

# 2010

## Annual Report Jahresbericht

**Remote Sensing  
Technology Institute**

Department  
Atmospheric Processors



**Published by** **German Aerospace Center (DLR)**  
A member of the Helmholtz Association

**Remote Sensing Technology Institute**  
Institut für Methodik der Fernerkundung (IMF)

Department  
**Atmospheric Processors (IMF-AP)**

**Department Head** Prof. Dr. Thomas Trautmann

**Editorial Team** Prof. Dr. Thomas Trautmann  
Dr. Manfred Gottwald  
Brigitte Rüba

**Layout** Dr. Manfred Gottwald

**Cover** Average tropospheric nitrogen dioxide (NO<sub>2</sub>) over East Asia between 2007-2009  
as seen by GOME-2 on MetOp.

## Contents

<b>1.</b>	<b>Foreword</b> .....	<b>3</b>
<b>2.</b>	<b>Atmospheric Remote Sensing – Instrument Operation, Calibration and Measurement Techniques</b> .....	<b>5</b>
2.1	The ATMOS Website .....	5
2.2	Application of QA4EO Principles to SCIAMACHY Level 1 Data .....	8
2.3	In-flight Spectral Calibration of the SCIAMACHY Channel 8 .....	11
2.4	SCIAMACHY Operations Support .....	13
2.5	SCIAMACHY Configuration in the Mission Extension Phase .....	16
<b>3.</b>	<b>Atmospheric Remote Sensing – Retrieval Methods</b> .....	<b>19</b>
3.1	Formaldehyd and Glyoxal in the Operational SCIAMACHY Processor .....	19
3.2	Operational and Scientific Limb Retrieval for SCIAMACHY .....	21
3.3	SCIAMACHY Level 2 Fast Delivery Service Timeliness .....	24
3.4	Migration of the SCIAMACHY Level 2 Processing Development Environment .....	27
3.5	GlobVapour – an IASI Assessment.....	33
3.6	Results from the Saharan Mineral Dust Experiment 2 (SAMUM-2).....	35
3.7	Radiative Transfer in a Diurnal Cycle of Inhomogeneous Shallow Cumulus .....	37
3.8	Reciprocity in Light Scattering Computations .....	41
3.9	Constrained Inversion Methods and Retrieval of O <sub>3</sub> Profiles from UV/VIS Nadir Instruments .....	43
3.10	Optimized Rational Approximations for the Voigt and Complex Error Function .....	45
3.11	Line-by-Line Tools for Absorption Optical Depths.....	47
3.12	Line-by-Line Computation of Atmospheric IR Spectra with Field Programmable Gate Arrays .....	49
3.13	First Results of Inversion for Infrared/Microwave Limb Sounding .....	51
3.14	Textbook on Numerical Regularization for Atmospheric Inverse Problems .....	54
<b>4.</b>	<b>Atmospheric Remote Sensing – Applications</b> .....	<b>56</b>
4.1	Remote Sensing of NO <sub>2</sub> Vehicle Emission using Mobile DOAS during Expo 2010 .....	56
4.2	Air Quality Measurements for the Expo 2010 in Shanghai from Space .....	58
4.3	The Eyjafjallayökull Eruption Monitored by GOME-2 .....	61
4.4	Operational O3M-SAF Trace Gas Column Products: GOME-2 NO <sub>2</sub> , BrO, SO <sub>2</sub> , CH <sub>2</sub> O and H <sub>2</sub> O .....	63
4.5	Venus Modeled Spectrum and Observations with SCIAMACHY .....	66
<b>5.</b>	<b>Documentation</b> .....	<b>69</b>
5.1	Books and Book Contributions.....	69
5.2	Journal Papers.....	69
5.3	Conference Proceeding Papers and Presentations .....	69
5.4	Attended Conferences and Professional Leaves.....	72
5.5	Diploma and Doctoral Theses.....	73
	<b>Abbreviations and Acronyms</b> .....	<b>74</b>



## 1. Foreword

This year's annual report is the 10<sup>th</sup> report which has been issued by us. Having achieved such a significant milestone is always a good opportunity both to look back and think about the future.

When the first annual report 2001 had been generated, IMF-AP was already established successfully in the then still rather new configuration of the Remote Sensing Technology Institute (IMF) and the German Remote Sensing Data Center (DFD) forming the *Cluster Applied Remote Sensing (CAF)*. Our activities 10 years ago focused on ESA's GOME sensor on ERS-2 and on the forthcoming launch of the ENVISAT mission. ENVISAT carried a suite of atmospheric remote sensing instruments – SCIAMACHY, MIPAS and GOMOS – into low-Earth orbit. Other future Earth Observation missions such as GOME-2 on EUMETSAT's MetOp series or suitable Earth Explorers, e.g. ADM-Aeolus, were still in their early stages. Together with theoretical work on radiative transfer, inverse modelling and scattering, a 'must' for succeeding in the retrieval of atmospheric parameters from remote sensing sensors, these activities qualified the first report to comprise 45 pages. Ten years later, the report volume nearly has doubled and now reflects our increased involvement in national and international EO missions. Nowadays Europe's fleet of atmospheric remote instruments is much larger than it was in 2001. This provides access to a huge data repository. Particularly the long timescales covered by GOME, SCIAMACHY and GOME-2 data permits new and exciting studies related to long-term climate change. In addition, the enormous progress in computer technologies was a pre-requisite for successfully tackling problems in retrieval studies which finally result in powerful new retrieval algorithms. We feel that what has been achieved in the past 10 years forms a sound basis for continuing to be an important member of the atmospheric remote sensing community.

What have been the highlights of 2010? Each individual team member might have his/her personal favourites, often related to a particularly demanding measurement campaign or exciting result. Undoubtedly important for all of us was certainly the inauguration of the new building at the DLR-Oberpfaffenhofen premises hosting staff from IMF and DFD. At that occasion the *Earth Observation Center (EOC)* was created replacing the former *Cluster Applied Remote Sensing*. The EOC reflects DLR's ambition to play a leading role in national and international Earth Observation. This will also help to provide our atmospheric remote sensing activities a continuous and prominent visibility.

We thank all our staff for their efforts and achievements in 2010 and their contributions to this annual report.

Prof. Thomas Trautmann  
Dr. Manfred Gottwald



## 2. Atmospheric Remote Sensing – Instrument Operation, Calibration and Measurement Techniques

### 2.1 The ATMOS Website

M. Gottwald, D. Loyola, G. Lichtenberg, B. Aberle

Maintaining an informative and up-to-date website is nowadays a 'must' for every scientific body aiming at gaining public attention. This is not only true for web pages providing information for public relation purposes but also for weblinks with scientifically or technically oriented content. It is just such pages which foster the exchange of scientific and technical information internally and externally.

In the past year DLR's Earth Observation Center (EOC) has launched the new EOC website (<http://www.dlr.de/caf>) providing information about the German Remote Sensing Data Center (DFD) and the Remote Technology Institute (IMF). It includes a more public relation type description about our section highlighting the major fields of IMF-AP, i.e.

- mathematics and physics (as required for remote sensing algorithms)
- sensor-specific methods
- processor development
- operations and support

In addition, IMF-AP has made its new ATMOS webserver fully accessible (<http://atmos.caf.dlr.de/>) in 2010. The information provided on this server supports scientific-technical tasks and applications.

Department  
Atmospheric Processors  
Earth Observation Center (EOC)

ATMOS - Atmospheric Parameters Measured by in-Orbit Spectroscopy

The department **Atmospheric Processors (AP)** of DLR's **Remote Sensing Technology Institute (IMF)** operates the **ATMOS** webserver. It provides internal and external services in the area of spaceborne atmospheric sensors. Currently these services include

- **SCIAMACHY Data Processing:**  
The SCIAMACHY Data Processing website provides access to level 0-1b and level 1b-2 relevant information such as tools and documentation. In addition it links to ESA's Earthnet environment where users may download SCIAMACHY and other remotely sensed products.
- **SCIAMACHY Operation Support:**  
The SOST website presents both an overview of SCIAMACHY operations concepts and actual mission planning issues. It serves the SCIAMACHY user community and ENVISAT/SCIAMACHY personnel as a tool to follow the operational status of the instrument. The SOST website is maintained by SOST-DLR with input from SOST-IUP/IFE.
- **GOME/ERS-2 Products:**  
This site lists information on the instrument including degradation effects as well as reference documents on retrieval algorithms and applications. In addition access to browse products from GOME/ERS-2 data is provided. The browse products include
  - Ozone (O3) total column
  - Nitrogen dioxide (NO2) total column
  - Cloud fraction (CF)
  - Cloud top pressure (CTP)
  - Cloud optical thickness (COT)both in NRT and offline mode.
- **GOME-2/MetOp Products:**  
This site lists reference documents on retrieval algorithms and applications. In addition access to browse products from GOME-2/MetOp data is provided. The browse products include
  - Ozone (O3) total column
  - Nitrogen dioxide (NO2) total column
  - Nitrogen dioxide (NO2) tropospheric column
  - Sulphur dioxide (SO2) total column
  - Bromine oxide (BrO) total column
  - Cloud fraction (CF)
  - Cloud top pressure (CTP)
  - Cloud optical thickness (COT)both in NRT and offline mode.

The listed items are the result of IMF-AP's involvement in national and international atmospheric remote sensing activities, including algorithm & processor development as well as instrument calibration & monitoring together with instrument operations. Details can be found on the web portal of the **Remote Sensing Cluster (CAF)**.

Home

**Services**

- SCIAMACHY Data Processing
- SCIAMACHY Operations Support
- GOME/ERS-2 Products
- GOME-2/MetOp Products

**AP Information**

- Annual Reports
  - 2009
  - 2008
  - 2007
  - 2006
  - 2005
  - 2004
  - 2003
  - 2002
  - 2001
- Overview
- Publications
  - 2009
  - 2008
  - 2007
  - 2006
  - 2005
  - 2004
  - 2003
  - 2002
  - 2001
- Conference contributions
  - 2010
  - 2009

**Imprint**

- ATMOS

Fig. 2-1: The ATMOS home page.

Currently the services listed on ATMOS cover:

- **SCIAMACHY Data Processing:** The SCIAMACHY Data Processing website permits access to level 0-1b and level 1b-2 relevant information such as tools and documentation. In addition it links to ESA's Earthnet environment where users may download SCIAMACHY and other remotely sensed products.
- **SCIAMACHY Operation Support:** The SOST website presents both an overview of SCIAMACHY operations concepts and actual mission planning issues. It serves the SCIAMACHY user community and ENVISAT/SCIAMACHY personnel as a tool to follow the operational status of the instrument. The SOST website is maintained by SOST-DLR with input from SOST-IUP/IFE.

- GOME/ERS-2 Products: This site lists information on the instrument including degradation effects as well as reference documents on retrieval algorithms and applications. In addition, access to browse products from GOME/ERS-2 data is provided. These browse products include
  - ozone (O<sub>3</sub>) total column
  - nitrogen dioxide (NO<sub>2</sub>) total column
  - cloud fraction (CF)
  - cloud top pressure (CTP)
  - cloud optical thickness (COT) both in near-realtime (NRT) and offline (OL) mode.
- GOME-2/MetOp Products: Reference documents on retrieval algorithms and applications are provided, together with access to browse products from GOME-2/MetOp data. The browse products include
  - ozone (O<sub>3</sub>) total column
  - nitrogen dioxide (NO<sub>2</sub>) total column
  - nitrogen dioxide (NO<sub>2</sub>) tropospheric column
  - sulphur dioxide (SO<sub>2</sub>) total column
  - bromine oxide (BrO) total column
  - water vapour total column (H<sub>2</sub>O)
  - formaldehyde total column (HCHO)
  - cloud fraction (CF)
  - cloud top pressure (CTP)
  - cloud optical thickness (COT) both in NRT and offline mode.

In addition, IMF-AP uses the ATMOS server for distributing reference material on an annual basis such as

- annual reports
- publication lists
- conference contributions

The listed items are the result of IMF-AP's involvement in national and international atmospheric remote sensing activities, including algorithm & processor development as well as instrument calibration & monitoring together with instrument operations.

#### GOME and GOME-2 Services

Particularly the GOME related product services have already reached a mature level. Images of near-realtime, offline and historical GOME-1 and GOME-2 operational products are updated automatically on the ATMOS server. Navigation facilities exist which are either focused on each sensor separately or on products from both satellites. The GOME-2 page hosts additional information for O<sub>3</sub> and SO<sub>2</sub> by providing operational services based on these data such as e.g. ozone assimilation and forecasting, and volcanic eruptions. The navigation on products contains entries for the trace gases mentioned above (Fig. 2-2). In addition the new product *Ozone Essential Climate Variable (ECV)* created by merging total ozone from GOME, SCIAMACHY and GOME-2 can be retrieved.

Links to documents describing the products (e.g. Algorithm Theoretical Basis Documents – ATBD, Product User Manuals – PUM) are given. This is supplemented by related scientific peer-reviewed papers, which can be directly downloaded, and external links relevant for the corresponding instrument.

Browsing of historical data is facilitated by means of an interactive calendar. The user can select the desired sensor, product, month and date. Clicking on a given day will open a new window providing a detailed view of the selected product (Fig. 2-3).

The layout of the images was updated in December 2010 following the new Earth Observation Center (EOC) guidelines for quick-look images (Fig. 2-4). This occurred in close collaboration with and under the guidelines of DFD-WV. Images and re-gridded data compliant with the new layout are being created with the UMAS system (Unified Mapping Tool for Atmospheric Spectrometers) developed at IMF-AP. At DFD-IT work is in progress to integrate UMAS in the DIMS system for the generation of the operational quick-looks generated at the EOC in the framework of the Ozone Monitoring SAF (O3M-SAF).

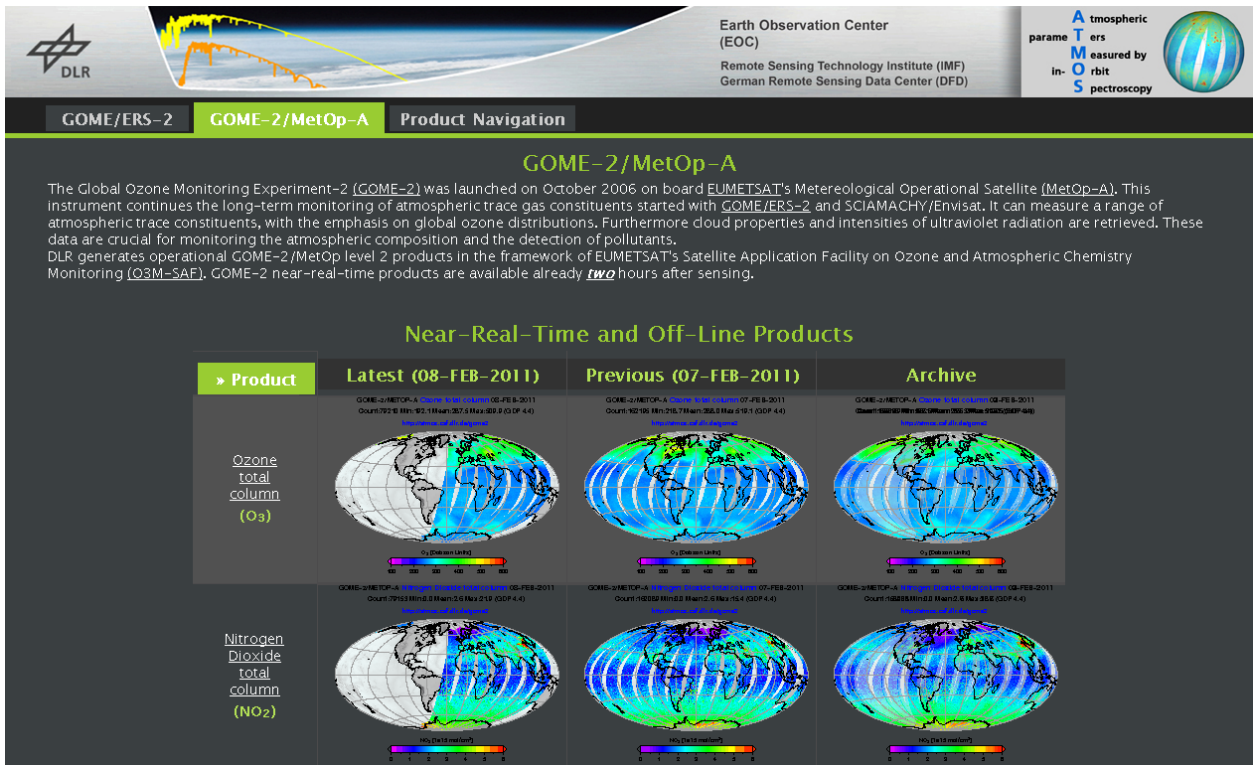


Fig. 2-2: The GOME-2 home page on the ATMOS server.



Fig. 2-3: Ozone product navigation page for November 2010.

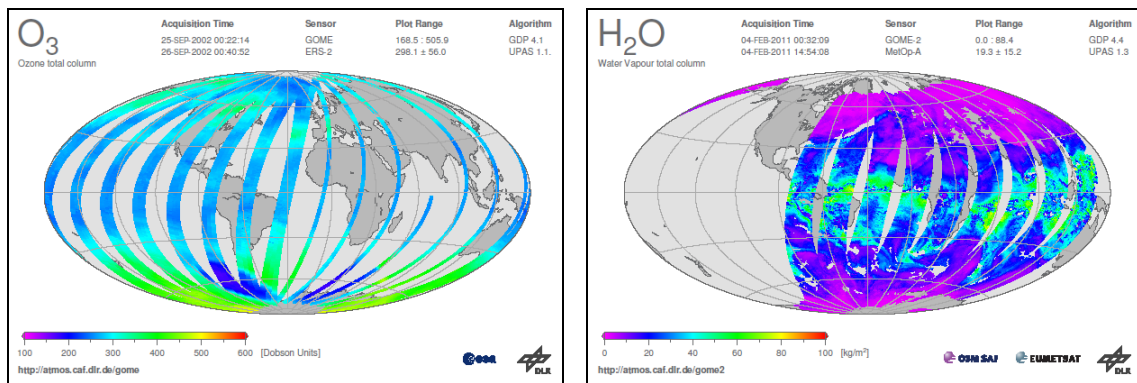


Fig. 2-4: New layout of the GOME and GOME-2 images.

## 2.2 Application of QA4EO Principles to SCIAMACHY Level 1 Data

*G. Lichtenberg*

Quality Assurance Framework for Earth Observation (QA4EO) seeks to improve interoperability of Earth observations made by different instruments. This is achieved through the establishment of the key principle that all data products should have associated with them a quality indicator based on documented evidence of traceability to internationally agreed standards. QA4EO provides guidance on how to follow and demonstrate best this principle in a harmonized manner through a set of key guidelines. Therefore traceability for data products, starting with the on-ground calibration and ending with derived products used in e.g. model and assimilation applications, is urgently required. The basis of all derived products is usually level 1 data, which combine on-ground calibration with in-flight monitoring and calibration measurements. Quality assurance and specifically QA4EO requires the documentation of calibration uncertainties as well as constant monitoring of the data quality during the mission lifetime.

In the case of SCIAMACHY, the level 1b data product comprises raw and geolocated data accompanied by all calibration parameters needed to generate the so-called 'level 1c' product with radiances as a function of wavelength. The mission concept includes frequent in-flight calibration and monitoring measurements. The instrument measures moderately resolved spectra (about 0.2 nm, depending on spectral region) in the wavelength range between 212-2384 nm and performs broadband measurements with the channels of the Polarisation Measurement Device (PMD). Viewing geometries comprise nadir, limb and occultation. The size of the ground pixel for nadir measurements varies, due to the diverse integration times, between 32 km × 233 km (along track × across track) and 26 km × 30 km.

### Calibration Concept for SCIAMACHY

Ideally, calibration measurements should be done under the same conditions as in space, i.e. in a tank with thermal vacuum conditions. SCIAMACHY has scanning mirrors, i.e. various incidence angles on the mirrors have to be characterised in the on-ground calibration. However, the size of the vacuum tank did not allow the necessary rotation of the instrument to all necessary angles. Therefore, SCIAMACHY was calibrated using a combination of thermal vacuum measurements (TV) representing the conditions in space and measurements done under ambient conditions. For the ambient measurements, only the mirror (combination) and the mirror/diffuser combination was measured by putting the modules with mirrors and diffusers on an optical bench, mimicking the distances and angles within the instrument. Ambient measurements were performed at several angle combinations and wavelengths. For the TV measurements the completely integrated instrument was used with the full wavelength range and resolution, but only one incidence angle combination for the different observation modes (nadir, limb, monitoring and calibration) was measured. In order to transfer the ambient calibration to the TV calibration, ambient measurements were done for the same angles as the TV measurements. Since SCIAMACHY is a polarisation sensitive instrument, measurements were performed using light sources of various polarisation directions.

In order to maintain the calibration over the whole mission, calibration measurements are also scheduled in-flight:

- weekly white light source (WLS) measurements with an on-board Tungsten-halogen lamp
- weekly spectral calibration measurements employing the on-board spectral line source (SLS, a PtCrNe lamp)
- dark measurements in eclipse and looking at large tangent heights above the atmosphere every orbit
- daily sun-over-diffuser measurements to correct the Earth spectrum for the solar spectrum and obtain the reflectance
- monitoring measurements to determine the degradation of the instrument using
  - Sun above atmosphere observations with mirrors in different observation modes
  - Moon above atmosphere observations
  - WLS and SLS observations using mirrors and diffusers.

From the combination of all those measurements and the calibration measurements on-ground, in principle, a complete characterisation of the instrument can be done. The calibration equation for any given pixel of the SCIAMACHY detectors can be formulated as

$$S_{i,det} = m_{deg} \cdot c_{pol} \cdot I(\lambda) \cdot \Gamma_{inst}(\lambda) \cdot QE(T_{det}, \lambda) + S_{stray} + S_{elec} + DC$$

with

$S_{i,det}$	= signal measured by the detector in pixel $i$
$m_{deg}$	= degradation correction
$c_{pol}$	= polarisation correction
$I(\lambda)$	= wavelength dependent incoming intensity
$\Gamma_{inst}(\lambda)$	= transmission of the instrument
$QE(T_{det}, \lambda)$	= detector temperature dependent quantum efficiency of the detector pixel,
$S_{stray}$	= stray light correction,
$S_{elec}$	= electronic corrections like non-linearity or memory effect
$DC$	= dark signal of the detector pixel

The inversion of this equation together with the application of the wavelength calibration and slit function correction results in calibrated radiances. Dividing the Earth radiance by the sun irradiance yields the reflectance which can be regarded as the basis of the trace gas retrieval. For the retrieval of atmospheric parameters, two main methods are applied: the DOAS (Differential Optical Absorption Spectroscopy) type retrievals use the differential structures of the spectrum and are insensitive to the absolute values of the spectrum but require a very high ( $10^{-4}$  or better) relative pixel-to-pixel accuracy. Direct retrieval methods using absolute reflectances are sensitive to the absolute values, but are somewhat less dependent on the relative accuracy values.

#### Quality Indicators and Traceability

QA4EO principles request application specific quality indicators and full traceability of the product as well as quality assurance for the duration of measurements. SCIAMACHY level 1 data already contain several quality indicators, i.e. total errors on

- radiance for spectra
- irradiance for solar spectra
- reflectance

Since DOAS type retrievals depend mainly on spectral structures, a definition of an additional quality indicator describing the accuracy from pixel-to-pixel or within a spectral retrieval window is currently discussed. Traceability covers two aspects. Firstly the data must be tied to internationally agreed standards and secondly, the user must be informed of transient degradation for the product quality. For SCIAMACHY, traceability is ensured by

- reporting problems and limits of data products in publicly accessible product disclaimers
- tying the absolute radiometric calibration to a NIST calibrated FEL lamp
- giving errors for calibration data

Still, traceability can be improved, especially in the area of calibration errors. In some cases like stray light and electronic effects, the errors given are upper estimates. It is planned to improve the error determination using available on-ground and in-flight data. A principle problem is the knowledge of the polarisation correction error (see below), which can only be estimated.

### Calibration Uncertainties and Quality Assurance

Even with extensive calibration campaigns the calibration of satellite instruments will always be hampered to a certain extent by uncertainties due to e.g. the instrument design or physical limits. For SCIAMACHY DOAS type retrievals there are two main issues:

- *Polarisation correction:* SCIAMACHY is a polarisation sensitive instrument. The correction for the polarisation uses in a complex way on-ground and in-flight measurements and theoretical assumptions. Especially, the polarisation correction depends on the in-flight measurements of the polarisation state of the atmosphere. The accuracy of these measurements can only be roughly estimated, because there are no independent determinations for the atmospheric polarisation that can be used for SCIAMACHY. In certain wavelength regions, an error in the polarisation determination will show up as a spectral artefact. This effect can be mitigated by choosing – where possible – spectral retrieval windows with weak polarisation sensitivity.
- *Spectral Structures:* These are mainly caused by the so-called ‘white light interference’ of the sun diffusers. They change with season and possibly with time and are difficult to determine. Particularly the retrievals of weak absorbers like BrO or CHOCHO are sensitive to spectral artefacts.

Once the satellite is in orbit, the calibration should be checked independently to ascertain that the previously determined precision and accuracy is achieved. This can be done in two ways: comparison with radiative transfer models and measurements from other satellites (1) or comparison with on-ground measurements (2). However, both approaches have their drawbacks. For full traceability, models themselves must be tied to calibrated observations. Other satellites usually do not measure at the same time and location. In addition it can be difficult to find stable ground scenes for a comparison which at the same time are representative for ‘normal’ measurements. For SCIAMACHY the comparison with on-ground measurements, which usually cover only a very small area, can only give a rough indication of uncertainties, because of its large ground pixels. This wide extent also makes it difficult to find cloud free scenes. For example for the DOME-C campaign only 87 spectra out of a total of 400 were classified as cloud free! Additionally, most on-ground measurements are done for imagers with a much lower spectral resolution often even not covering the wavelength range from 212-2384 nm as needed for SCIAMACHY.

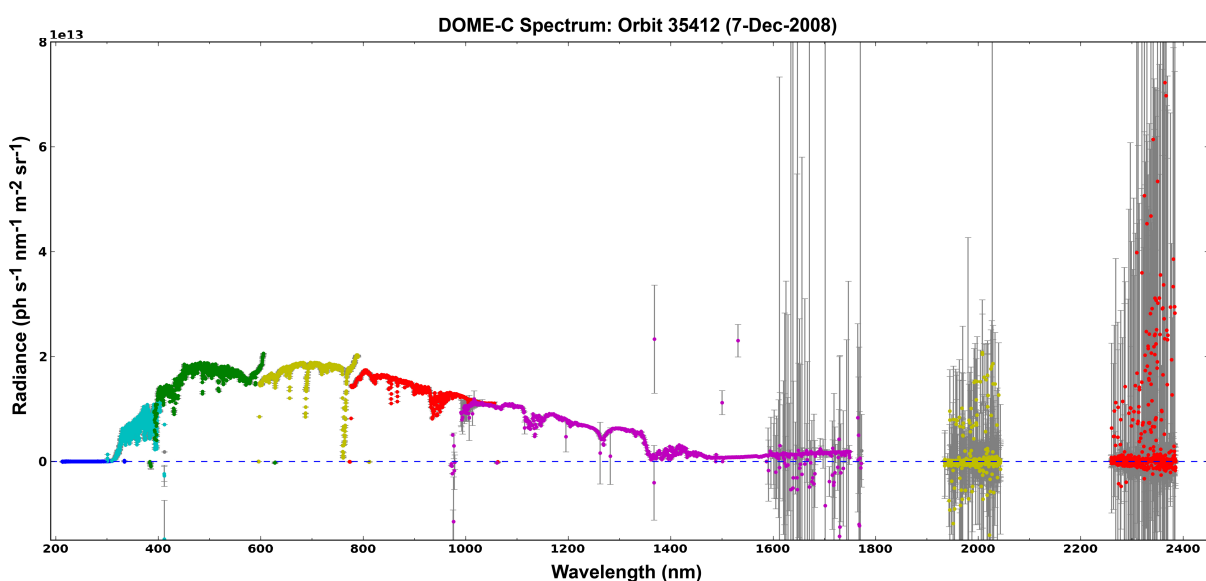


Fig. 2-5: Example for a SCIAMACHY spectrum of a ground pixel containing the DOME-C calibration site. Different colours indicate the different channels. The high error of in the short wave infrared channels ( $\lambda > 1600$  nm) is mainly caused by bad or dead pixels. These pixels have degraded in quality due to proton impact in the space environment.

Nevertheless, several efforts are made to improve the calibration information. Recently, SRON (Netherlands Institute for Space Research) re-analysed all on-ground measurements and combined polarisation and radiance measurements to come to a fully self-consistent characterization of the instrument. This characterization will become part of the next level 0-1b processor. Furthermore the analysis of all in-flight monitoring measurements obtained in the last 8 years provides insight to instrument degradation. Finally SCIAMACHY measurements were part of the DOME-C campaign, an initiative aiming at improving data quality by comparing various space-borne missions with measurements from a well characterized ground station, the DOME-C on the Antarctic Ice Sheet. The analysis of these measurements has started and will continue in the coming year (Fig. 2-5).

### 2.3 In-flight Spectral Calibration of the SCIAMACHY Channel 8

*S. Gimeno García (TUM), S. Slijkhuis, F. Schreier, G. Lichtenberg, M. Meringer, B. Aberle, K. Kretschel*

In order to ensure high spectral stability over the lifetime of the mission, SCIAMACHY has been equipped with a calibration lamp, the Spectral Line Source (SLS) for determining the pixel-to-wavelength relation. Whereas the SLS has been proved to be suitable for a precise in-flight spectral calibration of channels 1-6, it is insufficient for the calibration of channels 7 and 8 due to the lack of enough SLS spectral lines within these channels. Because of this, the pixel-to-wavelength relationship of channels 7 and 8 in the level 1b product is set to the on-ground calibration. Although on-ground calibration was performed under representative temperature and vacuum flight conditions, a similar spectral tuning as in the other channels should be applied to channels 7 and 8 for a precise spectral calibration.

Molecular spectral properties have been precisely determined in laboratory experiments and are publicly available in spectroscopic datasets, such as e.g. HITRAN and GEISA. This information can be exploited for an in-flight spectral calibration. Actually, radiative transfer models simulating Earth radiance spectra as measured by SCIAMACHY can provide non-shifted reference spectra.

In 2010 we improved the in-flight spectral calibration of SCIAMACHY's channel 8 based on absorption signatures of atmospheric methane, water vapor and carbon monoxide. The procedure followed was to apply different wavenumber shifts to the observed spectra and fit the shifted (observed) spectra to modelled ones. The spectra were selected from measurement states executed on March 27<sup>th</sup> for all years of the mission (2002-2010) over the Sahara without cloud contamination. The selection of this particular day was arbitrary but we kept this date in order to avoid seasonality effects. Fig. 2-6 shows the state location and the measured spectra corresponding to March 27<sup>th</sup>, 2003 (similar plots are obtained for the rest of the years).

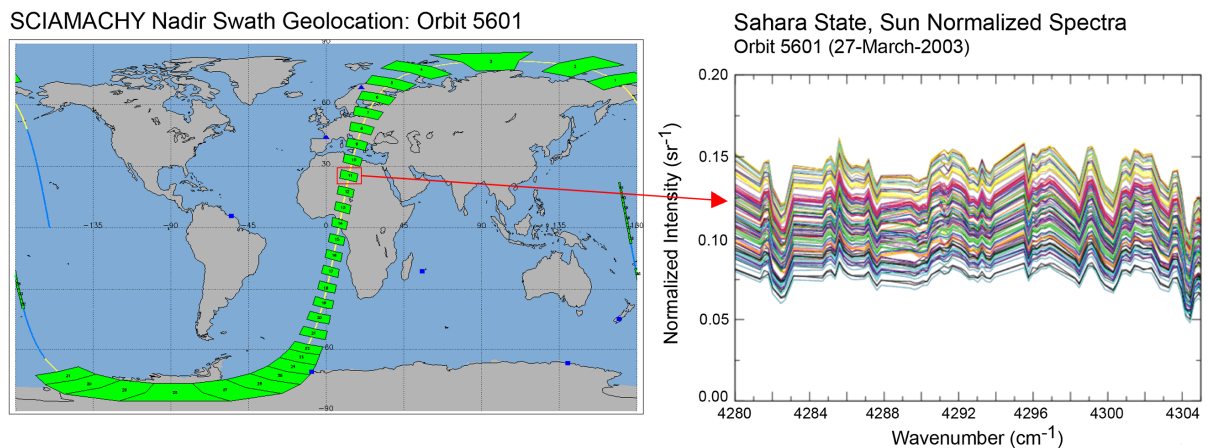


Fig. 2-6: The left panel shows the nadir states of orbit 5601 (March 27<sup>th</sup>, 2003). The right panel shows SCIAMACHY channel 8 measured spectra corresponding to the Sahara state within the red square in the left panel. Backscan observations were not taken into account.

We systematically applied wavenumber shifts ranging from  $-0.40 \text{ cm}^{-1}$  to  $0.85 \text{ cm}^{-1}$  in steps of  $0.05 \text{ cm}^{-1}$  to the measured spectra. Additionally, we divided channel 8 into 20 spectral sub-regions. For each sub-region and each wavenumber shift we calculated the cross-correlation coefficients between the shifted (observed) and the modelled spectra. The actual wavenumber shift (with respect to the on-ground calibration) associated to each spectral sub-interval was assumed to be the one with maximum cross-correlation coefficient. In order to find the maximum, we fitted a spline curve.

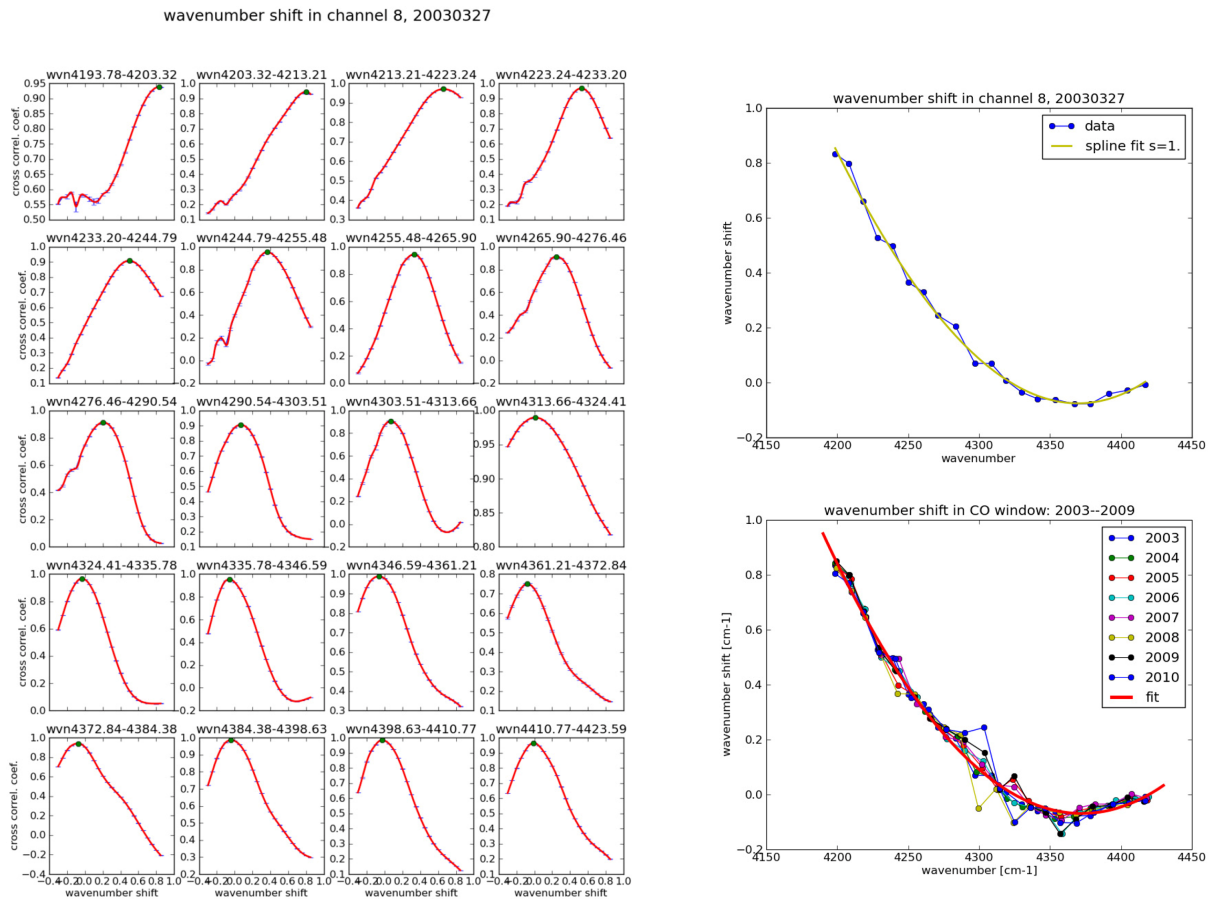


Fig. 2-7: Cross-correlation coefficient between shifted (measured as in Fig. 2-6) and modelled spectra as a function of the applied wavenumber shifts for 20 sub-regions of channel 8 (left). Spectral correction corresponding to each of the 20 sub-regions in channel 8 for the March 2003 measurement (right top) and correction for other years (right bottom).

The left panel of Fig. 2-7 displays the cross-correlation coefficients as a function of the applied shift for the 20 spectral sub-intervals. The plots correspond to March 27<sup>th</sup>, 2003, but similar plots are found for the rest of the years. The top right panel illustrates the spectral shift (maxima position of the individual curves on the left panel) as a function of the wavenumber. It represents the correction to be applied to the measured spectra. The bottom right panel displays the spectral shift as a function of the wavenumber for all years. Note that apart from some outliers, all curves have a similar spectral dependency, suggesting that a constant correction over the life time of the mission is sufficient. The spectral correction was fitted to a 2<sup>nd</sup> degree polynomial (shown in red). Its value can be as large as  $0.8 \text{ cm}^{-1}$ , i.e. more than 4 pixels, at the left edge of channel 8 (right edge in wavelength). Correcting this deviation from the on-ground pixel-to-wavelength relation (included in the level-1b product) is mandatory for a proper retrieval of trace gas vertical columns from channel 8. In the case of carbon monoxide (CO), neglecting it would have a dramatic impact on the quality and the absolute values of the retrievals.

Finally Fig. 2-8 compares an observed with a modelled spectrum without (left) and with (right) spectral correction. Note that, apart from some outlier, the spectral correction reduces the absolute value of the residuum (green lines) as well as its spectral structure.

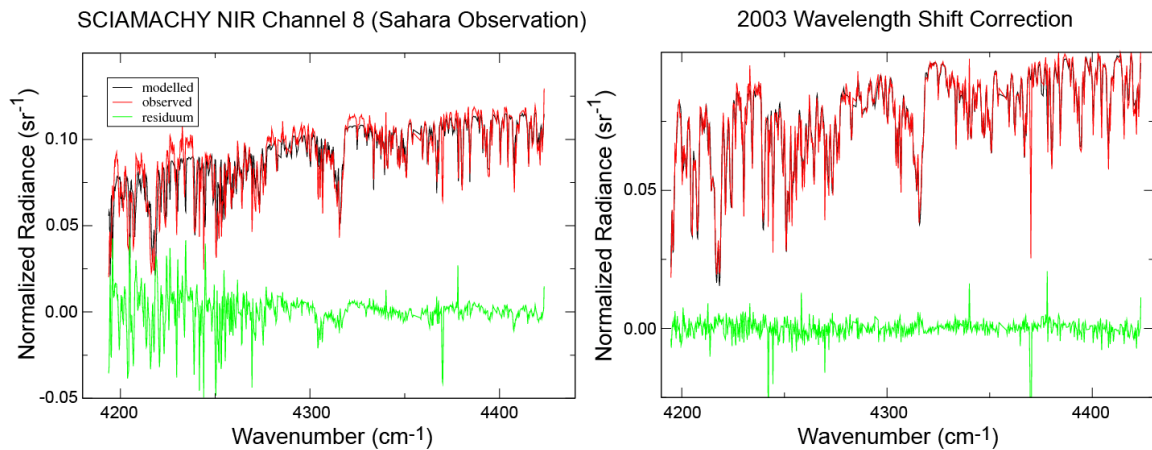


Fig. 2-8: Observed and modelled spectrum without (left) and with (right) spectral correction.

## 2.4 SCIAMACHY Operations Support

*M. Gottwald, E. Krieg (TwIG), K. Reissig (IBR), J. How (TwIG), S. Noël (IUP-IFE), K. Bramstedt (IUP-IFE)*

'The same procedure as every year' – this phrase describes best the work of the SCIAMACHY Operations Support Team (SOST), formed by personnel from IMF-AP and IUP-IFE/University of Bremen.. In 2010 our collaborations with the Quality Working Group (SQWG) and ESA (flight operations at ESOC, post launch support at ESTEC and payload data segment at ESRIN) were successfully continued.

When compared to 2009, the instrument availability remained high (Fig. 2-9). Anomalies caused the loss of 159 orbits. 4 of them were triggered by a ground segment deficiency while the rest was instrument related. One of the persistent errors of the early mission phase, the CCA MCMD check error, returned with in total 5 events (94 orbits) while the rest can be attributed to Single Event Upsets (SEU), i.e. high energy particles impinging onto instrument electronic components. Platform orbit control manoeuvres (OCM) required a transfer to MEASUREMENT IDLE in 14 orbits and the manoeuvres to lower the orbit altitude (see chapter 2.5) added another 73 orbits in this mode. Although it seems that the anomaly rate increased slightly, the overall availability reached the high value of 97% taking only anomalies into account or 95% when also considering orbit manoeuvres.

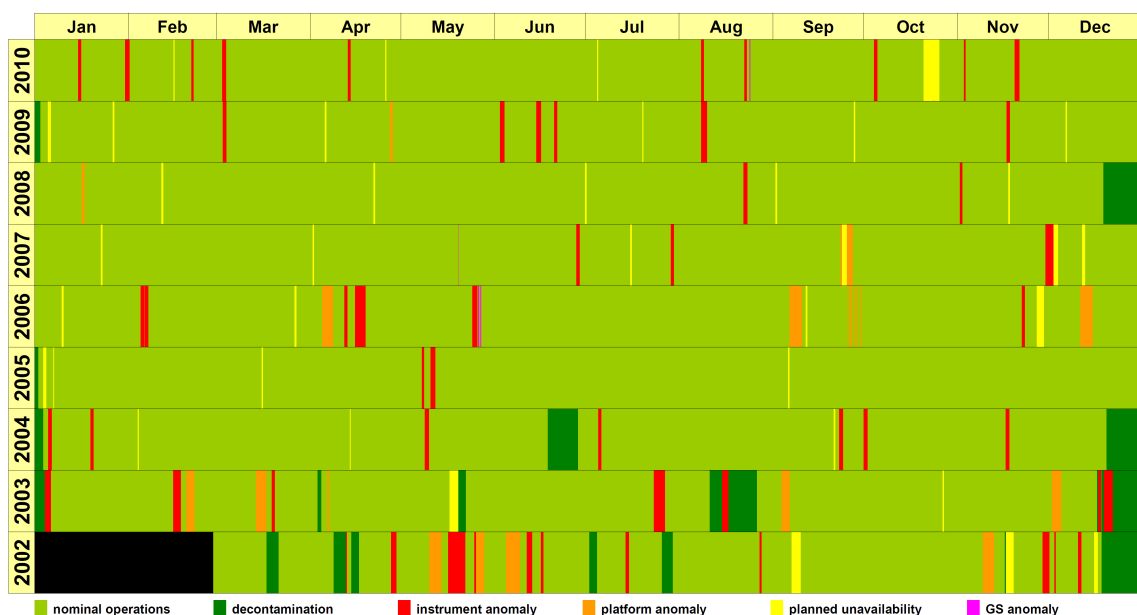


Fig. 2-9: Instrument availability since launch

On a monthly basis the availability was between 90-95% (Fig. 2-10) except for October because of the long MEASUREMENT IDLE mode due to the orbit manoeuvre.

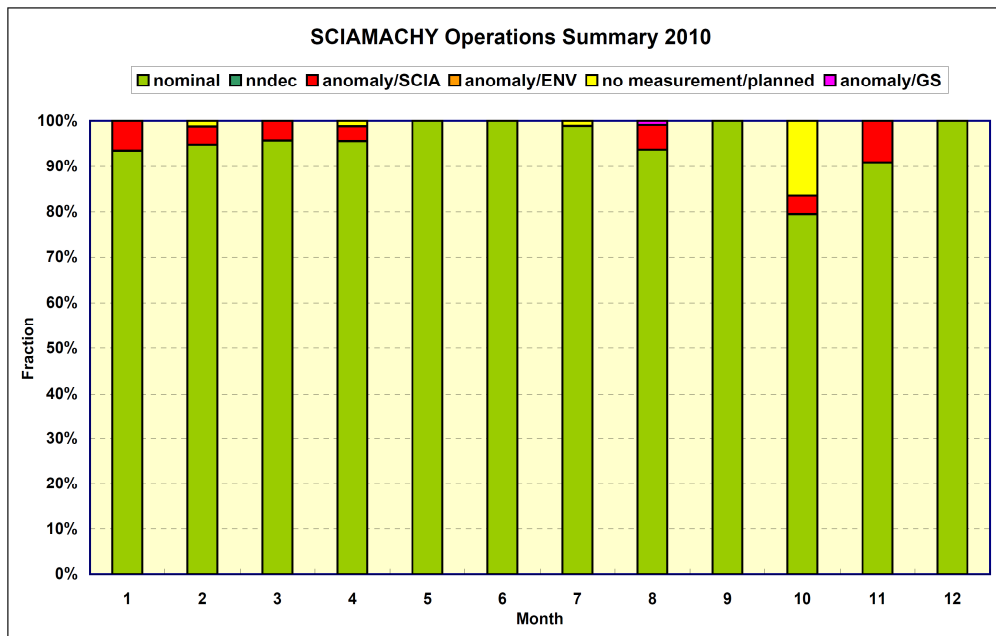


Abb. 2-10: Instrument availability in 2010 on a monthly basis

### Operation Change Requests

An impressive number of 8 *Operation Change Requests (OCR)* was successfully implemented. Two refer to the reconfiguration of the instrument for the mission extension phase (see chapter 2.5) and triggered new final flight state and timeline settings. The others implemented either scientific or calibration objectives. OCR\_046 (phytoplankton studies in the Arctic Atlantic Ocean) achieved a record time period of only 5 days between OCR submission and implementation!

### Routine Operations

The routine operation tasks were executed as required and planned. This applies to measurement planning, on-board configuration and long-term monitoring. All results were made available via the SOST webpages (<http://atmos.af.op.dlr.de/projects/scops/>). Since the mission lifetime has already been extended appreciably, presentation of the monitoring results was adapted accordingly. Now all temperatures and power readings, which are subject to regular monitoring, are displayed for the entire mission phase. The same is true for the scanner motor currents as a means for scanner monitoring. Degradation effects can now be easily detected and separated from other effects.

### Scanner Monitoring

As in 2008 and 2009 a four orbit sequence of *Non-Nominal Telemetry (NNTM)* formats during state 65 execution was commanded and acquired in June (see 2009 annual report). Thus studies of specified scanner current telemetry HK parameters during regular execution of state 65 continued. Analysis of the 2010 NNTM telemetry indicates almost identical current behaviour and no sign of degradation. While slightly higher readings for the ESM\_cw, ESM\_mean and ASM\_mean data in 2009 compared to 2008 during the high-acceleration part at the end of the measurement phase was obvious, the opposite occurred in 2010 when the ESM readings indicate signs of improvement. Contrary to this the ASM currents increased by about 5 mA.

Another method for scanner monitoring is the regular check of the ASM/ESM scanner currents obtained during execution of representative states. These are states 02 (nadir), 33 (limb), 49 (solar occultation) and 65 (scanner maintenance). Despite the coarse time resolution of 1/16 Hz, the state design causes for each state type a distinct current pattern. Changing current patterns could indicate the beginning of a scanner degradation. Up to now for all selected states the patterns remain rather stable. Even the observed increase in ESM scanner currents during state 65 execution has levelled out and the telemetry

readings returned to a level already observed before (Fig. 2-11). Close scanner monitoring continues throughout the mission lifetime.

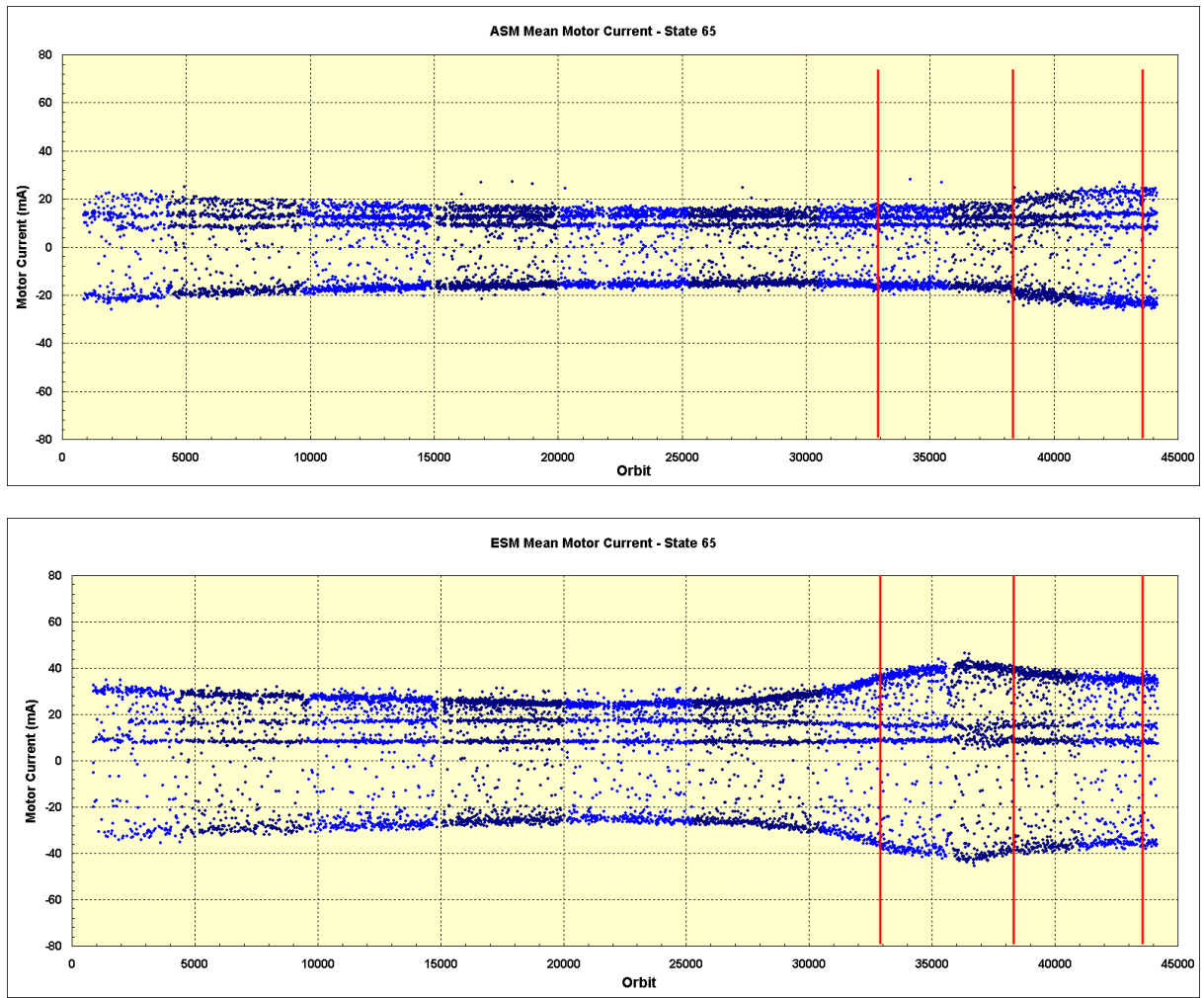


Fig. 2-11: ASM (top) and ESM (bottom) mean motor currents during state 65 execution from the standard ASM/ESM current monitoring since beginning of the mission. The red vertical bars indicate times of NNTM execution.

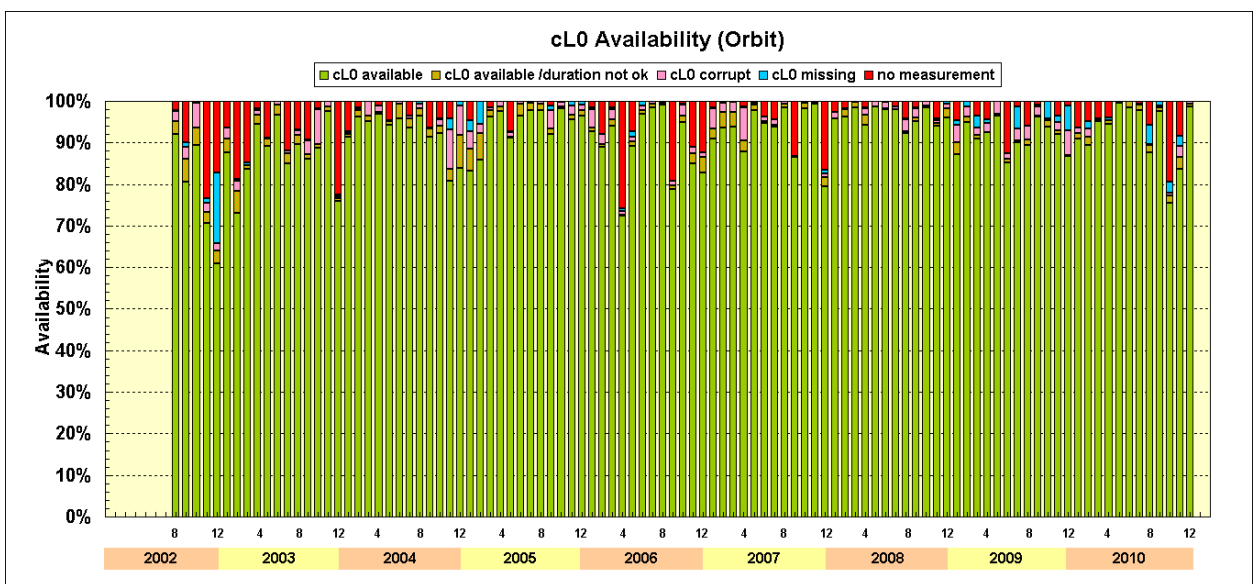


Fig. 2-12: cL0 statistics for the years 2002-2008 (final) and 2009-2010 (preliminary).

### Consolidated Level 0 Master Archive

In 2010 SOST continued to maintain its master archive of consolidated level 0 (cL0) data in the Data Information Management System (DIMS) environment of the German Remote Sensing Data Center (DFD) at DLR. It serves as a cL0 reference and supports SCIAMACHY product debugging in ENVISAT's Payload Data Segment (PDS). Consolidated level 0 data are regularly transferred to DIMS once they passed a sequence of checking routines. These verify the overall integrity of the cL0 products.

By the end of 2010 more than 45000 cL0 products have been quality checked and transferred to DIMS. The statistics for the years 2002-2010 is displayed in Fig. 2-12. Note that for 2009 and 2010 the results are only preliminary since the second re-consolidation at ESA has not yet been performed. The detailed cL0 availability on single orbit level is given at the SOST website (<http://atmos.caf.dlr.de/projects/scops/>).

## 2.5 SCIAMACHY Configuration in the Mission Extension Phase

*M. Gottwald, E. Krieg (TwIG), F. Cirillo (EADS Astrium), P. Lützow-Wentzky (EADS Astrium)*

In 2010 the preparation of SCIAMACHY for the ENVISAT mission extension until the end of 2013 had to be finalized including the implementation and – after the orbit change – the verification of the modified instrument status. Until early autumn final studies were executed, followed by a very short period for generating the inputs required by the ENVISAT flight operation segment. The actual orbit manoeuvre occurred in late October while the measurements in November were particularly aiming at verifying the modified final flight configuration.

### Orbit Definition and Analysis

The modified orbit for the mission extension phase was slightly updated by ESA in mid 2010. It required to adapt the orbit analysis since the corresponding change of some orbit parameters was larger than the accuracy of some entries in scanner control tables. Main differences between the nominal and the operational modified orbit are listed in table 2-1.

	Nominal Orbit	Modified Orbit (Oct 2010)	Modified Orbit (Dec 2013)
Semimajor axis (km)	7159.496	7142.146	7141.919
Orbital period (sec)	6035.928	6014.037	6013.772
Inclination (°)	98.549	98.537	98.398
Orbits per day	14.314	14.366	14.367

Table 2-1: Orbital parameters of nominal and mission extension ENVISAT orbit

SCIAMACHY as an instrument with multi-viewing capabilities is strongly dependent on the status of the line-of-sight (LoS) during measurements. Additionally, instrument operation is driven by sun- and moon-fixed events along the orbit. Their occurrence depends on the selected orbit. Therefore a modification of the ENVISAT orbit has major impacts on SCIAMACHY operations. The corresponding modification of the instrument status was a split activity between EADS Astrium (Friedrichshafen) and SOST reflecting the responsibilities for measurement planning and execution (SOST) and on-board software and engineering configuration (EADS Astrium).

### Engineering Parameter Updates

EADS Astrium investigated the orbit dependent engineering parameters in the *Scanner Constants* table comprising the

- semimajor axis  $a_0$
- inclination  $i_0$
- number of orbits per day  $N_{ref}$

- mean tangent length  $l_{t,obs}$  (from spacecraft to Earth's horizon)
- mean elevation angle  $\varphi_{t,obs}$  (of Earth's horizon)

The first three parameters refer to the mean Kepler elements of the ENVISAT orbit, i.e. the reference orbit with a 35 day / 501 orbits repeat cycle in the nominal phase and the slowly drifting orbit in the mission extension phase from October 2010 onwards with a 30 day / 431 orbits repeat cycle. The final two elements (Table 2-2) are used in the framework of the Earth model correction for computing the polar and equatorial radius of the observation reference ellipsoid, which describes the observation altitude above the reference Earth model. Both parameters assume a spherical Earth and a mean spacecraft altitude being the average of the orbital minimum and maximum values.

	Nominal Orbit	Modified Orbit (Oct 2010)	Modified Orbit (Dec 2013)
tangent length $l_{t,obs}$ (km)	3290.000	3252.977	3252.592
elevation angle $\varphi_{t,obs}$ (rad)	4.239098	4.241217	4.241217
elevation angle $\varphi_{t,obs}$ (°)	242.882	243.004	243.004

Table 2-2: Scanner Constants parameters for Earth model correction in nominal and mission extension ENVISAT orbit

Since the scanner control parameters are specified with rather tight orbital tolerances, the large parameter drifts over the mission extension period requires updates at regular intervals.

#### Limb/Nadir Matching

The matching of the geolocation of limb states with associated nadir states is a major scientific requirement for SCIAMACHY operations. It has an across-track and an along-track aspect, both being orbit dependent. Scanner control treats the across-track component in the framework of the *Earth model correction with instrument yaw steering*. The ENVISAT platform is operated in stellar yaw steering mode, i.e. compensating for the Earth velocity vector at the subsatellite point. Thus, when observing a volume of air in limb mode, the rotational velocity of this part of the atmosphere does no longer ensure that it has rotated exactly onto the subsatellite track when SCIAMACHY passes over it. Therefore a correcting instrument yaw steering angle is applied shifting the limb LoS such that the limb and the corresponding nadir state, executed later, sense the same volume of air. Since the current platform yaw steering model is maintained for the mission extension orbit, the need for changing this angle could only result from the lowered orbit altitude. EADS Astrium showed that within specification the look-up table for the instrument yaw steering correction table for the nominal orbit is also applicable in the mission extension orbit.

To ensure accurate along-track limb/nadir matching it is necessary to place the geolocation of the limb tangent point into the middle of the nadir ground pixel. When the spacecraft altitude is lower, the length of the limb tangent LoS is reduced by 35 km and intercepts the atmospheric layers 'earlier' along-track. Maintaining the performance of the current limb/nadir matching can be achieved by skipping one horizontal scan in the limb states thus shortening the limb measurements by 1.6875 sec. Then the matching nadir state is executed 6.75 sec earlier in the modified orbit, corresponding to an along-track shift of about 40-45 km. Reducing a limb state by a single horizontal scan would result in a maximum achievable altitude of 90 km which is considered too low for upper atmosphere studies. Therefore it was decided to increase the limb starting altitude from -3 km (one step below the horizon) to 0 km (horizon).

#### Measurement Parameter Updates

SOST had to update those measurement parameter tables reflecting the orbit driven LoS changes. The modifications of azimuth/elevation angles due to the change in orbit altitude affected only the *Basic Profile Scan* table. Of the 15 basic profiles 5 required adapted elevation angles. Shortening the limb states and rising the start scan altitude caused modified entries in the *Scanner State* tables and *State*

*Duration* table. In addition a new timeline set was needed since a large fraction of the currently specified 109 timelines execute limb states. All of them are becoming shorter.

Because the nadir scan angle remained unchanged, lowering the altitude reduces the width of the nadir swath. This could not be compensated for due to the fact that on each side the scan is limited by baffles. At the reduced mean altitude the nadir swath width amounts to 933 km as compared to 954 km in the nominal orbit. In order to match the limb swath width as precisely as possible, the limb scan angle had to be adjusted accordingly. This occurred by adapting the *Relative Scan Profile* table no. 3 by a small amount.

#### Manoeuvre Schedule

At the end of orbit 45188 (October 21<sup>st</sup>) SCIAMACHY stopped measuring, followed by a 5-day period in MEASUREMENT IDLE mode. During this phase the updated engineering parameters were uploaded procedure driven. At the same time, on October 22<sup>nd</sup> and 26<sup>th</sup> four orbit lowering manoeuvres occurred by firing dedicated thrusters on the ENVISAT platform. Another minor thruster firing for orbit adjustment was scheduled for November 4<sup>th</sup>. However this did not impact the status of SCIAMACHY. Shortly after the manoeuvre on October 26<sup>th</sup>, in orbit 45261, SCIAMACHY continued measurements in the modified orbit. At the start of this period the updated measurement CTI tables and the new timelines were uploaded via MPS.

#### Verification

Analyzing the measurement data and HK telemetry received since then revealed that in general the instrument was successfully adapted to the modified orbit. However two effects became obvious which required further investigations. One concerned the thermal status. All detector temperatures were higher by up to 0.5 K and the ATC heater powers were reduced by up to 0.8 W. The HK readings of other SCIAMACHY subsystems also indicated increased temperatures. This was even the case for ENVISAT platform subsystems and other instruments. It is suggested that a switch to KBS-3 (Ka-band antenna subsystem) from KBS-2, which showed an anomaly on October 21<sup>st</sup> unrelated to the orbit manoeuvre, is the cause of the modified thermal environment. While KBS-2 was not permanently 'on', KBS-3 is running continuously thus dissipating now additional energy equivalent to 120 W.

The second effect relates to the tangent heights in limb measurements. With the Basic Scan Profile table settings updated for fixed altitudes of 0 km (limb start scan), 17.2 km (Sun occultation), 150 km (limb\_mesosphere start, limb\_mesosphere\_thermosphere start), 250 km (limb dark current pointing) and 350 km (limb\_mesosphere\_thermosphere dark current pointing) the specified tangent heights of 0 km, 150 km, 250 km and 350 km could not be fully achieved. Reason is most likely the underlying spherical Earth model in the corresponding correction algorithm. Therefore a test in December with slightly modified Basic Scan elevation angles was executed. It yielded the required limb altitudes. The corresponding measurement parameters are scheduled for a permanent update of the Basic Scan profile table in early 2011.

In summary SCIAMACHY's adaption to the new ENVISAT orbit was successful such that the high optical and operational performance from the nominal mission phase is expected to be also accomplished in the mission extension until the end of 2013.

### 3. Atmospheric Remote Sensing – Retrieval Methods

#### 3.1 Formaldehyde and Glyoxal in the Operational SCIAMACHY Processor

*S. Hrechanyy, K. Kretschel, G. Lichtenberg, M. Meringer, I. De Smedt (BIRA-IASB), F. Wittrock (IUP-IFE)*

Formaldehyde (HCHO) and glyoxal (CHOCHO) are formed during the oxidation of volatile organic compounds (VOCs) emitted by plants, during fossil fuel combustion, and biomass burning. Due to a rather short lifetime of formaldehyde and glyoxal, their distribution represents the emission fields of their precursors, VOCs. They can support global and local studies of air quality as well as VOC emission.

Including HCHO and CHOCHO in the suite of operational SCIAMACHY products was therefore highly recommended by the Quality Working Group (QWG) and put onto the agenda for the new level 2 processor version 6. In 2010 the implementation of both new trace gases continued and reached its final steps.

The reference algorithms were developed by the Belgian Institute for Space Aeronomy (BIRA-IASB) for formaldehyde (*De Smedt et al. 2008*) and by the Institute of Environmental Physics (IUP-IFE), University of Bremen for glyoxal (*Vrekoussis et al. 2009*), respectively. Both species are retrieved exploiting the DOAS technique (*Platt 1994*). To correct retrieved slant column densities (SCDs) for fitting artifacts, the reference sector method is applied. It includes subtracting the mean slant column of the corresponding gas in a chosen reference sector (Pacific Ocean) from all SCD of the day and replacing it by the background. This background value is either taken from the 3-D Chemistry Transport Model (CTM) IMAGES (*Stavrakou et al. 2009*) in case of formaldehyde, or constant in case of glyoxal. The corrected slant columns are then converted into the vertical column densities (VCDs) using airmass factors (AMFs) calculated by the radiative transfer model LIDORT. The retrieval settings for both species are listed in Table 3-1.

Setting	Formaldehyde (HCHO)	Glyoxal (CHOCHO)
Sun reference	azimuth scanning mirror (ASM)	azimuth scanning mirror (ASM)
Fitting window	328.5-346 nm (channel 2)	435-457 nm (channel 3)
Cross-sections	HCHO, NO <sub>2</sub> , O <sub>3</sub> , BrO, OClO, Ring, Polarization, Undersampling	CHOCHO, NO <sub>2</sub> , O <sub>3</sub> , O <sub>4</sub> , H <sub>2</sub> O, Ring, Phytoplankton
Reference sector correction	Pacific (140° W – 180° W)	Pacific (160° W – 180° W)

Table 3-1: Retrieval settings for formaldehyde and glyoxal

The tropospheric distribution of both gases together with their screening by clouds affects the SCIAMACHY measurements. Only pixels with a cloud fraction < 0.4 represent really measured columns. As for the pixels with higher cloud fraction, their VCDs are predominantly based on the climatological data.

In order to verify the success of the implementation the results obtained by the operational processor required comparison with those from the reference algorithm. Ten full days were chosen for this comparison (five days in 2006 and five days in 2009). The test samples were picked from different seasons ensuring a representative set. In total, the verification set consisted of 136 orbits. Since the implementation of the glyoxal retrieval was not yet finalized only one day in 2006 (13 orbits) was used for the algorithms' comparison. However as soon as the implementation reaches the final phase, the full verification using all 136 orbits will be executed. The scatter plots together with the absolute difference histograms are presented in Fig. 3-1 (HCHO VCDs) and Fig. 3-2 (CHOCHO SCDs). The comparison of the results obtained with the reference algorithms and with the SGP V6.0 revealed slight discrepancies. The

mean difference amounts to  $\sim 7 \times 10^{14}$  molec  $\text{cm}^{-2}$  for the formaldehyde total columns and to  $\sim 2 \times 10^{14}$  molec  $\text{cm}^{-2}$  for the glyoxal slant columns. In both cases this corresponds to an uncertainty of about 10%. The disagreement in the formaldehyde product can partly be explained by the use of a different albedo climatology in the reference and the operational algorithms as well as the slightly different manner how the reference sector correction is applied. Nevertheless, the revealed bias is acceptable. It is within the current accuracy of the method, which is 30% in the best case (*De Smedt et al. 2008*). Taking this into account, the SQWG already decided to consider the formaldehyde total columns as verified.

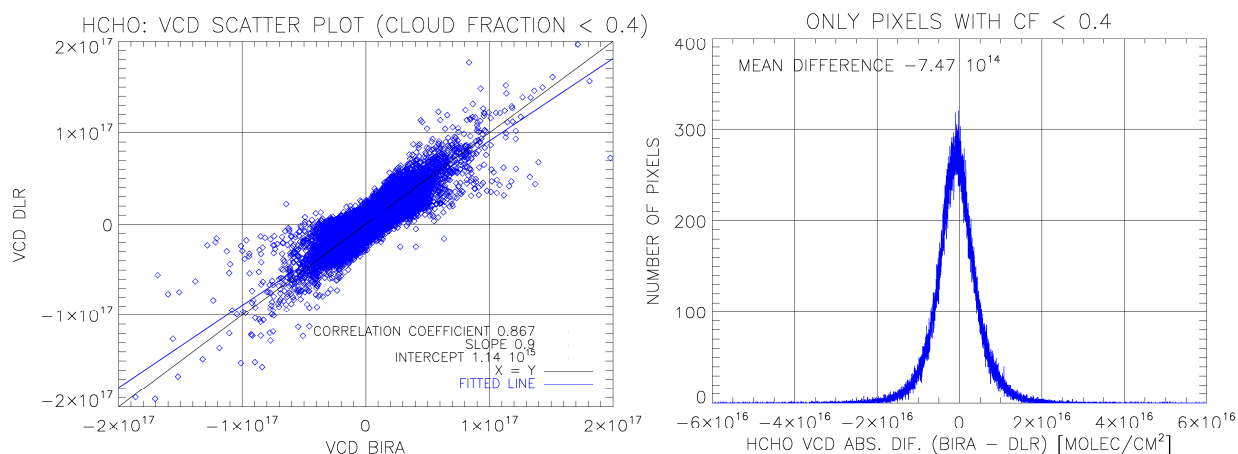


Fig. 3-1: The scatter plot and the absolute difference histogram for the total columns of the formaldehyde.

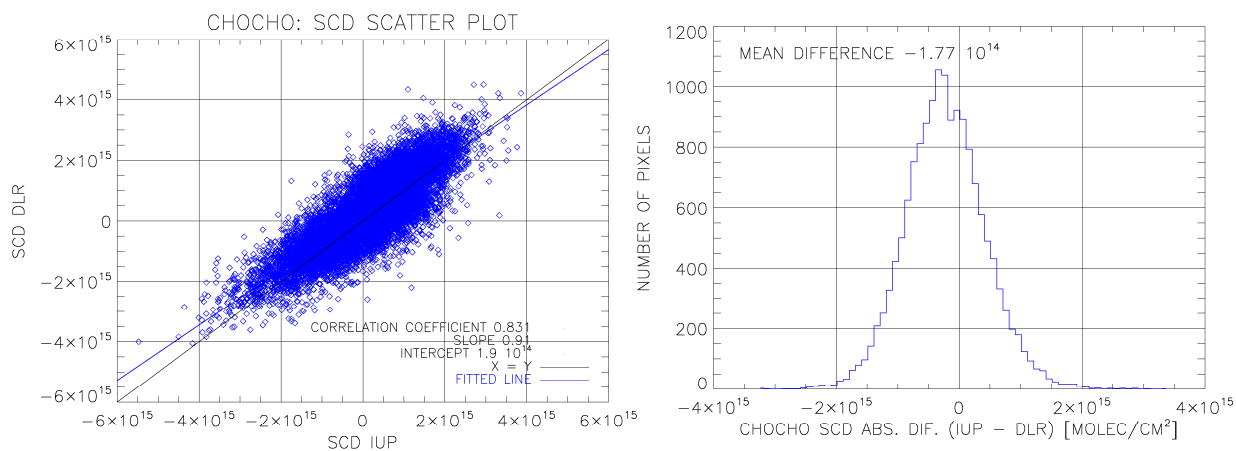


Fig. 3-2: Same as for Fig. 1 but for the slant columns of glyoxal.

The glyoxal retrieval verification revealed that only a small change in the processor code (quality flag format) is needed to proceed further to the corrected slant columns stage. Once this is accomplished air mass factor and subsequent calculation of the vertical columns can be achieved. The final product is expected in the next version of the SGP (V6.0).

### References

*De Smedt, I., Müller, J.-F., Stavrou, T., van der A, R., Eskes, H., and M. Van Roozendael: Twelve Years of Global Observation of Formaldehyde in the Troposphere Using GOME and SCIAMACHY Sensors, Atmos. Chem. Phys., 4947-4963, 2008*

*Platt, U.: Differential optical absorption spectroscopy (DOAS), Chem. Anal. Series, 127, 27-83, 1994*

Stavrakou, T., Müller, J.-F., De Smedt, I., Van Roozendael, M., van der Werf, G. R., Giglio, L., and A. Guenther: Evaluating the performance of pyrogenic and biogenic emission inventories against one decade of space-based formaldehyde columns, *Atmos. Chem. Phys.*, 1037-1060, 2009

Vrekoussis, M., Wittrock, F., Richter, A., and J. P. Burrows : Temporal and spatial variability of glyoxal as observed from space, *Atmos. Chem. Phys. Discuss.*, 9, 8993-9042, doi:10.5194/acpd-9-8993-2009, 2009

### 3.2 Operational and Scientific Limb Retrieval for SCIAMACHY

A. Doicu, B. Aberle, S. Hrechanyy, G. Lichtenberg, M. Meringer

A scientific processor for retrieving atmospheric parameters from SCIAMACHY limb measurements has been developed based on the same retrieval method as pursued in the operational processor, but without the strict requirements for computation speed. It uses as a forward model, the Picard iteration model, and as an inversion model, direct and iterative regularization methods. In contrast, the operational processor uses an approximate forward model with a multiple scattering correction and Tikhonov regularization with a constant value of the regularization parameter.

Due to the strict requirements regarding the computation time, the off-line processor of the SCIAMACHY instrument operates with several approximations. These approximations are incorporated in both the forward and the inversion models. Their impact is as follows.

The main simplification in the forward model concerns the treatment of the multiple scattering. At the a priori state  $X_a$  we compute the signal measured by the detector  $I(X_a)$  with a radiative transfer model for a pseudo-spherical atmosphere and in independent pixel approximation. The correction factor for the effect of multiple scattering is defined by

$$c_{ms}(X_a) = \frac{I(X_a) - I_{ss}(X_a)}{I(X_a)}$$

where  $I_{ss}(X_a)$  is the single scattering term. In the inversion process we use the representation

$$I(X) = I_{ss}(X)[1 + c_{ms}(X_a)]$$

where  $X$  is the actual atmospheric state. Thus, only the single scattering term accounts on the actual atmospheric state. This approximation is valid if the a priori state is sufficiently close to the true atmospheric state. Note, that not only the forward model but also the Jacobians are affected by the multiple scattering approximation.

The regularization method which is used in the inversion process is the Tikhonov regularization (Tikhonov and Arsenin 1977) with an a priori regularization parameter meaning that the regularization parameter, which should balance the residual and the constraint, is chosen in advance and is not correlated with the true measurement. The a priori selection of the regularization parameter is performed for synthetic data, and therefore the method appears to be a risky approach when the measurement is affected by large systematic errors.

Because the scientific processor is a 'counterpart' of the off-line processor not being limited by any time constraints, more accurate, i.e. time-consuming approaches can be implemented. This processor uses the Picard iteration method to simulate the radiance field in a full spherical atmosphere and includes polarization as well as Ring effects. A large class of regularization methods as for instance, the Tikhonov regularization, the iteratively regularized Gauss-Newton method, the regularizing Levenberg-Marquardt method, the asymptotical regularization approach and the regularized total least-squares method can be used for specific applications.

#### Pointing Error Correction

The SCIAMACHY ozone profiles retrieved both by the scientific and the off-line processors are shown in Fig. 3-4 together with the corresponding ground-based LIDAR profile measured during the satellite overpass at Tsukuba, Japan.

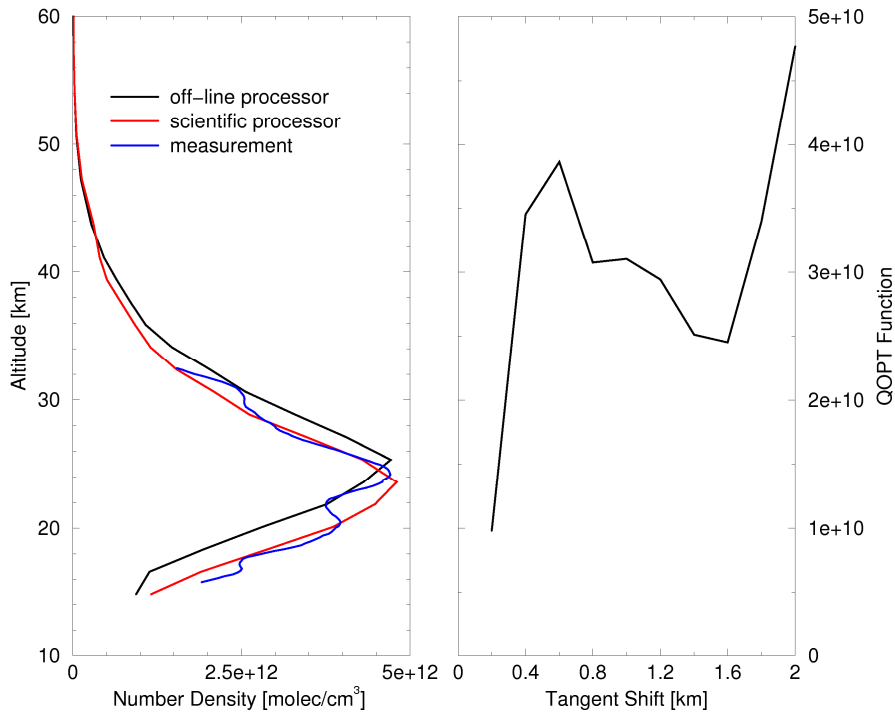


Fig. 3-4: Left: SCIAMACHY ozone profile compared with the profile measured by ground-based LIDAR at Tsukuba on December 11<sup>th</sup>, 2006. Right: the discrete quasi-optimality function.

Comparing the measured profile and the profile retrieved by the off-line processor one can recognize the pointing error causing an altitude shift of the retrieved profile. In the scientific processor the altitude shift is treated by using the quasi-optimality principle introduced in (Tikhonov and Glasko 1964; 1965). Namely, if  $x_{\Delta h}^{\delta}$  is the retrieved profile corresponding to the altitude shift  $\Delta h$ , then the optimal value of  $\Delta h$  is given by

$$(\Delta h)_{opt} = \arg \min_{\Delta h} \left\| \Delta h \frac{dx_{\Delta h}^{\delta}}{d\Delta h} \right\|^2$$

Fig. 3-5 is a graphical illustration of the idea expressed in the equation listed above.

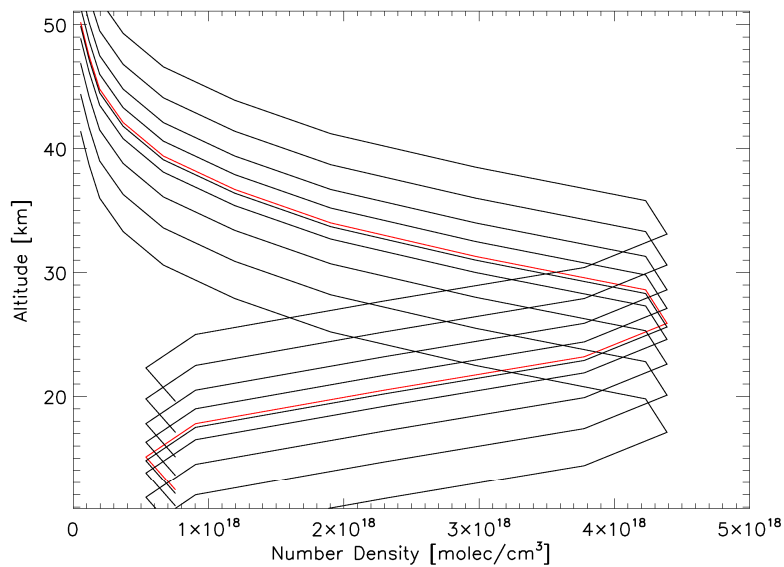


Fig. 3-5: Set of profiles retrieved assuming different  $\Delta h$ . The profile corresponding to the local minimum of the quasi-optimality function is shown in red.

For a set of  $\Delta h$  values a set of profiles is retrieved. Every next profile is shifted relative to the previous one by  $dx_{\Delta h}^{\delta}$ . For the profile retrieved with optimal  $\Delta h$  its shift relative to the previous one becomes smaller than for other ones. This corresponds to the local minimum of the optimality function expressed as

$$QOPT\_Function = arg \min_{\Delta h} \left\| \Delta h \frac{dx_{\Delta h}^{\delta}}{d\Delta h} \right\|^2$$

In practice, a discrete version of the quasi-optimality criterion is used, where we compute the regularized solutions for a discrete set of  $\Delta h$  values and calculate the derivatives by using finite-differences.

#### Addressing the Underregularization Problem

The curves in Fig. 3-6 illustrate that the profile retrieved by the off-line processor is underregularized, i.e. the value of the regularization parameter is too small. To deal with this problem the scientific processor uses an a posteriori parameter choice method, namely the nonlinear discrepancy principle. The steps of this criterion for parameter selection can be summarized as follows:

- Solve the inverse problem without regularization and estimate the noise level  $\Delta$  as the nonlinear residual at the last iteration.
- Solve the inverse problem for several discrete values of the regularization parameter  $\alpha_k$  and store the corresponding nonlinear residuals  $\|y^{\delta} - F(x_{\alpha_k}^{\delta})\|$
- Select the optimal solution  $x_{\alpha_{k^*}}^{\delta}$  corresponding to the first index  $k^*$  for which

$$\|y^{\delta} - F(x_{\alpha_k}^{\delta})\| \leq \tau \Delta$$

where  $\tau \Delta = (1.1..1.2)$  is a control parameter.

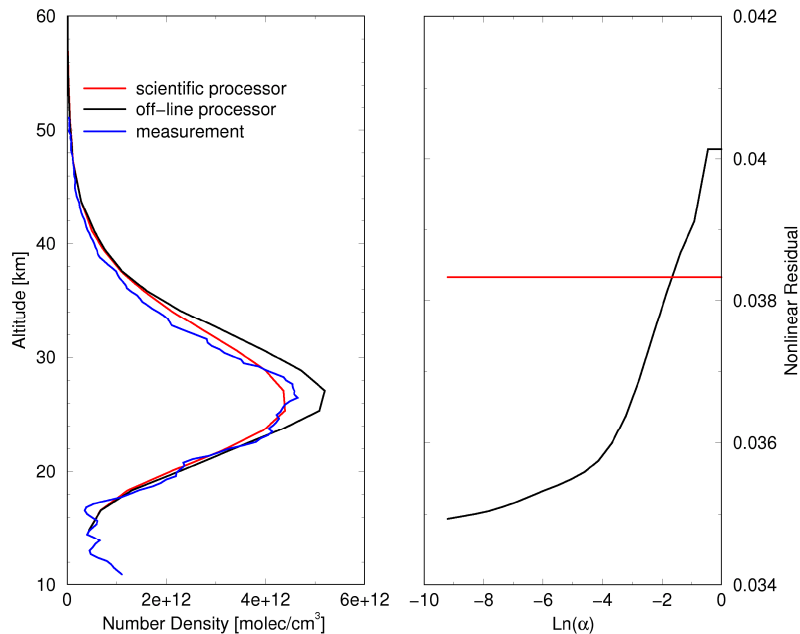


Fig. 3-6: Left: Same as left panel in Fig. 3-4, but for Mauna Loa on 13 October 13<sup>th</sup>, 2006. Right: nonlinear residual together with the noise level.

Once sufficient progress is made in CPU speed, the described improvements shall be transferred from the scientific to the operational processor environment.

## References

Tikhonov, A. and Glasko, V.: The approximate solution of Fredholm integral equations of the first kind, Zh. Vychisl. Mat. Mat. Fiz. 4, 564-71 1964

Tikhonov, A. and Glasko, V.: Use of the regularization method in non-linear problems, USSR Comput. Math. Math. Phys. 5, 93-107, 1965

Tikhonov, A. and Arsenin, V.: Solutions of Ill-Posed Problems, Wiley, New York, USA 1977

### 3.3 SCIAMACHY Level 2 Fast Delivery Service Timeliness

G. Lichtenberg

Remote sensing data are used for different applications having different requirements. While forecasting needs data availability shortly after sensing of the data, climate research and other longer term scientific applications rely more on optimal data calibration and retrieval. In order to satisfy both requirements, two separate processing chains were set up: the Fast Delivery (FD) of level 2 products (Table 3-2) and the offline (OL) level 1b-2 processing chain. While the processors used for both chains are identical, the input data are different. The time requirements for the FD chain do not allow to process and the inventory all the calibration data and to calculate attitude corrections. The standard data slicing of the level 0 product is also omitted. The main differences between the processing chains are:

- *Delivery time*: The goal for the FD products is to deliver them within 24 hours after sensing. Offline data are delivered 1-2 weeks after sensing.
- *Start/Stop times*: OL products contain one orbit always starting at the ANX (Ascending Node Crossing) while FD data do not need to fulfil this requirement. They may contain data from different parts of the orbit.
- *Geolocation*: The geolocation differs slightly since the restituted attitude information for the platform is only available a few days after sensing, i.e. it cannot be used in the FD chain.
- *Calibration Data*: In the FD chain the latest available in-flight calibration data are used while in the OL chain the most recent calibration data made just before the measurement are applied.

Product	Version 5.01 (from 2010)
<b>Nadir</b>	
<b>O<sub>3</sub></b>	Vertical Column Density (VCD)
<b>NO<sub>2</sub></b>	VCD
<b>SO<sub>2</sub></b>	VCDs for volcanic and anthropogenic scenario
<b>OClO</b>	Slant Column Density (SCD)
<b>BrO</b>	VCD
<b>H<sub>2</sub>O</b>	VCD
<b>CO</b>	VCD
<b>Aerosol</b>	Absorbing Aerosol Index
<b>Cloud Parameters</b>	Cloud Top Height, Cloud Optical Thickness, Cloud Fraction
<b>Limb</b>	
<b>O<sub>3</sub></b>	Profile Values
<b>NO<sub>2</sub></b>	Profile Values
<b>BrO</b>	Profile Values
<b>Cloud</b>	Height resolved information about water clouds, ice clouds

Table 3-2: Geophysical Parameters in the level 2 FD products.

### Timeliness of the Fast Delivery Processing

Fast Delivery processing started in February 2010 and the first statistics for the timeliness of the data are available. As noted above, the initial goal for the availability of FD level 2 products was 24 hours from sensing. This includes the entire chain, i.e. transmitting the data from the satellite to the ground station, generating the level 0 file, processing from level 0 to level 1b, processing from level 1b to level 2 and finally copying the product to an externally accessible ftp server. The level 0-1b NRT processing in the framework of the FD service is performed by ESA. The resulting products are retrieved by the D-PAC, further processed to level 2 and subsequently put on an ftp server for easy user access. Fig. 3-7 shows how fast the level 2 data is made available, defined by the parameter *delivery time*, which is the time difference between the sensing stop (time of the last observation in the product) and the modification time of the file on the ftp server.

FD Level 2 Products Timeliness: Timeseries Februar 2010 - November 2010

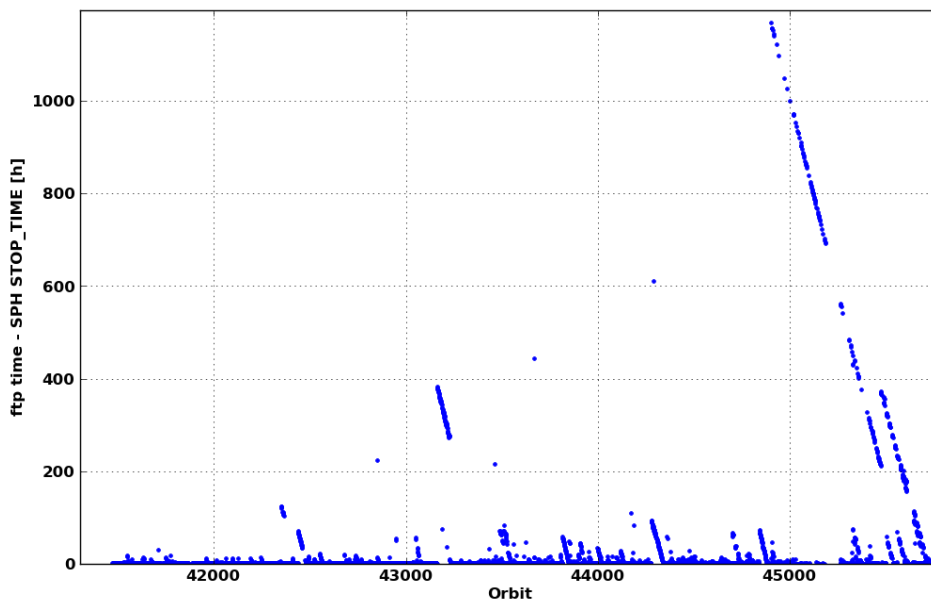


Fig. 3-7: Delivery time for FD Level 2 products as a function of orbit number.

FD Level 2 Products Timeliness: Timeseries Februar 2010 - November 2010

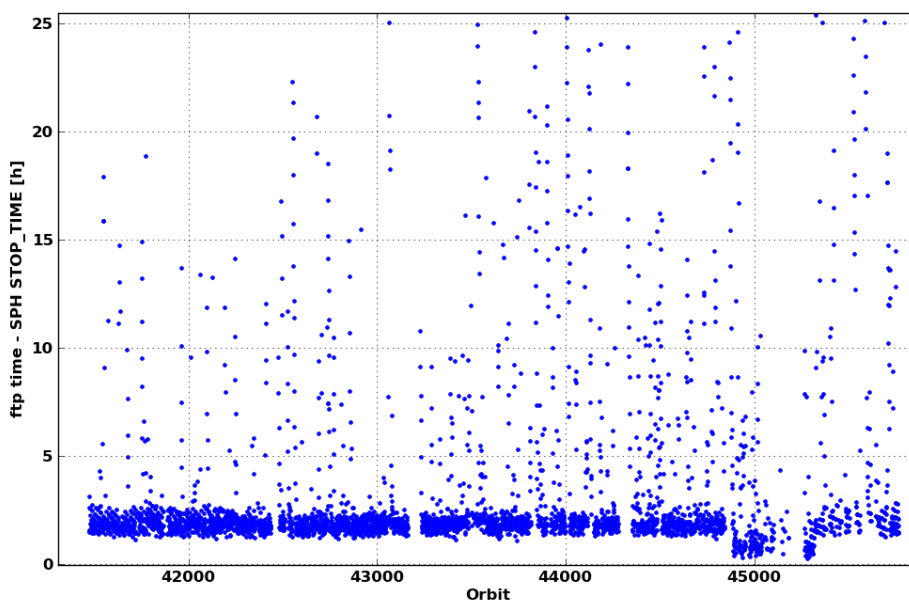


Fig. 3-8: Zoom-in version of Fig. 3-7. For most orbits the delivery time is below 3 hours.

Although for some products and limited time periods the delivery time exceeds 24 hours a more detailed analysis confirms that the majority of files is available within 6 hours from sensing (Fig. 3-8). About 80% of the more than 4200 products generated so far meet the goal of delivery within 24 hours. The median time for delivery amounts to 2 hours. Fig. 3-9 illustrates the statistics for delivery times using 15 minute bins.

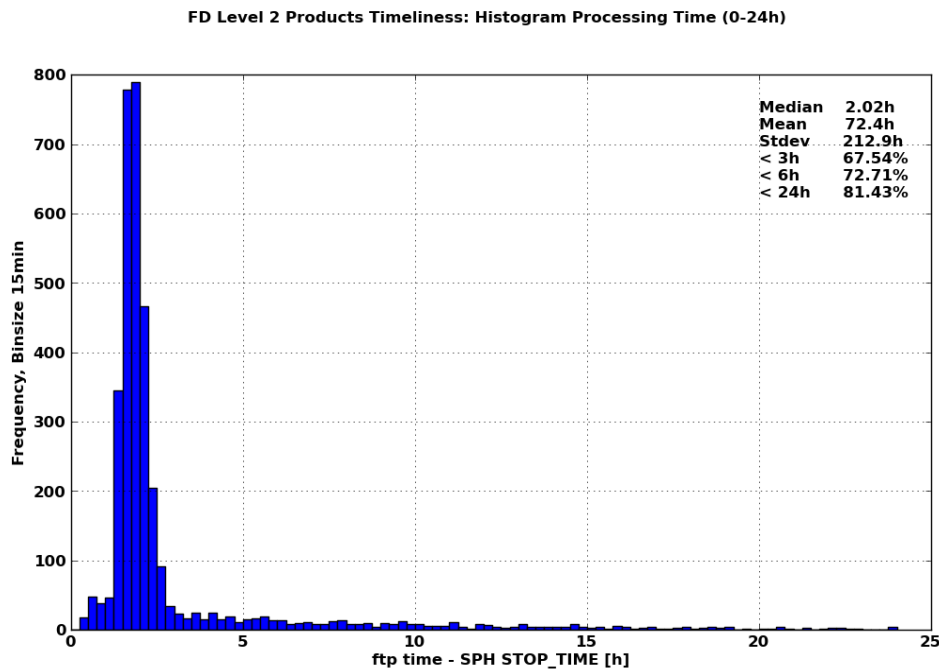


Fig. 3-9: Statistics for the delivery time of FD products. Two thirds of the 4239 products were available within 3 hours from sensing. For nearly 82% of the product the goal of a delivery within 24 hours was achieved.

The pure processing time of an orbit from level 1b to level 2 spans only a few minutes up to at most 30 minutes. However, this does not consider waiting times for input data files, time needed to transfer products from and to the archive, etc. For the level 2 FD processing the inputs are the level 1b files and the m-factor file. The latter contains factors needed to correct the degradation of the instrument in the orbit. They are calculated weekly and delivered to the processing centres.

Generation of the level 1b NRT products occurs at ENVISAT processing centres at ESRIN and Kiruna from where the resulting level 1b data are transferred to the D-PAC for further processing within the fast delivery chain. For the time period from November 23<sup>rd</sup>, 2010 to December 1<sup>st</sup>, 2010<sup>1</sup> we analyzed how much time was required until the level 1 file became available and how long it took from the availability of the level 1b file to the availability of the level 2 file (Fig. 3-10). It can be seen that for most of this period, the availability of the level 1b file determines the delivery time of the fast processing chain. Only in early December (orbit number > 45750), the delivery of level 2 files needed significantly more time although level 1b products were available. The reason was an overload of the ftp server due to individual users that opened too many parallel sessions. Once this problem was solved, the fast level 2 availability was re-established. In the selected time period the level 1b input files took a long time before being available at the D-PAC (peak in Fig. 3-7 above orbit 45000). The reason for this behaviour could be related to the fact that the level 0-1b processing requires many auxiliary files as input which were possibly delayed.

<sup>1</sup> Note that the NRT level 1 files are not kept on the server, such that an analysis for the whole period was not possible.

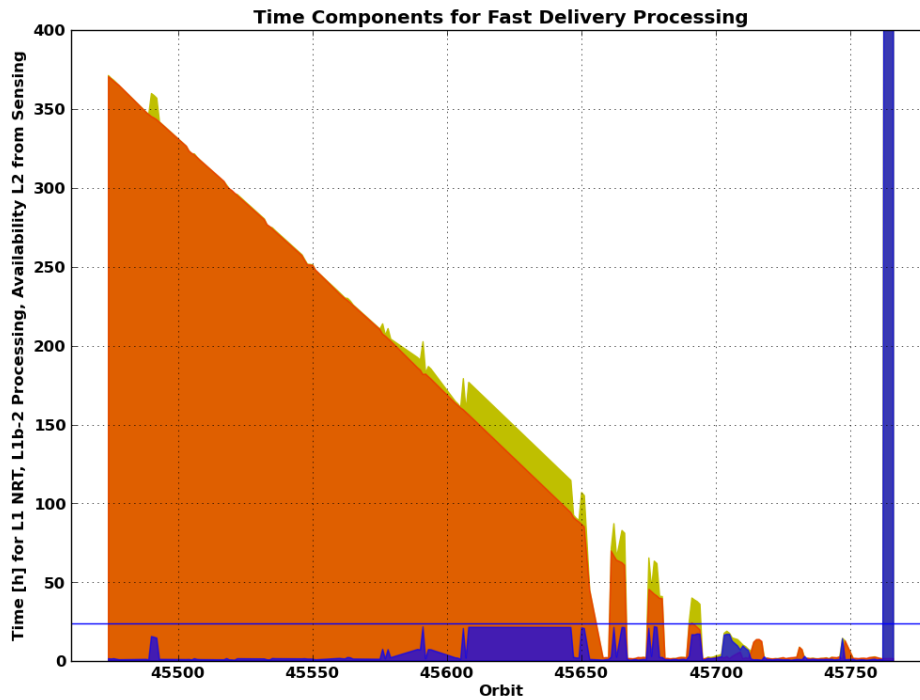


Fig. 3-10: FD availability between November 23<sup>rd</sup>, 2010 and December 1<sup>st</sup>, 2010. Shown is the time between sensing stop and availability of the level 1b file (red), the processing time for level 1b-2 (blue) and the total time after a level 2 product is available (green), which is the sum of the two. The horizontal line marks the 24 hours delivery goal.

### 3.4 Migration of the SCIAMACHY Level 2 Processing Development Environment

*D. Scherbakov, M. Meringer, G. Lichtenberg*

During the last year a change of Level 2 processor's target platform and development environment away from the original 32-bit architecture and the SNIFF+ IDE was prepared. The reasons for the change are:

- The SNIFF+ version used is outdated and no longer maintained.
- RCS, the revision control system used by SNIFF+ has several disadvantages and is outdated (see below)
- The arrival of 64-bit consumer computers with their advantages for processing large amount of data makes it possible to migrate the processor to 64-bit architectures without more cost and with gain of processing speed.

Up to version 5 of the offline level 2 processor, the SNIFF+ IDE (integrated development environment) is used to develop the processor. SNIFF+ is a software suite that integrates the version control (using RCS), generation of makefiles to build the processor and other features under a graphical user interface. The SNIFF version used was acquired at the start of the processor development and is now outdated. While an update to a newer version would have been possible, the complicated handling of a large project within SNIFF+ led to the decision to migrate to a freely available and widely tested software solution consisting of *Subversion* as version control system and *CMake* as the build environment. At the same time the move to 64-bit systems was decided.

#### **Migration of the Version Control System**

A version control system is one of the important building blocks for successfully accomplishing projects. It is almost the first item one should start thinking about when beginning a new project or want improving an existing one. It is something that works flawlessly in the project background and at the same time makes teamwork possible when the team consists of tens, hundreds and even sometimes thousands of individuals.

All files of a project are kept in a repository together with information when a file was changed and who did the change. The repository allows going back to earlier versions and to transparently evolve the project. Version control has the following basic concepts:

- *Repository*: The repository holds all files of the project (note that the files can be of any kind, e.g. source code, documents, binary files etc.)
- *Check Out*: A check out copies files of a certain revision to the users working environment. The user can then change, add or delete files.
- *Commit*: A commit by an user copies the changed file(s) back to the repository together with the author name, the date and an optional comment by the user describing the change
- *Trunk*: This is the main development area in the repository. Official releases are usually made from the trunk.
- *Revision (number)*: For each commit by users, a revision number is incremented. A revision consists of all files in the project at a certain point in time. All revisions can be again checked out by users that have access to the repository. The user will then have an exact copy of the project at this revision (i.e. point in time).
- *Branch*: A branch in the repository constitutes a copy of a set of files from the trunk. After branching, the branch can be developed independently from the trunk. This can be useful if e.g. a new feature shall be tested or included in a future version of the software, but not yet in the next release. Changes made in one branch can be merged back into the trunk to include them in a release.
- *Tag*: In order to simplify handling of the repository, the user can make a snapshot of the repository at an arbitrary point of time and 'tag' it with a meaningful text. One example is to provide tags for each delivered version of the software. This facilitates going back to a certain version, check it out and e.g. debug it.

In the early days of the SCIAMACHY processor development back in the mid-90s there was almost no other possibility for a project willing to do revision control but to use RCS (Revision Control System) or its successor – CVS (Concurrent Versioning System). These systems were de-facto a standard due to popularity gained because of publicly available source code and a long development and improvement history. RCS was introduced in 1982 (*Tichy 1985*) as an open-source alternative to then-popular Source Code Control System (SCCS). CVS at the beginning was just a set of scripts which helped developers to manage RCS projects as a whole. CVS takes its roots from a source code published in 1986 (*Grune 1986*) to a UseNet group. Four years later in 1990, CVS version 1.0 was submitted to the Free Software Foundation for development and distribution.

Free availability of RCS and CVS attracted many supporters and developers. This resulted in a large number of tools and add-ons available for RCS and CVS projects. When the development of SCIAMACHY processors began, RCS was chosen as a system for a code revision control because it was the best choice.

#### RCS/CVS Deficiencies

Any project that uses RCS/CVS will have to decide how to deal with the following peculiarities:

- Revision control is performed on a per-file basis. Each file during commit has to be modified individually. This means files from one commit will probably have different modification times. When reconstructing how the whole source tree was changed, no method exists of telling if it was in one or more commits with the same comment.
- Telling where one commit ends and another starts remains uncertain.
- If a file is moved to another location or just renamed, determining who its predecessor becomes impossible.
- Deletion of a file keeping all change history is cumbersome.
- When creating a tag, one has to modify every file. If one file was originally omitted from tagging and only included afterwards, no means exists for telling if it was originally tagged or not.

In summary any RCS/CVS repository is just a collection of files, where each file keeps its own change history, sometimes with tags. Likewise a RCS/CVS change log is no more than just a list with two columns: commit date/time and filename.

### Roadmap to Subversion

These problems accompanied by a more and more outdated and unsupported GUI front-end SNIFF+ accelerated transition to Subversion (SVN) for SCIAMACHY software development. As a main component that will perform migration it was decided to use rcs2svn.pl Perl script and to modify it such that it fulfills the following goals:

- Migration to SVN should be performed as smooth as possible with a minimum downtime for project developers. RCS and SNIFF+ will be used until all tests show that both RCS and SVN versions of the processor produce the same results. This means that work will be done in parallel.
- RCS should be imported into SVN trunk. Changes necessary for migration should be done in a separate SVN branch.
- Some developers continue working on enhancements for a SCIMACHY processor and will be committing changes into RCS. The others will be writing tests and preparing final migration to SVN and committing their work to a newly created SVN branch. This means that at some point in time:
  - There might be a need to re-import new changes from RCS into the existing SVN repository.
  - A new SVN repository might need to be created and all changes from an old SVN repository should be imported into a new one. Thus the script should be able to emulate user activities (SVN add, delete, change, move, commit, etc.) because there is currently no tool to automatically migrate changes from one SVN repository to another.
- When merging changes from RCS and SVN into a new SVN repository commits from RCS and SVN should be sorted by date and committed accordingly to show that development was done simultaneously.
- The script should also be able to:
  - start or stop import at a particular date
  - continue operation from where it stopped
  - pause on particular date or SVN revision before they are committed into SVN
- If an unrecoverable error is found, the script should be able to stop and give an operator a possibility to fix it. There should be no need to abort and restart migration.
- As noted above no information exists about which change belongs to which commit. Hence the script should be able to automatically group changes to different files into single commits. Several changes to a single file must not be grouped.
- If possible the script should be capable of commit re-ordering to reduce number of commits needed (see Fig. 3-11).
- When a repository has RCS/CVS tags, the script should:
  - Identify files that are no longer used and delete them automatically. Candidates for deletion are files that have no changes in the future and are not present in any tag in the future.
  - Create appropriate tags in a /tags SVN directory.
  - When a tag is created, check that it contains only files that belong to this tag.
  - Check that revisions of files in a tag match tag requirements. If a file revision should be lower, copy over needed file version from SVN. If a file revision should be higher, overwrite this file with a version that will be submitted to the repository in the future.
  - By means of a lookup table keep track of RCS and SVN revision associations, i.e. which RCS revision corresponds to which subversion revision, for each file. Be able to identify, when a particular RCS revision was submitted into a SVN repository, and which SVN revision corresponds to it. If a lookup table has no entry for some revision pairs, be able to automatically query the SVN repository to fill in the gaps.

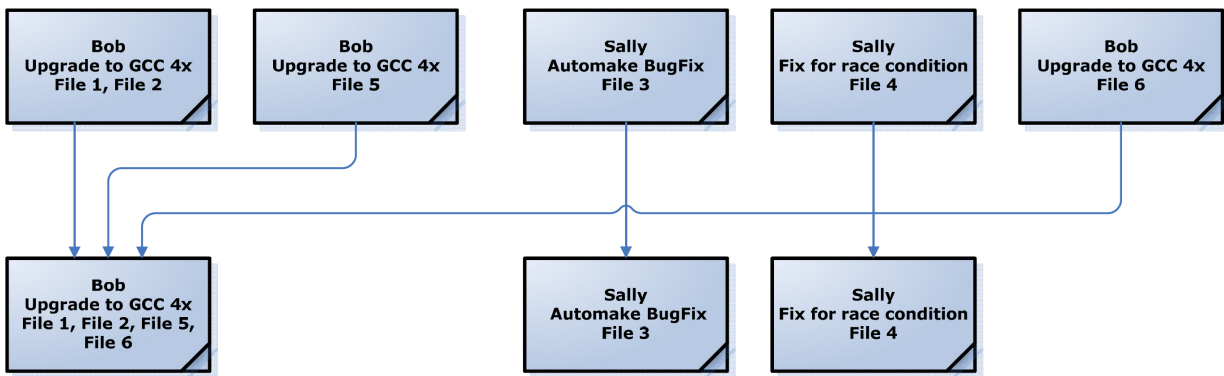


Fig. 3-11: Upper row indicates changes sorted ascending by date and time from left to right how they appear in RCS/CVS. Lower row represents order, how they should be submitted into a SVN repository. Here examples of commit grouping (Files 1, 2 and 5) and commit reordering (File 6) are shown.

By the end of 2010 the majority of the work has been completed. The `rcs2svn.pl` script has grown from a small program with only a few capabilities to a full-blown RCS/CVS to SVN migration application skilled enough to handle projects of almost every size. When the last step will be done, i.e. finalization of coding in RCS and comparison testing, the whole new world of revision control with SVN is accessible.

### **Getting Ready for 64-bit Processing**

The first 64-bit computer was delivered to a customer already back in 1962. However it took more than 40 years until 64-bit processing reached the consumer market. Nowadays almost any x86-compatible system is capable of 64-bit processing. Even when not using this functionality because of running a 32-bit Operating System (OS), it still resides on the chip.

#### **64-bit benefits and tradeoffs**

Usually programs run smoothly on 32-bit machines. However porting to 64-bit OS has become an ever growing activity. Why is this extra work done? Major advantages of 64-bit systems are:

- 64-bit processors have more internal registers. This means that if at one point in time one has to handle large amounts of data one can perform computations for a much longer time before using time-consuming memory operations. This is particularly important for scientific computations.
- One SCIAMACHY level 1b orbit generates about 300 megabyte of data. Although not the whole level 1 product is loaded into memory at once, processing this amount of data requires (temporarily) much more than 300 MB, because e.g. climatologies, topographical databases etc, have to be read in. On 32-bit machines the maximum memory is 4GB. As soon as this limit is violated, data are temporarily stored on the hard disk until they are needed. Since read/write access on the hard disk is much slower than memory access, the processing speed is substantially lowered in this case. Therefore the current theoretical limit of a 64-bit address space of 4 petabytes comes really in handy. It is 65536 times bigger than the maximum limit of a 32-bit machine which is 4GB.

The main disadvantage of 64-bit architectures is that relative to 32-bit architectures, the same data type occupies more space in memory (see table below).

#### **ILP32 vs. LP64**

When porting an application from 32- to 64-bit some data-types can change their size. This is especially important when one relies on sizes for reading and writing binary files or performing a bit shift. The data-type length model for 32-bit applications is ILP32. This name refers to the fact that *int*, *long* and *pointers* are of the same size, i.e. 32 bits. On 64-bit OS the model is LP64. Here *long* and *pointers* grow in size to 64-bits. Table 3-3 lists how the same data-type might differ in size on various processors:

	PowerPC	PowerPC64	x86	amd64	alpha	alpha64
char	1	1	1	1	1	1
short	2	2	2	2	2	2
int	4	4	4	4	4	4
long	4	8	4	8	4	8
long long	8	8	8	8	8	8
float	4	4	4	4	no data	4
double	8	8	8	8	no data	8
long double	16	16	16	16	no data	8

Table 3-3: Sizes of data-type for various processors

*Long* and *long double* have different sizes depending on whether it is a 32- or 64-bit OS and processor. For current 32-bit programs it is not unusual to assume that *int* and *long* are the same in size. It is just this assumption which causes problems in 32- to 64-bit conversion. This problem can be overcome by a special header file `stdint.h` which declares platform-independent data-types with a constant length (Table 3-4). It is particularly useful for cross-platform programming.

Name	Unix/Linux equivalent	Windows equivalent	Signing	Bits	Bytes
<code>int8_t</code>	signed char	signed char	signed	8	1
<code>uint8_t</code>	unsigned char	unsigned char	unsigned	8	1
<code>int16_t</code>	short	short	signed	16	2
<code>uint16_t</code>	unsigned short	unsigned short	unsigned	16	2
<code>int32_t</code>	int	int long	signed	32	4
<code>uint32_t</code>	unsigned int	unsigned int unsigned long	unsigned	32	4
<code>int64_t</code>	long	long long	signed	64	8
<code>uint64_t</code>	unsigned long	unsigned long long	unsigned	64	8

Table 3-4: Data-types in the header file `stdint.h`

A similar approach was chosen for the SCIAMACHY processor, i.e. all data types were defined with a fixed length. Still, the migration from 32-bit version to the 64-bit version made some code changes necessary. The migration also included the move to the latest compiler and standard libraries. In order to check that the migration was successful, 180 level 2 products, the so called verification data set, generated with the 32-bit version were compared to the results of the 64-bit version (see Table 3-5).

Differences smaller than  $10^{-5}$  are generally acceptable and are simply a consequence of the numerical precision of the calculation and the update of the libraries and/or compiler version. Even if a small number of cases is larger than this limit, it is considered acceptable as long as the differences are orders of magnitudes smaller than the retrieval error. Mostly the reasons for larger differences are numerical instabilities of the algorithm under certain conditions. Taking this into account, the comparison showed that the nadir  $\text{SO}_2$  retrievals and all limb retrievals had larger than acceptable differences between the 32-bit and the 64-bit version.

Species	Data Points	Absolute Relative Difference (ARD > 10 <sup>-5</sup> )	Max ARD	Remark
Nadir O <sub>3</sub>	818595	-	-	
Nadir NO <sub>2</sub>	1392300	-	-	
Nadir BrO	825099	80 (0.01%)	0.0006570	VCD
Nadir SO <sub>2</sub>	824939	18008 (2.18%)	0.8020000	<i>Reason: Optimisation of cos() calculation during background database binning</i>
Nadir OCIO	865881	1 (0.00%)	0.0000295	SCD
Nadir H <sub>2</sub> O	1199259	-	-	
Nadir CO (only good pixels)	121245	2 (0.002%)	0.0107213	VCD, flags 0-2, 6-11 true
Clouds & AAI	1669201	688 (0.04%)	0.0077200	CTH only, differences are absolute values in km
Limb O <sub>3</sub>	953186	86213 (9.94%)	0.4420000	Number Density, Values ARD > 10 <sup>-2</sup> found
Limb NO <sub>2</sub>	953186	86953 (10.5%)	0.1000000	<i>Reason: Calculation of π instead of setting as a constant</i>
Limb BrO	944866	78735 (8.33%)	0.8570000	
Limb Clouds	15792	-	-	No differences

Table 3-5: Summary of comparison of SGP 32-bit and SGP 64-bit (ARD = Absolute Relative Difference). Shown is the number of data points, the absolute number of points and the fraction of points with ARD > 10<sup>-5</sup> and the maximum value of the ARD. Dark gray: No or very few differences, light gray: Acceptable number of outliers exists.

Closer investigation of the SO<sub>2</sub> retrieval led to a code sequence

```
float64 diff = cos(day_in_year * d2rad) - cos(db_day_in_year * d2rad);
```

for which the 32-bit version did not compute exactly 0.0 in case of equal values for *day\_in\_year* and *db\_day\_in\_year*. Instead, *diff* is assigned a very small, but nevertheless positive value, which produces an integer error a few lines of code later in

```
new_quality = (int16) ((1 - diff) * old_quality);
```

The *new\_quality* parameter is used as a weight factor in the averaging of background values. This error propagates to the erroneous calculation of a background correction which finally leads to the above described differences. The code was changed and now checks at first whether *day\_in\_year* equals *db\_day\_in\_year* and if this is true, *diff* is assigned 0.0. After this fix vertical column density (VCD) values calculated by both versions were identical.

The limb differences could also be tracked down to a single line of code. In the limb retrieval  $\pi$  was calculated via an *arcsin* function:

```
PI = 2.D0 * DASIN(1.D0);
```

which is mathematically correct, but leads to different values when different compilers with different math libraries are used. Similar to the problem with SO<sub>2</sub> this small deviation in  $\pi$  led to integer errors in another code sequence.

In summary the new development environment employs standard open source tools which are widely used and maintained ensuring that the processor is future proof for the coming years and that building the processor becomes much easier than before.

### References

Grune, D.: Concurrent Version System, a method for independent cooperation, IR 113, Vrije Universiteit, Amsterdam, 9, 1986

Tichy, W.F.: RCS – A System for Version Control, Software – Practice and Experience, 15/7, 637-654, 1985

## 3.5 GlobVapour – an IASI Assessment

M. Hess (RASCIN), A. Doicu, F. Schreier

*GlobVapour* is an ESA project with the objective to provide long-term coherent water vapour data sets from a number of different European and non-European EO missions and from in-situ data. One of these missions is the infrared spectrometer IASI on MetOp. The quality of different water vapour profile algorithms shall be assessed by a comparison of the algorithms using IASI data around radio sonde measurement sites. IMF-AP participates in this comparison with the newly developed data processor VINO based on the line-by-line radiative transfer model GARLIC (Schreier and Schimpf 2001) and the optimization software DRACULA (Doicu et al. 2010).

VINO is a descendant of BIRRA (Gimeno-Garcia and Schreier 2011) which is used in the SCIAMACHY data processor for trace gas column retrievals in the near infrared spectral regions. In contrast to BIRRA, the highly sophisticated DRACULA routines are used for optimization since profile retrievals usually are ill-posed problems, requiring regularization. DRACULA contains different regularization methods such as the *Iterative Regularized Gauss Newton* method (IRGN) or the *Tikhonov* regularization.

The data set calculated for the comparison consisted of all cloud free measurements of July and August 2007 in an area around the Meteorological Observatory Lindenberg. This area contains  $11 \times 11$  IASI pixels centred at Lindenberg, corresponding to a box with a side length of about 130 km. In total, more than 5000 water vapour profile retrievals have been performed. Each of them required about 2 minutes computer time on the IMF-AP department server 'Donau1'. The following retrieval setup was used:

- spectral range: 1308-1337  $\text{cm}^{-1}$  (81 data points)
- atmosphere model: midlatitude summer for  $\text{N}_2\text{O}$ ,  $\text{CH}_4$ ,  $\text{CO}_2$ ,  $\text{O}_3$  and pressure profiles  
radio sonde for temperature profile
- profile resolution: 1 km (up to 12 km) and an end altitude at 50 km
- retrieval method: IRGN with line search

The regularization parameter  $\alpha$  and the *correlation length* were selected manually with respect to a best fit compared to the radio sonde data. As an example, the results of our water vapour profile retrievals for July 8<sup>th</sup>, 2007 are shown in Fig. 3-12 and 3-13. Both figures contain all 121 results inside the box around Lindenberg. The final residuals are in most cases below 20% while the average deviation from the radio sonde data is slightly above 20% (Fig. 3-12). The deviations on individual profile levels can be somewhat higher (Fig. 3-13).

This first application of VINO showed several deficiencies which have to be remedied in the near future. The main improvement will be the application of multiple independent micro-windows, which enables the use of separate spectral regions without the need to calculate the radiative transfer in between. Furthermore, the automatic selection of the regularization parameter  $\alpha$  is desirable for an operational application of VINO.

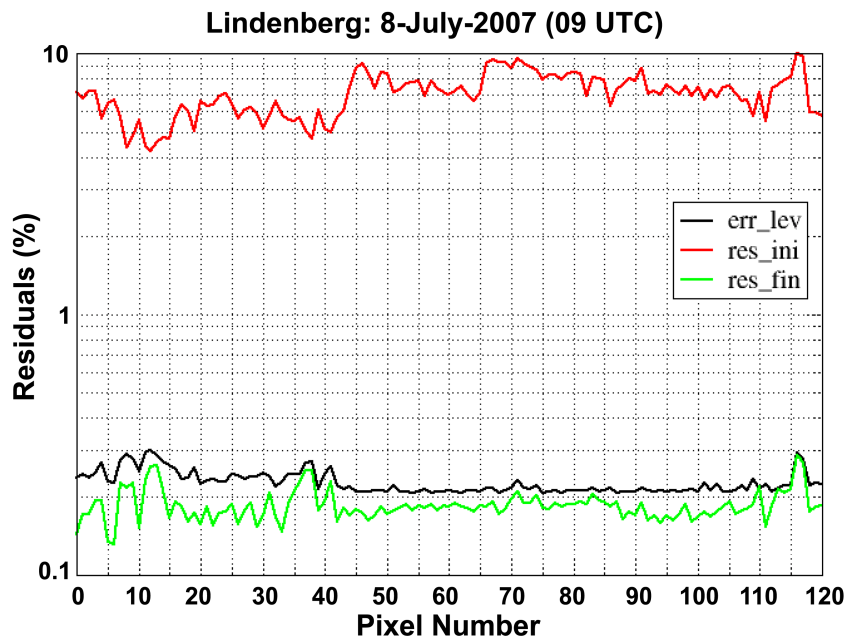


Fig. 3-12: IASI water vapour retrieval results for July 8<sup>th</sup>, 2007 near Lindenberg. Initial (res\_ini), final residual (res\_fin), and deviation from radio sonde data, averaged over profile levels (err\_lev) for all 121 pixels inside the box around Lindenberg.

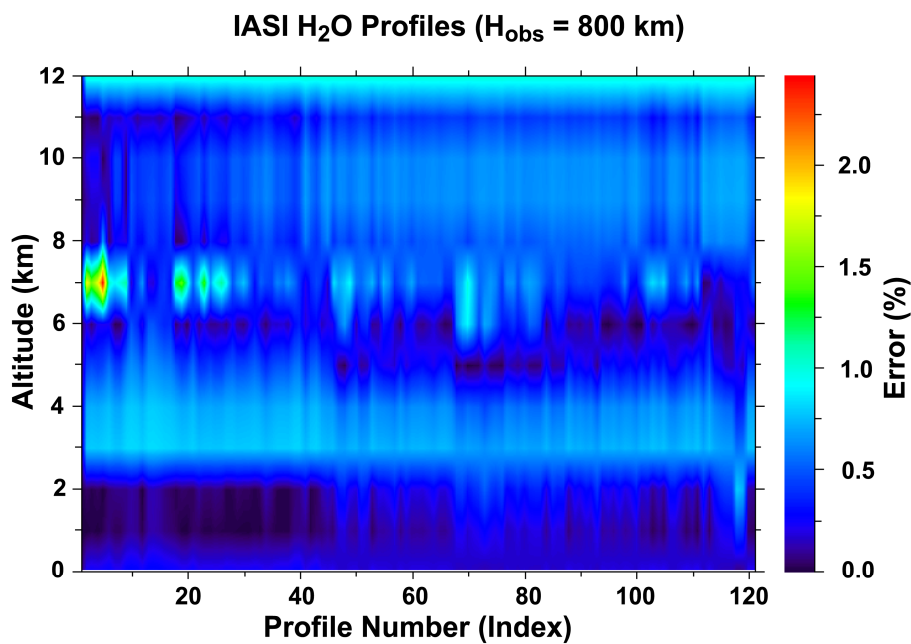


Fig. 3-13: Same retrievals as in Fig. 3-12. Deviation from radio sonde data on profile levels.

References

*Doicu, A., Trautmann, T. and Schreier, F.:* Numerical Regularization for Atmospheric Inverse Problems, Springer and Praxis Publishing, 2010

*Gimeno García, S. and Schreier, F.:* Near Infrared Nadir Sounding of Vertical Column Densities: Methodology and Application to SCIAMACHY, submitted to Atmos. Meas. Tech. Discuss., 2011

*Schreier, F. and Schimpf, B.:* A new efficient line-by-line code for high resolution atmospheric radiation computations incl. derivatives, In W.L. Smith and Y. Timofeyev, Eds., IRS 2000: Current Problems in Atmospheric Radiation, pages 381-384. A. Deepak Publishing, 2001

### 3.6 Results from the Saharan Mineral Dust Experiment 2 (SAMUM-2)

C.H. Köhler, T. Trautmann, E. Lindermeir (IMF-EV)

Mineral dust constitutes a major fraction of the global aerosol burden. It is usually emitted by globally spread arid and barren regions (source regions), the most prominent being the Sahara Desert. Once airborne, the aerosol scatters and absorbs electromagnetic radiation from the UV to thermal infrared (TIR) and emits thermal radiation. This *direct aerosol radiative effect (DRE)* is complemented by an *indirect radiative effect (IRE)*, summarizing the aerosols capabilities to alter the formation, life-cycle and optical properties of clouds in the atmosphere, resulting in modified radiative fluxes. The mineral dust may be airborne several days and is thus subject to disposition covering distances of thousands of kilometers from the source region, e.g. Sahara dust aerosol is regularly transported to Asia, Middle-Europe or the Caribbean. Furthermore, the associated deposition onto the planetary surface impacts the ecosystem at the destination by supplying locally unavailable trace substances, microorganisms or pollutants. The fact that neither DRE nor IRE are scientifically sufficiently understood has spawned several major national and international research projects dedicated to this topic within the last decade. After all, there exists no generally accepted theory to model the radiative properties of irregularly shaped medium sized – compared to the wavelength of the radiation – aerosol particles, which is essential for the interpretation of radiation measurements in the presence of aerosols. As a consequence the products derived from measurements of space-borne and ground-based remote sensing instruments, i.e. the vast majority of quantities derived for monitoring weather and climate, are potentially adversely affected by the presence of aerosols. In order to investigate the impact of aerosols on the remote sensing products in question and to eventually correct for the resulting distortions, an accurate theoretical model describing the interaction of radiation with particles of complex shapes is required.

The Saharan Mineral Dust Experiment is a two-phase project funded by the German Research Foundation (DFG) aiming at the microphysical and radiative properties of pristine mineral dust aerosol (SAMUM-1) and transported mineral dust including admixed biomass burning and maritime aerosol components (SAMUM-2). The first phase included a field experiment in Morocco, the results of which have been published in a special issue of *Tellus 61B (Heintzenberg 2009)*. A publication of the SAMUM-2 findings resulting from the second field experiment conducted at the island of Santiago, Cape Verde, is planned for 2011 (*Ansmann et al. 2011, Köhler et al. 2011*).

The cooperative work of IMF-AP and IMF-EV within the scope of SAMUM-2 is focused on achieving of a radiative closure, which is obtained if the measured radiation at top/bottom of the atmosphere (TOA/BOA) agrees with modelled spectra calculated by a suitable radiative transfer model within the accumulated error of model and measurement. The radiative transfer model used for this purpose requires a large number of input parameters describing aerosols (vertically resolved number concentration, size, shape and refractive index of the aerosol particles) and atmospheric gases (vertical profiles of temperature and gas concentration) within the field of view of the instrument. Since most of the required input parameters are obtained from simultaneous co-located measurements of other SAMUM-2 groups using state-of-the-art techniques and equipment, the uncertainty in the simulated spectra caused by uncertainties in the input parameters for radiative modelling is minimized. In this respect SAMUM-2 is unique, since the multitude of different instrumentation guarantees a thorough characterization of the observed aerosol layers. A sketch of the experimental setup is provided in Fig. 3-14. Of special importance was the deployment of the DLR Falcon research aircraft, which allowed for in-situ sampling of aerosol particles and consequently lead to an accurate analysis of the aerosol microphysical properties.

The spectrally resolved radiation measurements included in this study are obtained from ground based measurements with a D&P Model 102 FTIR and from space borne measurements taken by the IASI FTIR on-board MetOp-A. The Model 102 field spectrometer was set-up at the Praia field site during the SAMUM-2 campaign in close cooperation with IMF-EV, which provided expertise for instrument operation, calibration and characterization. The simulations were carried out by means of line-by-line multi-scattering radiative transfer algorithms provided by the PIRATES radiative transfer library developed within the scope of the SAMUM project (for details on PIRATES see annual report 2009).

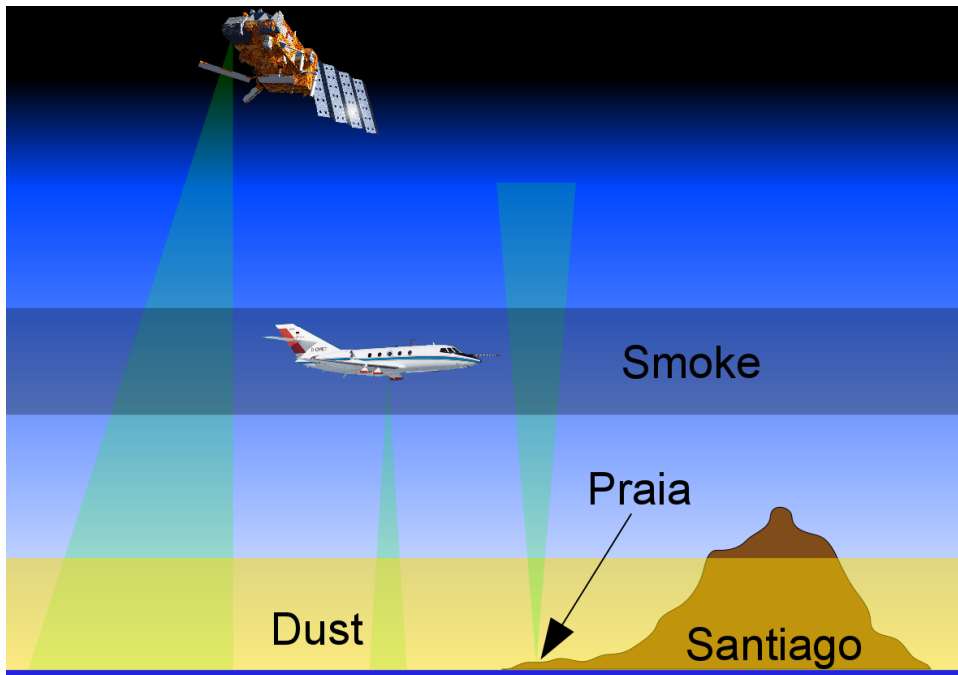


Fig. 3-14: Sketch of the experimental setup deployed during SAMUM-2 on the Island of Santiago, Cape Verde including space-borne, air-borne and ground based measurement platforms. The ground based instrumentation located at Praia included several LIDARs, sun photometers, spectrometers (UV to TIR) and radio sonde ascends. The DLR Falcon aircraft was equipped with a LIDAR and with in-situ particle sampling equipment for size distribution measurements and off-line chemical analysis. Furthermore satellite data obtained from the IASI instrument on-board METOP are used in this study.

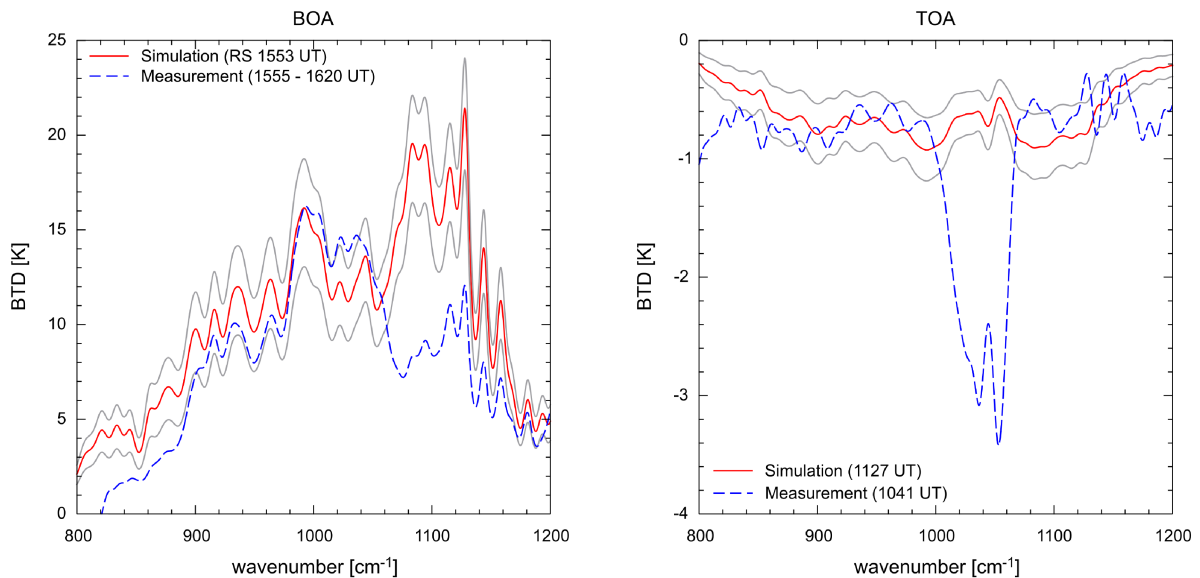


Fig. 3-15: BTDR spectra for simulated (solid) and observed (dotted) data. Differences are towards simulated clear-sky case. Grey lines denote effect of uncertainties in the size-distribution.

It should be noted that all measured spectra represent column integrated data, which means that the spectrum intrinsically accounts for all information obtained from every point inside the field of view of the instrument. Although we are interested in radiation emitted/scattered by aerosols, it is not trivial to separate this radiation from other radiation emitted by gases or the surface. As a result, our simulations have to take into account all matter inside the field of view which interacts with radiation in the observed spectral interval. We then attempt to isolate the aerosol effect by subtracting from each of the simulated and measured spectra a simulated spectrum obtained under the assumption of clear-sky, aerosol free conditions. The resulting spectrum is an estimate of the aerosol DRE. Example spectra of the DRE obtained in this manner during SAMUM-2 in a case study for January 25<sup>th</sup>, 2008 are shown in Fig.

3-15. The aerosol effect is plotted as brightness temperature difference (BTD) between aerosol loaded and clear-sky, aerosol free conditions at BOA and TOA. The situation during this day is similar to that depicted in Fig. 3-14 as far as dust and biomass layers are concerned.

It is obvious that the DRE at BOA is far larger than at TOA (note different scales in Fig. 3-15) due to the fact that the optically dominant mineral dust layer was close to the surface. Thus its temperature is relatively high and creates a high contrast as compared to the cold background of a clear sky when viewed from below. Conversely an observer/instrument looking down at the dust from above has difficulties to discriminate between the warm surface and the only slightly cooler dust layer, resulting in low BTD values observed at TOA. In general simulated and observed aerosol DREs agree well, exceptions being the spectral regions  $1060\text{-}1140\text{ cm}^{-1}$  in the BOA spectrum and  $980\text{-}1080\text{ cm}^{-1}$  in the TOA spectrum. The latter is most probably attributed to ozone profile uncertainties stemming from the fact that no local ozone sonde measurements were performed within the scope of SAMUM-2. The formerly mentioned deviations between measurement and simulations are currently suspected to occur due to effects caused by particle non-sphericity, since our simulations assume spherical particles. Until recently it was generally believed that the assumption of spherical particles leads to correct results for radiative transfer simulations in the TIR, even though the mineral dust aerosol particles display rather irregular shapes. Nonetheless our findings are in accordance with more recent observations, which indicate that particle non-sphericity may not be negligible in TIR spectral regions, where the real part of the refractive index assumes values below unity (cf. *Reststrahlen bands*). It is intended to further investigate the scattering properties of aspherical particles within these spectral bands using the scattering database developed at IMF-AP by *Schmidt et al. (2009)*. Our investigations are intended to identify combinations of complex refractive index, particle geometry and particle size where shape effects play an enhanced effect in the TIR, thus rendering the ideal homogeneous sphere an insufficient optical model.

### References

*Ansmann, A. et al.*: Saharan Mineral Dust Experiments SAMUM-1 and SAMUM-2: What have we learned?, *Tellus B*, 63 (submitted), 2011

*Heintzenberg, J.*: The SAMUM-1 experiment over Southern Morocco: overview and introduction, *Tellus B*, 61, 2009

*Köhler, C.H. et al.*: Comparison of Ground Based Radiation Measurements in the Thermal IR during SAMUM-2 with Radiative Transfer Simulations, *Tellus B*, 63 (submitted), 2011

*Schmidt, K., Wauer, J., Rother, T., Trautmann T.*: Scattering database for spheroidal particles, *Applied Optics*, 48 (11), 2009

## **3.7 Radiative Transfer in a Diurnal Cycle of Inhomogeneous Shallow Cumulus**

*S. Gimeno García (TUM), V. Venema (University of Bonn), T. Trautmann*

To handle complexity to the smallest detail in radiative transfer (RT) models is in practice infeasible. Two main reasons prevent from this: (1) the optical properties of the atmosphere and Earth's surface are not available at an arbitrarily high resolution and (2) time-consuming accurate models for solving the RT in three-dimensional resolved media are prohibitive for some applications such as e.g. climate and numerical weather prediction (NWP) modeling as well as for operative remote sensing algorithms.

In addition to these restrictions there is, at least, another conceptual reason why simplified models are still widespread in use for atmospheric radiation applications: the search for a (mathematically) exact solution. There are only two cases where the radiative transfer equation has exact solutions: (1) considering a non-scattering medium and no reflection at the boundaries (or allowing reflection but decoupling the upwelling from the downwelling beam) and (2) allowing scattering but considering variability only in the vertical direction. The analyticity of these solutions, or combinations or slight modifications of them, is exploited in practically all operational remote sensing algorithms and climate and NWP models. Real clouds, however, are neither perfect black bodies, as they scatter radiation, nor horizontally homogeneous.

Three-dimensional radiation models can account for a greater complexity than one-dimensional ones, providing a more accurate solution of the radiative transfer at the cost of renouncing to the desirable exact mathematical solution and considerably increasing the calculation time. Continuous technology progress has led to an increase of computing power, therefore more sophisticated models can be used for radiative transfer computations. Additionally, three-dimensional models have been developed to study cloud variability and its multi-fractal nature. So, the actual situation offers a perfect scenario to test the adequacy of the one-dimensional (1D) radiative transfer theory and opens the possibility to explore alternatives.

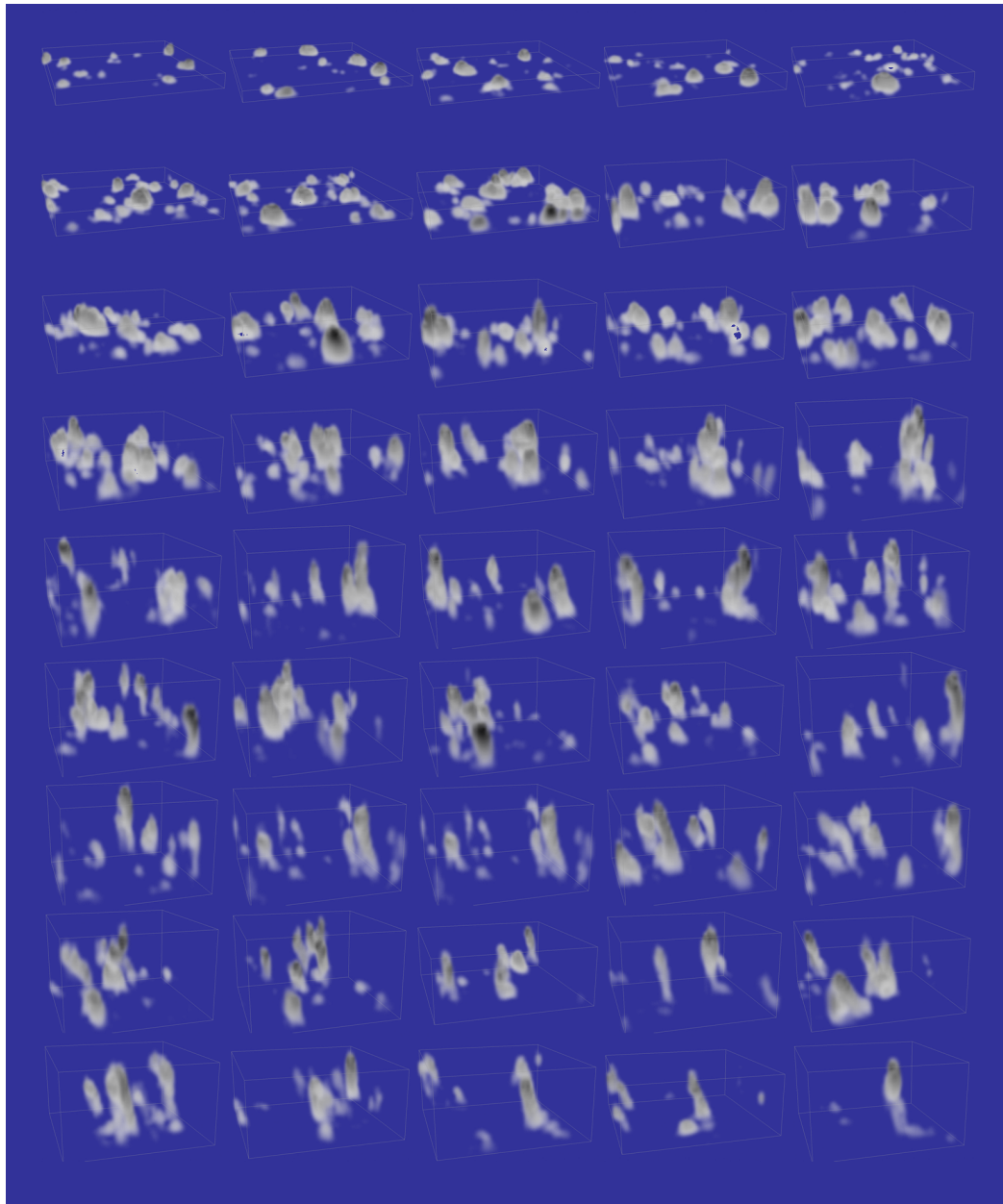


Fig. 3-16: Diurnal cycle of shallow cumulus clouds developing over land. Each of the 45 scenes shown here represents the cumulus evolution every 20 minutes. Dark grey colour represents high liquid water content (LWC), whereas light grey color represents low LWC. The spatial resolution is of 100 m (horizontally) and 40 m (vertically), respectively.

In our work, we aimed at examining the errors made when calculating one-dimensionally the solar radiation fluxes within coarse-resolved cloudy atmospheres instead of resolving cloud horizontal variability and using a three-dimensional (3D) RT model. In particular, we dealt with broadband solar fluxes in a diurnal cycle of a convective cumulus (see Fig. 3-16). The cloud microphysical properties were provided by a Large-Eddy Simulation (LES) model simulating the diurnal cycle of a shallow cumulus initialized with measurements taken on June 21<sup>st</sup>, 1997 at the SGP Central Facility, Ponca City, Oklahoma/USA (Latitude: 36° 36' 18.0" N, Longitude: 97° 29' 6.0" W; *Brown et al. 2002*). The LES

model delivered a cloudy scene every 20 min with a horizontal and vertical spatial resolution of 100 m and 40 m, respectively. For the dimensions of the atmospheric grid  $64 \times 64$  horizontal cells and 122 height levels were used (this study only comprised layers between 1160 m and 3040 m). The optical properties were calculated from the microphysical properties by means of the Slingo parameterization (Slingo 1989) and the angular distribution of cloud scattering events was described by the Henyey-Greenstein phase function. The solar position (zenith and azimuth) was exactly calculated as a function of time and geolocation. Finally the broadband molecular absorption was taken into account by means of the correlated k-distribution (CKD) method (Fu and Liou 1992). Molecular (Rayleigh) scattering was also considered, whereas the effect of aerosols was neglected. Lambertian reflection at the surface was considered with the broadband surface albedo equivalent to that of an agricultural region (Henderson-Sellers and Wilson 1983).

The RT simulations were performed using the Monte Carlo Radiative Transfer model (MoCaRT), which can provide both, the 3D 'exact' solution of the RT or an approximative one by employing a variety of 1D methods. The radiation simulations comprised the whole solar range. Only the troposphere and the lower stratosphere – top of the atmosphere at 30 km – were considered. On the one hand, we carried out fully three-dimensional (3D) calculations over the whole day using the fine resolved cumuli ( $100\text{m} \times 100\text{m} \times 40\text{m}$ ) and considered the results of these simulations as reference ('the truth'). On the other hand, we calculated the RT by means of the independent column approximation (ICA) using coarser clouds, representing the RT scheme in a cloud resolving model with coarser spatial resolution. In this case, the cumulus clouds were horizontally coarsened to  $16 \times 16$  pixels, i.e. the resolution was decreased four-fold down to ( $400 \text{ m} \times 400\text{m} \times 40\text{m}$ ).

Fig. 3-17 shows the results of the study. The left panel displays the reflected flux at the top of the atmosphere (TOA), the right top panel illustrates the transmitted flux at the Earth's surface and the right bottom panel shows the absorbed power through the whole atmosphere. Note that the absolute values of the fluxes depend on the incoming solar radiation which is a function of the cosine of the solar zenith angle (SZA), what is clearly seen in all three plots.

Two effects mainly contribute to the differences in the fluxes. Firstly, cloud variability is described at different resolutions, and secondly, horizontal photon transport is allowed in one case and forbidden in the other. The loss of variability leads to an overestimation of the reflected flux in case of the coarse resolved clouds due to Jensen's inequality (known in the literature as *albedo bias* or ICA-PPA – plane parallel approximation – bias). ICA simulations neglect the radiative 'cross-talk' between atmospheric columns (3D-ICA bias). This bias depends on the spatial distribution of cloud properties as well as on the illumination geometry.

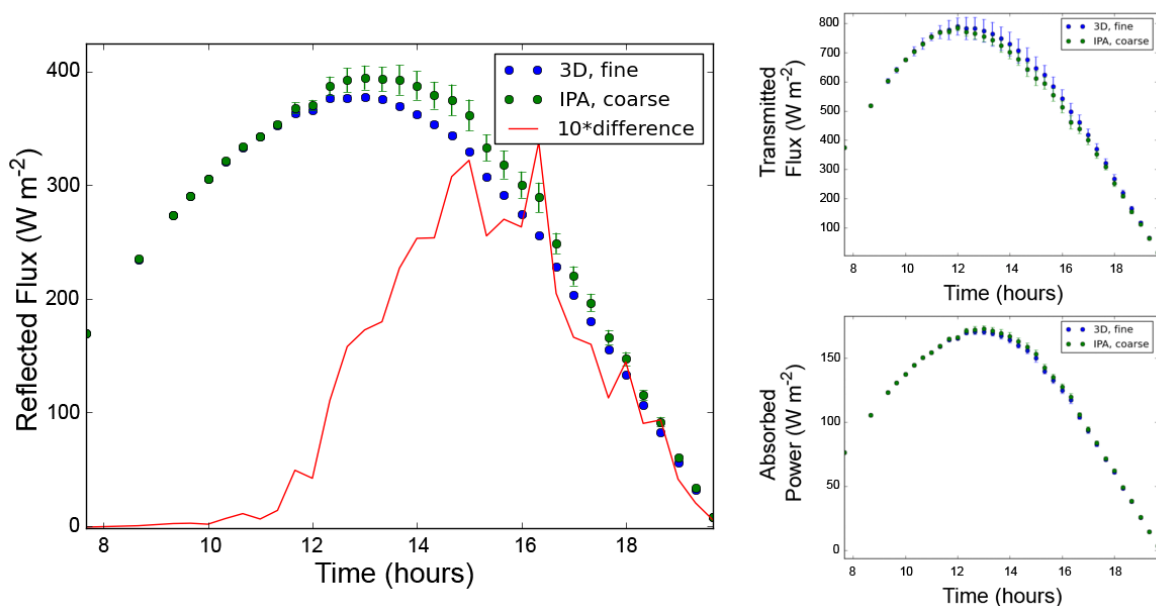


Fig. 3-17: Radiation fields in a diurnal cycle of shallow cumulus clouds developing over land (see Fig. 3-16). For further details see text.

In our study, the 'IPA-coarse' (green spots) reflected fluxes are larger than their '3D-fine' counterparts (blue spots) over the whole day with maxima as large as  $30 \text{ Wm}^{-2}$ . The standard deviation of the mean is shown as error bars: the larger the error bars, the higher the dispersion of the values. As a consequence of horizontal transport, 3D-fine reflected fluxes at TOA are smoother than the IPA-coarse ones. In case of transmitted fluxes at the ground, 3D-fine fields still show large variability, since the cloud layers are close to the surface.

In summary, in highly inhomogeneous cloudy atmospheres, the radiative transfer strongly depends on the horizontal scale at which the microphysical properties of the cloud fields are defined. Neglecting the subscale variability introduces large biases in the radiation fields. For radiation fluxes integrated over the whole solar range, these biases can reach a magnitude of tens of  $\text{Wm}^{-2}$  for reflection (albedo) and transmission, and few  $\text{Wm}^{-2}$  for absorption. RT biases introduced by the neglect of the subscale cloud variability have a large impact in numeric weather prediction and climate models.

### References

- Brown, A.R. et al.:* Large-eddy simulation of the diurnal cycle of shallow cumulus convection over land, *Q. J. R. Meteorol. Soc.*, 128 (582), 1075-1093, 2002
- Fu, Q., and Liou, K.N.:* On the correlated k-distribution method for radiative transfer in nonhomogeneous atmospheres, *J. Atmos. Sci.*, 49, 2139-2156, 1992
- Henderson-Sellers, A. and Wilson, M.F.:* Surface albedo data for climatic modeling, *Reviews of Geophysics*, 21 (8), 1983
- Slingo, A.:* A GCM Parameterization for the Shortwave Radiative Properties of Water Clouds, *J. Atmos. Sci.*, 46 (10), 1419-1427, 1989
- Gimeno García, S. and Trautmann, T.:* Radiative transfer modeling in inhomogeneous clouds by means of the Monte Carlo method. *Wissenschaftliche Mitteilungen aus dem Institut für Meteorologie der Universität Leipzig*, 30, Meteorological Institute of Leipzig University, Germany, ISBN 3-9808822-0-9, 2003

### 3.8 Reciprocity in Light Scattering Computations

K. Schmidt, M. Kahnert (SMHI), T. Rother

In the past a variety of different methods have been developed to describe the scattering of electromagnetic waves on single nonspherical particles. In general, they differ in the approach used, and, consequently, in their capabilities to compute the scattering behaviour of various particle classes. Corresponding computer programs are sophisticated, tested, and partly publicly available. However, they may lead to slightly different numerical results for a given scattering problem. This can also be the case for various implementations of the same approach or even for different versions of the same program. Such differences may become larger and larger when approaching the limits of the algorithms. On the other hand there are cases where only one single method exists for treating special scatterer types, i.e. no comparative calculations with alternative methods are possible for verifying the results obtained. In all these cases it is up to the user to finally judge the accuracy and correctness of the findings.

Fulfilling the reciprocity criterion represents a useful way to come to a final conclusion. *Reciprocity* means that the source and the observation point can be interchanged without changing the result. It requires no detailed knowledge of the method or the specific implementation. In addition it can also be used as a self-consistent and sensitive test when developing own algorithms. Examples for how to apply the reciprocity criterion are given below.

Table 3-6 summarizes the scatterer geometries and parameters considered in the investigations. Here,  $x$ ,  $a/b$  and  $n$  are the volume equivalent size parameter, the aspect ratio, and the complex refractive index, respectively. To check the reciprocity, two different configurations, proposed by *Rother and Wauer (2010)*, were used: Eulerian angles ( $\alpha=0^\circ$ ,  $\beta=0^\circ$ ,  $\gamma=0^\circ$ ) with a scattering angle  $\theta=90^\circ$  and Eulerian angles ( $\alpha=0^\circ$ ,  $\beta=90^\circ$ ,  $\gamma=0^\circ$ ) with a scattering angle  $\theta=270^\circ$ . Table 3-7 illustrates the results for the polarized differential scattering cross sections  $d\sigma_{pq}/d\Omega$  with the polarization (p,q) obtained by means of the programs *mieschka* (version 1.0.1\_1; see *Wauer et al. 2004*) and *DDSCAT* (*Draine and Flatau 1994*). Fulfilment of the reciprocity means that  $d\sigma_{hh}/d\Omega$  and  $d\sigma_{ww}/d\Omega$  are equal in both configurations. As obvious, at larger size parameters *DDSCAT* reveals problems. The largest discrepancy exists for  $d\sigma_{hh}/d\Omega$  at the scatterer *sphd\_o\_15*. Fig. 3-18 provides a comparison of the whole scattering behaviour between *mieschka* and *DDSCAT* for this case. Significant differences occur in the range  $60^\circ$ - $120^\circ$ , consequently in  $240^\circ$ - $300^\circ$ , and in the backscattering region around  $180^\circ$  which is crucial in LIDAR applications. The fulfilment of the reciprocity by *DDSCAT* is therefore only expected outside these critical regions under the assumption that *mieschka* produces correct results.

Scatterer		Parameters
Abbreviation	Form	
sphd_p_3	prolate spheroid	$x = 3, a/b = 1.5, n = (1.6, 0.0005)$
sphd_p_15	prolate spheroid	$x = 15, a/b = 1.5, n = (1.6, 0.0005)$
sphd_o_3	oblate spheroid	$x = 3, a/b = 0.67, n = (1.6, 0.0005)$
sphd_o_15	oblate spheroid	$x = 15, a/b = 0.67, n = (1.6, 0.0005)$

Table 3-6: Scatterer geometries and parameters considered in the investigations.

Scatterer	$d\sigma_{hh}/d\Omega$ $\beta=0^\circ$ $\theta=90^\circ$	$d\sigma_{hh}/d\Omega$ $\beta=90^\circ$ $\theta=270^\circ$	$d\sigma_{vv}/d\Omega$ $\beta=0^\circ$ $\theta=90^\circ$	$d\sigma_{vv}/d\Omega$ $\beta=90^\circ$ $\theta=270^\circ$	Program
sphd_p_3	2.214 2.178	2.225 2.170	1.330 1.344	1.332 1.346	mieschka DDSCAT
sphd_p_15	6.485 6.465	6.485 8.443	6.883E-1 7.757E-1	6.944E-1 4.050E-1	mieschka DDSCAT
sphd_o_3	1.334 1.314	1.334 1.312	1.250 1.259	1.246 1.255	mieschka DDSCAT
sphd_o_15	1.078E+1 2.818	1.078E+1 1.081E+1	1.925E+1 1.933E+1	1.925E+1 1.919E+1	mieschka DDSCAT

Table 3-7: Polarized differential scattering cross sections for the different particles obtained by means of the programs mieschka and DDSCAT.

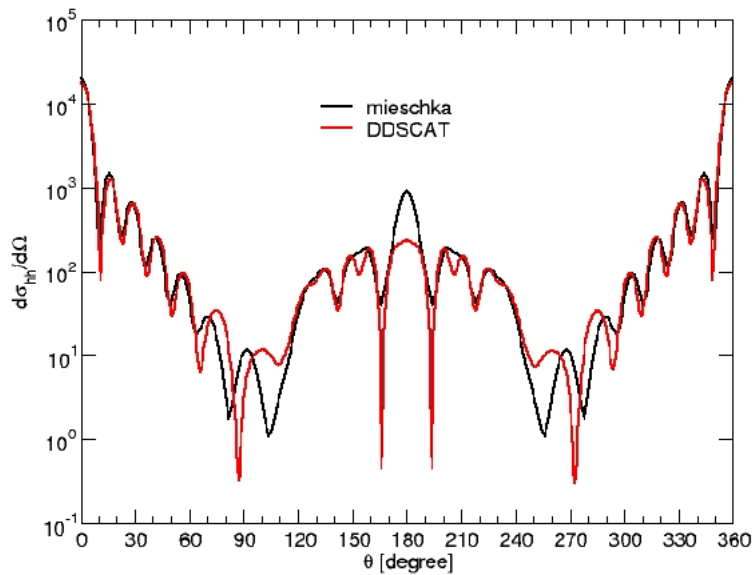


Fig. 3-18: hh-polarized differential scattering cross section for the scatterer *sphd\_o\_15* in the orientation ( $\alpha=0^\circ$ ,  $\beta=0^\circ$ ,  $\gamma=0^\circ$ ) obtained by means of the programs mieschka and DDSCAT.

### References

Draine, B.T. and Flatau, P.J.: Discrete-dipole approximation for scattering calculations, J. Opt. Soc. Am., A 11, 1491-1499, 1994

Rother, T. and Wauer, J.: Case study about the accuracy behavior of three different T-matrix methods, Appl. Opt. 49, 5746-5756, 2010

Wauer, J., Schmidt, K., Rother, T., Ernst, T. and Hess, M.: Two software tools for the plane-wave scattering on nonspherical particles in the German Aerospace Center's virtual laboratory, Appl. Opt., 43 6371-6379, 2004

### 3.9 Constrained Inversion Methods and Retrieval of O<sub>3</sub> Profiles from UV/VIS Nadir Instruments

*O. Schüssler (TUM), A. Doicu, D. Loyola*

A class of methods for the retrieval of ozone profiles from UV/VIS nadir sounding instruments, such as GOME/ERS-2, GOME-2/MetOp, SCIAMACHY/ENVISAT and OMI/AURA has been designed. We incorporated an additional constraint into the classical regularization methods in order to make them less sensitive to the choice of the regularization parameter. In classical regularization, when the regularization parameter value is too small, the retrieved profile has significant deviations from the *a priori* profile and in the opposite case, when it is too large, the retrieved profile is too close to the *a priori* profile. For the designed constrained inversion methods we imposed the additional constraint on the integrated ozone profile, which can be accurately computed by an independent algorithm like DOAS or GODFIT. Thus the magnitude of the profile through the vertical column can be controlled reducing the sensitivity of the regularization methods with respect to the choice of the regularization parameter.

#### Constrained Tikhonov Regularization

In the framework of Tikhonov regularization, the solution of the inverse problem  $\mathbf{y}^\delta = F(\mathbf{x})$  is computed as the minimizer of the objective function

$$\mathcal{F}(\mathbf{x}) = \|\mathbf{y}^\delta - F(\mathbf{x})\|^2 + \alpha \|\mathbf{L}(\mathbf{x} - \mathbf{x}_a)\|^2$$

where  $\mathbf{y}^\delta$  is the noisy data vector,  $\mathbf{x}$  is the state vector,  $\mathbf{x}_a$  is the *a priori* state vector,  $\mathbf{L}$  corresponds to the regularization matrix and  $\alpha$  is the regularization parameter.

The solution of a nonlinear ill-posed problem via Tikhonov regularization is equivalent to the solution of a sequence of ill-posed linearizations of the forward model about the current iterate. At the iteration step  $k$ , we consider the linearized problem  $\mathbf{K}_{k\alpha}(\mathbf{x} - \mathbf{x}_a) = \mathbf{y}_k^\delta$  with  $\mathbf{y}_k^\delta = \mathbf{y}^\delta - F(\mathbf{x}_{k\alpha}^\delta) + \mathbf{K}_{k\alpha}(\mathbf{x}_{k\alpha} - \mathbf{x}_a)$ .

The linearized problem is ill-posed as well, and in this regard, we solve the linear equation with Tikhonov regularization, i.e.

$$F_k(\mathbf{x}) = \|\mathbf{y}_k^\delta - \mathbf{K}_{k\alpha}(\mathbf{x} - \mathbf{x}_a)\|^2 + \alpha \|\mathbf{L}(\mathbf{x} - \mathbf{x}_a)\|^2$$

Expressing  $F$  in terms of  $\Delta\mathbf{x} = \mathbf{x} - \mathbf{x}_a$ , we get

$$F_k(\Delta\mathbf{x}) = \Delta\mathbf{x}^T (\mathbf{K}_{k\alpha}^T \mathbf{K}_{k\alpha} + \alpha \mathbf{L}^T \mathbf{L}) \Delta\mathbf{x} - 2 \mathbf{y}_k^{\delta T} \mathbf{K}_{k\alpha} \Delta\mathbf{x} + \mathbf{y}_k^{\delta T} \mathbf{y}_k^\delta.$$

The new iterate is computed from  $\Delta\mathbf{x}_{k+1\alpha}^\delta = \mathbf{x}_{k+1\alpha}^\delta - \mathbf{x}_a$  where the minimizer  $\Delta\mathbf{x}_{k+1\alpha}^\delta$  is given by  $\Delta\mathbf{x}_{k+1\alpha}^\delta = -\mathbf{G}^{-1} \mathbf{g}$  with  $\mathbf{G} = \mathbf{K}_{k\alpha}^T \mathbf{K}_{k\alpha} + \alpha \mathbf{L}^T \mathbf{L}$  and  $\mathbf{g} = -\mathbf{K}_{k\alpha}^T \mathbf{y}_k^\delta$ .

#### Equality Constrained Tikhonov Regularization

At the iteration step  $k$ , we compute the profile deviation  $\Delta\mathbf{x}_{k+1\alpha}^\delta$  by solving the constrained quadratic problem

$$\begin{aligned} \text{minimize } Q(\Delta\mathbf{x}) &= \mathbf{g}^T \Delta\mathbf{x} + \frac{1}{2} \Delta\mathbf{x}^T \mathbf{G} \Delta\mathbf{x} \\ \text{subject to } \sum_{i=1}^n \Delta\mathbf{x}_i &= \mathbf{c} \end{aligned}$$

where  $c$  is the difference between the vertical columns of the *exact* state vector and the *a-priori*. The null-space or range-space methods can be used to solve this constrained programming problem (Gill et al. 2004).

Inequality constrained Tikhonov Regularization

At the iteration step  $k$ , we compute the profile deviation  $\Delta \mathbf{x}_{k+1\alpha}^\delta$  solving the following constrained quadratic problem

$$\begin{aligned} & \text{minimize } Q(\Delta \mathbf{x}) = \mathbf{g}^T \Delta \mathbf{x} + \frac{1}{2} \Delta \mathbf{x}^T \mathbf{G} \Delta \mathbf{x} \\ & \text{subject to } \sum_{i=1}^n \Delta x_i \leq c_{max} \quad \wedge \quad \sum_{i=1}^n \Delta x_i \geq c_{min} \end{aligned}$$

The quadratic problem with inequality constraint is solved with primal and dual active sets methods (Goldfarb and Idnani 1983).

Constrained Iteratively Regularized Gauss-Newton (IRGN) Method

The iteratively regularized Gauss-Newton method can be regarded as a modified version of Tikhonov regularization with a variable regularization parameter, which can be chosen in advance as the terms of a geometric sequence. The iterative process is stopped according to the discrepancy principle. As in the case of Tikhonov regularization, the constrained versions of the IRGN method assume the replacement of the unconstrained minimization step by a quadratic problem involving equality or inequality constraints.

Simulations and Results

The relative errors of the constrained regularization methods, of the Tikhonov regularization and of the Gauss-Newton method are shown in the Fig. 3-19. The constrained methods are more stable than their unconstrained versions, especially with respect to underestimation of the regularization parameter.

Table 3-8 lists the computing times for all of the mentioned methods. It is obvious that the computing time of the equality-constrained Tikhonov regularization resembles that of the ordinary method.

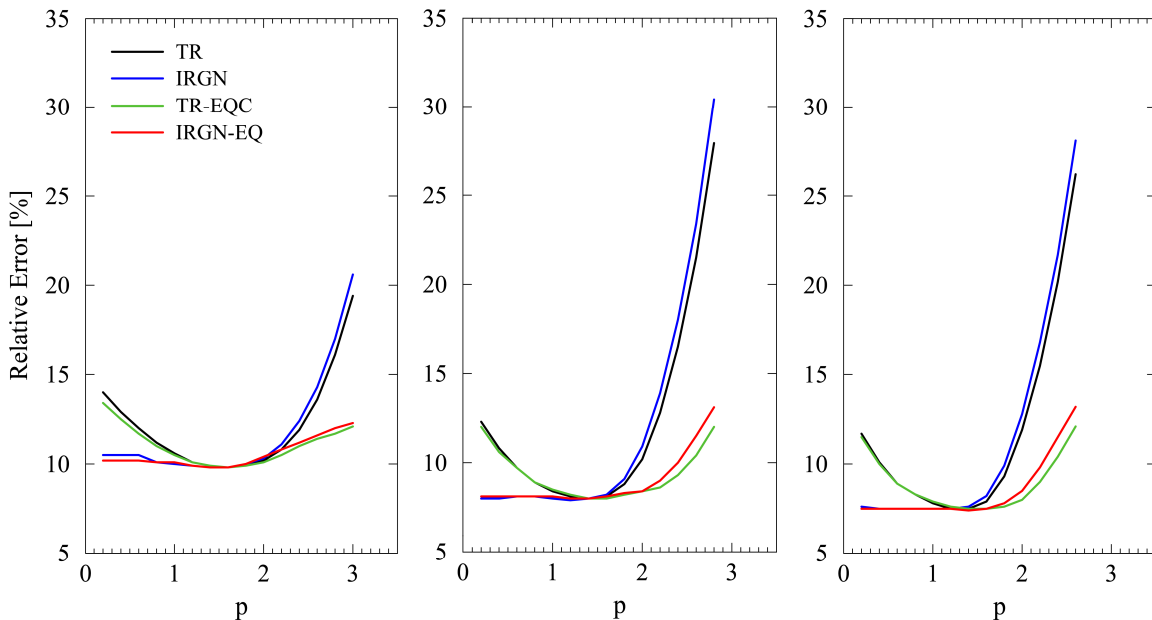


Fig. 3-19: Relative errors of the Tikhonov regularization (TR), the iteratively regularized Gauss-Newton method (IRGN) and their equality-constrained versions (TR-EQC and IRGN-EQC, respectively). The regularization parameter is  $\alpha = \sigma^p$ , where  $\sigma$  is the noise standard deviation.

p	TR	TR-EQC	IRGN	IRGN-EQC	IRGN-INEQC
2.4	0:20 (4; 16.5)	0:21 (4; 9.2)	0:23 (5; 18.0)	0:26 (5; 9.8)	12:28 (5; 9.9)
0.2	0:20 (4; 12.3)	0:21 (4; 12.9)	0:39 (12; 8.1)	0:50 (12; 8.1)	12:28 (12; 8.3)

Table 3-8: Computing time in the format minutes:seconds for Tikhonov regularization (TR) and its constrained versions and for iteratively regularized Gauss-Newton method (IRGN) and its constrained versions, respectively. The numbers in parentheses represent the number of iterations and the relative error in percent.

### References

Gill, P.E., Murray, W., Wright, M.H.: Practical Optimization, London: Elsevier Academic Press, 2004

Goldfarb, D., Idnani, A.: A numerically stable dual method for solving strictly convex quadratic programs, *Mathematical Programming*, 27, 1-33, 1983

## 3.10 Optimized Rational Approximations for the Voigt and Complex Error Function

F. Schreier

The Voigt function, defined as convolution of a Lorentz and a Gaussian function, is important in many branches of physics, e.g. atomic and molecular spectroscopy, atmospheric radiative transfer, plasma physics, astrophysics. The Voigt function is identical to the real part of the complex error function

$$w(z) = K(x, y) + iL(x, y) = \frac{i}{\pi} \int_{-\infty}^{\infty} \frac{e^{-t^2}}{z - t} dt \quad z = x + iy$$

The integrals defining the Voigt and complex error function cannot be evaluated in closed analytical form and have to be computed numerically. Unfortunately this is especially difficult for small  $y$ , and the majority of algorithms developed in the past divide the  $x,y$  plane into several regions and utilize appropriate methods, e.g., a series approximation for small  $x,y$  and an asymptotic approximation for large  $x,y$ . However, even though the algorithms developed for the individual  $x,y$  regions may be highly optimized, the overall efficiency of such codes largely depends on the efficiency of arithmetic operations as well as the efficiency of executing conditional code. Even worse, if only a few function evaluations are typically required in a certain  $x,y$  subdomain, then any code optimization will be irrelevant for the total computing time.

Rational approximations have been proven to be an efficient approach for a wide variety of functions, and have been used also for the complex error function. e.g., Hui *et al.* (1978), Humlicek (1979, 1982), and Weideman (1994). An attractive and unique feature of the Hui-Armstrong-Wray and Weideman algorithms is their applicability in the entire domain. Unfortunately, the Hui-Armstrong-Wray approximation has serious accuracy problems for small  $y$ , and the Weideman approach is computationally more expensive than the others. On the other hand, the widely used Humlicek algorithm uses four different approximations for small  $y$ . In order to minimize the number of conditional branches one can combine Humlicek's rational approximation for large  $|x|+y$  with Weideman's approximation for small arguments,

$$w(z) = \frac{iz / \sqrt{\pi}}{z^2 - \frac{1}{2}} \quad \text{for } |x| + y < 15$$

$$w(z) = \frac{\pi^{-1/2}}{L - iz} + \frac{2}{(L - iz)^2} \sum_{n=0}^{N-1} a_{n+1} Z^n, \quad Z = \frac{L + iz}{L - iz}, \quad L = 2^{-1/4} N^{1/2} \quad \text{for } |x| + y \geq 15$$

Fig. 3-20 shows the relative accuracy  $|\Delta K / K_{ref}|$  of this approximation, indicating maximum deviations of less than  $2 \times 10^{-3}$  and  $8 \times 10^{-5}$  for  $N=24$  and  $N=32$ , respectively.

For benchmark tests of this new code including some more versions of such rational approximations (implemented in Fortran and Python) molecular absorption cross sections for high resolution line-by-line atmospheric radiative transfer modelling in the microwave and infrared spectral range have been evaluated. They were similar to the tests described in section 3.14 of the 2007 Annual Report. Fig. 3-21 indicates that the Humlicek-Weideman combination is superior for both the Fortran and Python implementation. Because the line center region comprises only a few dozen grid points and gives the largest contribution to the total sum of Voigt lines, high accuracy of the approximation used for small  $|x|$  is significantly more important than computational speed. Furthermore, the tests demonstrate that programming language, compiler choice, and implementation details impact computational speed and there is no unique ranking of algorithms (for details and further comparisons see *Schreier 2011*).

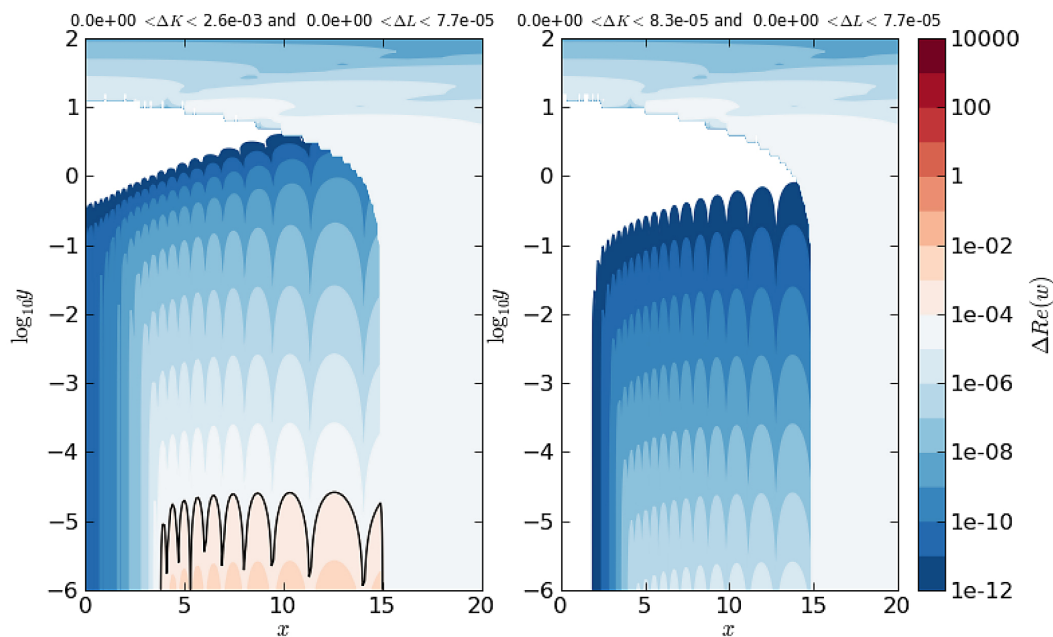


Fig. 3-20: Relative accuracy of Humlicek-Weideman approximation with  $N=24$  (left) and  $N=32$  (right). The Poppe-Wijers algorithm has been used as a reference (*Poppe and Wijers 1990*).

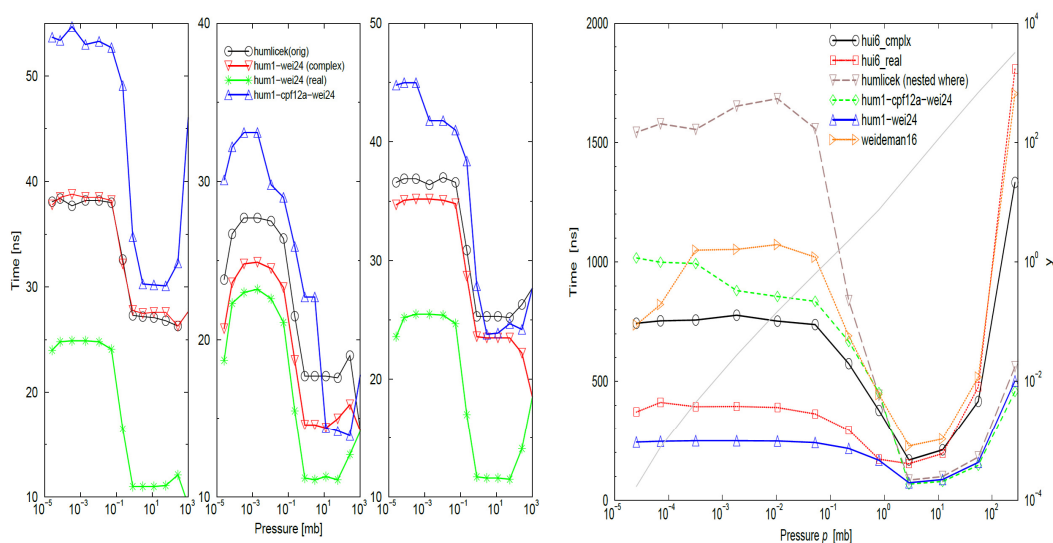


Fig. 3-21: Time (in  $10^{-9}$  sec) per function evaluation for various optimized implementations.  $\text{HNO}_3$  cross sections in the interval  $16-17 \text{ cm}^{-1}$  computed with (a) GNU gfortran compiler, (b) Intel ifc compiler, (c) NAG nagfor compiler, and (d) Python/Numeric Python interpreter.

### References:

Hui, A.K., Armstrong, B.H. and Wray, A.A.: Rapid computation of the Voigt and complex error functions. *J. Quant. Spectrosc. & Radiat. Transfer*, 19:509–516, doi: 10.1016/0022-4073(78)90019-5, 1978

Humlicek, J.: An efficient method for evaluation of the complex probability function: the Voigt function and its derivatives, *J. Quant. Spectrosc. & Radiat. Transfer*, 21:309-313, 1979

Humlicek, J.: Optimized computation of the Voigt and complex probability function, *J. Quant. Spectrosc. & Radiat. Transfer*, 27:437-444, 1982

Poppe, G.P.M., Wijers, C.M.J.: Algorithm 680 – evaluation of the complex error function, *ACM Trans Math Soft*, 16:47, 1990

Schreier, F.: Optimized implementations of rational approximations for the Voigt and complex error function, *J. Quant. Spectrosc. & Radiat. Transfer*, doi:10.1016/j.jqsrt.2010.12.010, 2011

Weideman, J.A.C.: Computation of the complex error function, *SIAM J. Num. Anal.*, 31:1497, 1994

### **3.11 Line-by-Line Tools for Absorption Optical Depths**

*F. Schreier, C. Emde (LMU), B. Mayer (LMU)*

Radiative transfer modelling plays a key role for remote sensing because it is central for the development and testing of inversion algorithms as well as for the design of new remote sensing instruments. Remote sensing of planetary atmospheres and surfaces uses radiation covering a wide range of wavelengths, coming either from the Sun or from the atmosphere (passive remote sensing), or from an artificial radiation source (active remote sensing). Radiation is affected by its interaction with the atmosphere or the surface – the observed radiation therefore contains information about the atmosphere and surface which can be retrieved.

The aim of the ESAS-Light (Earth-Surface-Atmosphere-System-Light) study, funded by ESA-ESTEC and performed by the partners LMU, DLR-IPA, Arve Kylling/Norway and DLR-IMF, was to develop a flexible radiative transfer toolbox for the Earth atmosphere-surface system in the solar and thermal spectral ranges (<http://esaslight.libradtran.org/internal/Wiki/doku.php>). The toolbox shall strengthen ESA's modelling capabilities for internal purposes (instrument and prototyping of inversion algorithms) and provide a set of standard radiative transfer tools for the development of ESA commissioned inversion schemes and calibration/validation activities.

The libRadtran software package (Mayer and Kylling 2005, [www.libradtran.org](http://www.libradtran.org)), a suite of tools for radiative transfer calculations mainly for but not restricted to the Earth's atmosphere, was selected as an ideal starting point for the ESAS-Light study. In order to perform high spectral resolution calculations using radiative transfer solvers such as libRadtran, pre-calculated (layer) optical depths of molecular absorption are required. A user friendly line-by-line tool which generates these input (data) as required for libRadtran has been provided by IMF-AP. Based on atmospheric input parameters (pressure, temperature, and trace gas concentrations) and on spectroscopic data (line parameter databases such as HITRAN or GEISA), molecular absorption optical thicknesses were computed. The 'lbl2od' tools are based on 'Py4CAtS', a Python re-implementation of the Fortran infrared radiative transfer code MIRART/GARLIC (Schreier and Schimpf 2001). Clearly a pure Python implementation would be by far too slow for a computational challenging task such as line-by-line modelling, so Py4CAtS makes heavy use of the Numeric Python extensions. The code utilizes efficient and accurate numerical methods for the computation of absorption cross sections, n.b. a 'multigrid' technique to cope with the large number of spectral points (Schreier 2006) and an optimized version (Schreier and Kohlert 2008) of the rational approximation for the Voigt function (Hui et al. 1978).

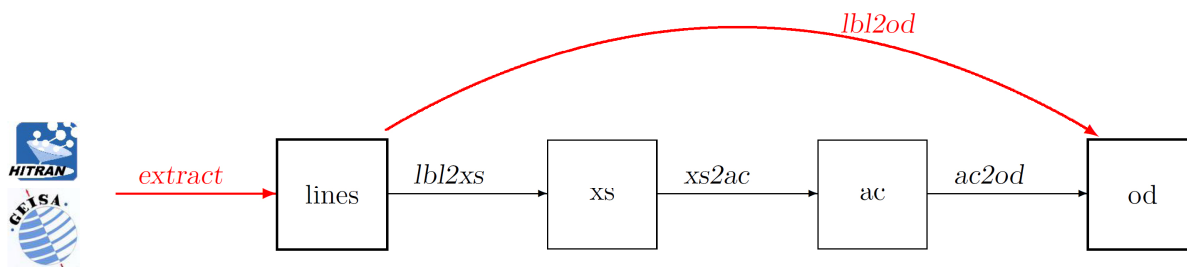


Fig. 3-22: From HITRAN/GEISA via cross sections and absorption coefficients to optical depths.

In Py4CATS the individual steps of an infrared radiative transfer computation are implemented in separate scripts, see Fig. 3-22 which consists of the steps:

- `extract`: (select) lines of relevant molecules in the spectral range of interest
- `lbl2xs`: compute line-by-line cross sections for given pressure(s) and temperature(s)
- `xs2ac`: multiply cross sections with number densities and sum over all molecules
- `ac2od`: integrate absorption coefficients along the line-of-sight through atmosphere

```

mkdir example
cd example
extract -x 50,60 /data/hitran/2008/lines
lbl2xs H20.vSEan 03.vSEan 0H.vSEan
xs2ac H20.xs 03.xs 0H.xs
ac2od H20+03+0H.ac
lbl2od H20.vSEan 03.vSEan 0H.vSEan
  
```

For each molecule  $m$  and  $p, T$  level  $j$ :

$$k^{(m)}(\nu, p_j, T_j) = \sum_l S_l g(\nu, \hat{\nu}_l, \gamma_l)$$

$$\alpha_j(\nu) = \sum_m k^{(m)}(\nu, p_j, T_j) n_m(z_j)$$

$$\tau_j(\nu) = \int_{z_j}^{z_{j+1}} \alpha_j(\nu) dz$$

Fig. 3-23: Typical workflow for line-by-line modelling with Py4CATS: HITRAN/GEISA → line parameter extracts → cross sections → absorption coefficients → optical depth for the spectral range 50–60  $\text{cm}^{-1}$ . Note that on the left hand side the output files are not indicated (usually done with the 'o'-option). Furthermore specification of the atmospheric data is not shown.

All these scripts read their input from external files, and save their results on files, too (see the workflow indicated in Fig. 3-23). As a consequence, I/O operations can become quite time consuming since the number of spectral grid points can become quite big. Furthermore a large part of the scripts was devoted to check the consistency of the various input files, e.g. the `xs2ac` script had to test that the different cross section files cover the same – or at least a common subset – spectral range for the same altitude range. On the other hand, circumventing/bypassing some of the intermediate files is straightforward, especially when being mainly interested in the final optical depth, see Fig. 3-24 consisting of the step:

- `lbl2od`: compute line-by-line cross sections, combine to absorption coefficients and integrate through the atmosphere.

```

mkdir example
cd example
extract -x 50,60 /data/hitran/2008/lines
lbl2od -o H20+03+0H.od atmos.data \
      H20.vSEan 03.vSEan 0H.vSEan
  
```

For each molecule  $m$  and  $p, T$  level  $j$ :

$$k^{(m)}(\nu, p_j, T_j) = \sum_l S_l g(\nu, \hat{\nu}_l, \gamma_l)$$

$$\alpha_j(\nu) = \sum_m k^{(m)}(\nu, p_j, T_j) n_m(z_j)$$

$$\tau_j(\nu) = \int_{z_j}^{z_{j+1}} \alpha_j(\nu) dz$$

Fig. 3-24: Typical workflow: From HITRAN/GEISA line parameter extract directly to optical depths.

## References

Hui, A.K., Armstrong, B.H. and Wray, A.A.: Rapid computation of the Voigt and complex error functions. *J. Quant. Spectrosc. & Radiat. Transfer*, 19:509–516, doi: 10.1016/0022-4073(78)90019-5, 1978

Mayer, B. and Kylling, A.: Technical note: The libradtran software package for radiative transfer calculations – description and examples of use, *Atm. Chem. Phys.*, 5(7):1855-1877, doi: 10.5194/acp-5-1855-2005, 2005

Schreier, F. and Schimpf, B.: A new efficient line-by-line code for high resolution atmospheric radiation computations incl. derivatives, In W.L. Smith and Y. Timofeyev, editors, *IRS 2000: Current Problems in Atmospheric Radiation*, 381–384. A. Deepak Publishing, 2001

Schreier, F.: Optimized evaluation of a large sum of functions using a three-grid approach, *Comp. Phys. Comm.*, 174:783-802, doi: 10.1016/j.cpc.2005.12.015, 2006

Schreier, F. and Kohlert, D.: Optimized implementations of rational approximations – a case study on the Voigt and complex error function, *Comp. Phys. Comm.*, 179(7):457-465, doi: 10.1016/j.cpc.2008.04.012, 2008

### **3.12 Line-by-Line Computation of Atmospheric IR Spectra with Field Programmable Gate Arrays**

*F. Schreier and D. Kohlert (University of Applied Sciences, Regensburg)*

Radiative transfer modelling of high resolution infrared (or microwave) spectra still represents a major challenge for the processing of atmospheric remote sensing data. Computational capabilities such as speed and memory have significantly grown in the past decades, but concurrently these advances have been compensated by a similar growth in data amount and quality: MIPAS aboard ESA's ENVISAT platform measures about 17 000 spectra per day since its launch in March 2002, whereas PREMIER's limb IR imager proposed for one of the future ESA Earth Explorer missions will provide about 15 000 000 radiance spectra per day.

The computation of thousands of Voigt profiles for several molecules and some dozen atmospheric levels on up to a million of spectral points presents the greatest challenge for line-by-line radiative transfer models. Recent work on optimization of Voigt function algorithms (see chapter 3.10) has shown that some ten  $10^{-9}$  seconds per function evaluation appear to be the best what can be performed with current commodity CPU's. In the past decade, novel architectures such as Graphics Processing Units (GPU) or Field Programmable Gate Arrays (FPGA) have gained increasing attraction as an alternative to conventional CPU's (*Kindratenko 2009*). Recently, we have achieved the first Field Programmable Gate Array (FPGA) implementation of line-by-line molecular absorption computations.

#### FPGA Coprocessor Architecture

The time critical computation of the value of the Voigt function  $K(x_i, y_l)$  for every grid point  $i$  (essentially frequency) and every line  $l$  and the summation of all Voigt profiles making up the cross section is implemented in hardware. For the evaluation of the Voigt function, a highly optimized implementation of the rational approximation (*Hui et al. 1978*) is utilized (*Schreier and Kohlert 2008*), and accordingly, in a 'pre-processing' step, the computation of the coefficients of the nominator and denominator polynomial of  $K(x, y)$  is implemented in hardware, too.

The hardware is realized on a Virtex-4-FPGA (XC4VLX25-10FFG668C) by XILINX Technologies Inc. The FPGA is located on a plug-in card, produced by CESYS GmbH, Germany, with PCI-Express interface (chip made by PLX Technology Inc.). Fig. 3-25 shows an overview of the FPGA-board and its connection to the host-computer. The communication via the PCI-Express interface is handled by the PLX-device. Software drivers are provided by PLX, as well as an application programming interface.

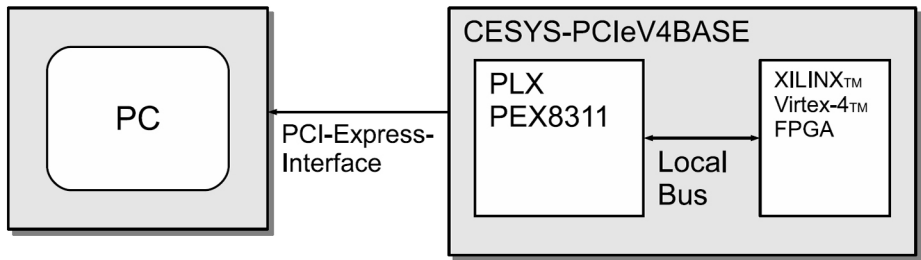


Fig. 3-25: Connection FPGA to host computer.

Fig. 3-26 illustrates the concept of the overall structure of the FPGA-design. It is strictly synchronous, all elements are clocked by the 66 MHz system clock. The local bus interface connects the computing hardware to the PLX local bus. Two RAM blocks are used for input and output data. The block called 'coefficient RAM' stores the input data (line parameters, the number of grid points and lines, and the polynomial coefficients). 959 lines, each represented by four 44 bit words, can be stored and calculated without additional I/O. The block 'XS RAM' stores the values of the cross section  $xs[i]$  for every grid point  $i$ . It also serves as an accumulator, where the values for each line are added to the values of the previous lines. Altogether,  $959 \times 16384 = 15.7 \times 10^6$  single Voigt and cross section calculations can be done after loading one set of 959 line data.

Furthermore, there are two computing units: The ' $\rho/\tau$ -engine' computes the coefficients of the nominator and denominator polynomial approximating the Voigt function. The XS-engine calculates the contribution of the current line to the cross section  $xs[i]$ , while the accumulator logic block reads the old value of  $xs[i]$ , adds it to the new value and stores the result in the same memory location. The optimal realization would be two parallel pipelines for denominator and nominator supplying the divider and the subsequent units with a new operand per clock cycle. This would deliver one result for a grid point in every clock cycle, but requires 16 floating point multipliers, 16 floating point adders and 1 floating point divider. However, due to hardware restrictions, only one multiplexed pipeline for nominator and denominator requiring two clock cycles had to be used.

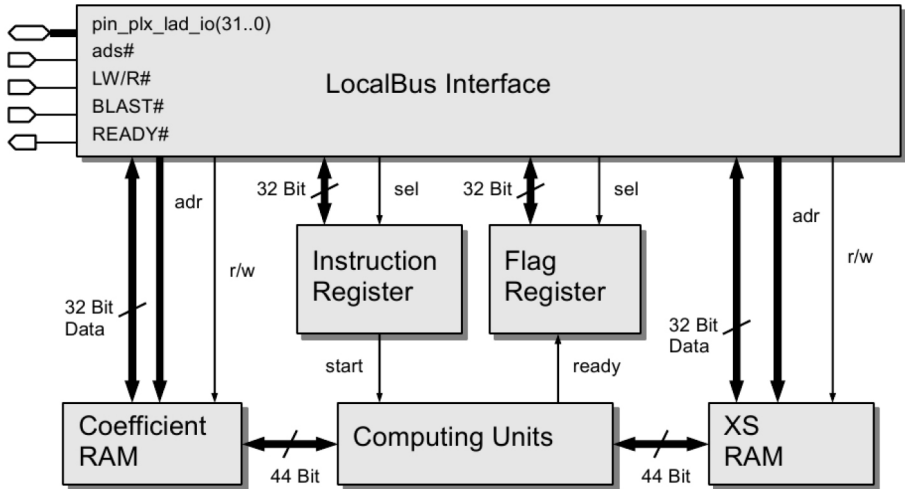


Fig. 3-26: Overview of the implemented hardware.

### Performance Tests

The performance of the FPGA coprocessor was compared to the performance of a conventional C program running on a *state-of-the-art* Dell Optiplex computer. The measured computation time of the hardware co-processor was 0.453 seconds for 950 lines and 16 000 spectral points, corresponding to about 30 ns per line and grid point. On the other hand, the pure software solution required 0.297 seconds, i.e. the (optimized) software implementation is slightly faster than the current hardware implementation. This better performance of the software solution can be explained by the much higher clock frequencies of the Intel processor (2.4 GHz), whereas the FPGA-coprocessor currently uses a 66 Mhz clock. Moreover, the VIRTEX4-FPGA generation does not use the latest semiconductor technologies, and due to size restrictions the nominator and denominator polynomials had to be calculated sequentially ('multiplexing').

### Outlook

Recently we started to use an FPGA board with a VIRTEX 6 XC6VLX240T device. This FPGA includes 768 25 ×18 multiplier/accumulators and 241152 logic cells compared to 24192 logic cells of the currently used FPGA device. With the new FPGA device it is possible to implement 12 parallel XS engines on the chip with no nominator/denominator multiplexing necessary. Furthermore, doubling the clock frequency is also possible, i.e. a performance increase of a factor of 48 is realistic. Thus, execution times well below 1 ns per Voigt line and spectral grid point will soon be possible (for details see *Kohlert and Schreier 2011*).

### References

*Hui, A.K., Armstrong, B.H. and Wray, A.A.*: Rapid computation of the Voigt and complex error functions. *J. Quant. Spectrosc. & Radiat. Transfer*, 19:509–516, doi: 10.1016/0022-4073(78)90019-5, 1978

*Kindratenko, V.*: Novel computing architectures, *Computing in Science & Eng.*, 11(3):54-57, doi: 10.1109/MCSE.2009.56, 2009

*Kohlert, D. and Schreier, F.*: Line-by-line computation of atmospheric infrared spectra with field programmable gate arrays, *IEEE Journal of Selected Topics in Earth Observations and Remote Sensing*, doi: 10.1109/JSTARS.2010.2098395. (in press), 2011

*Schreier, F. and Kohlert, D.*: Optimized implementations of rational approximations – a case study on the Voigt and complex error function, *Comp. Phys. Comm.*, 179(7):457-465, doi: 10.1016/j.cpc.2008.04.012, 2008

## **3.13 First Results of Inversion for Infrared/Microwave Limb Sounding**

*J. Xu, F. Schreier, A. Doicu, T. Trautmann, P. Vogt (IMF-EV)*

In order to measure emission from space in the infrared (IR) and microwave (MW) spectral range for mapping atmospheric species, several new generation instruments for remote sensing of the atmosphere have recently been developed. This leads to an increased interest in high resolution radiative transfer modelling and advanced inversion strategies.

The German Aerospace Center (DLR) developed a new balloon-borne heterodyne limb sounder, TELIS (Terahertz and submillimeter Limb Sounder) in cooperation with the Netherlands Institute for Space (SRON), and the Rutherford Appleton Laboratory (RAL) in the United Kingdom. After two successfully completed flights during 2009 and 2010, the next flight is scheduled for early 2011. Together with the MIPAS-B instrument TELIS is acting as a test-case for space-borne missions, e.g. SMILES, focusing on submillimeter (sub-mm) / far infrared (FIR) limb emission measurements. SMILES (Superconducting submillimeter-wave limb-emission sounder) has been launched in September 2009 aiming at monitoring global distributions of stratospheric trace gases.

The new code PILS (Profile Inversion for Limb Sounding) has been developed for solving the nonlinear inverse problems arising in the analysis of atmospheric measurements by limb sounders. PILS can be regarded as one of the descendants of GARLIC (see previous IMF-AP annual reports) as PILS's forward model (radiative transfer simulation) is based on the GARLIC line-by-line code. This model emphasizes

efficient and reliable algorithms and techniques for the computation of radiance and transmission, the Jacobian matrix calculation, and constrained nonlinear least squares optimization.

In order to ascertain the atmospheric profile, we have to solve a minimization problem,

$$\min_{\vec{x}} \left\| \vec{F}(\vec{x}) - \vec{y} \right\|^2$$

leading to an iterative solution

$$\delta \vec{x} = \left[ \mathbf{A}(\vec{x}_0)^T \mathbf{A}(\vec{x}_0) \right]^{-1} \mathbf{A}(\vec{x}_0)^T \delta \vec{y}$$

Here,  $\mathbf{A}$  is the Jacobian matrix (first-order partial derivatives of the function  $\vec{F}(\vec{x})$ ) which determines the value of the iterative solution with respect to  $\vec{x}$ . Therefore, the implementation of automatic differentiation (AD) is addressed as the optimized approach for the Jacobian calculation in PILS. It offers large advantages, both for computational efficiency and suitable accuracy with respect to the evaluation of derivatives. PILS currently utilizes TAPENADE for generating differentiated codes. Fig. 3-27 illustrates the derivative spectra of OH in the far infrared spectral range discretized at 7 altitude levels at the tangent heights of 14 km, 16 km, respectively. It is emphasized that a strong decrease of the first derivative is displayed at both sides from the OH line triplet pair at  $\nu = 61.275 \text{ cm}^{-1}$ , and the effect of OH becomes almost invisible around the regions of  $\nu < 61 \text{ cm}^{-1}$  and  $\nu > 61.5 \text{ cm}^{-1}$ .

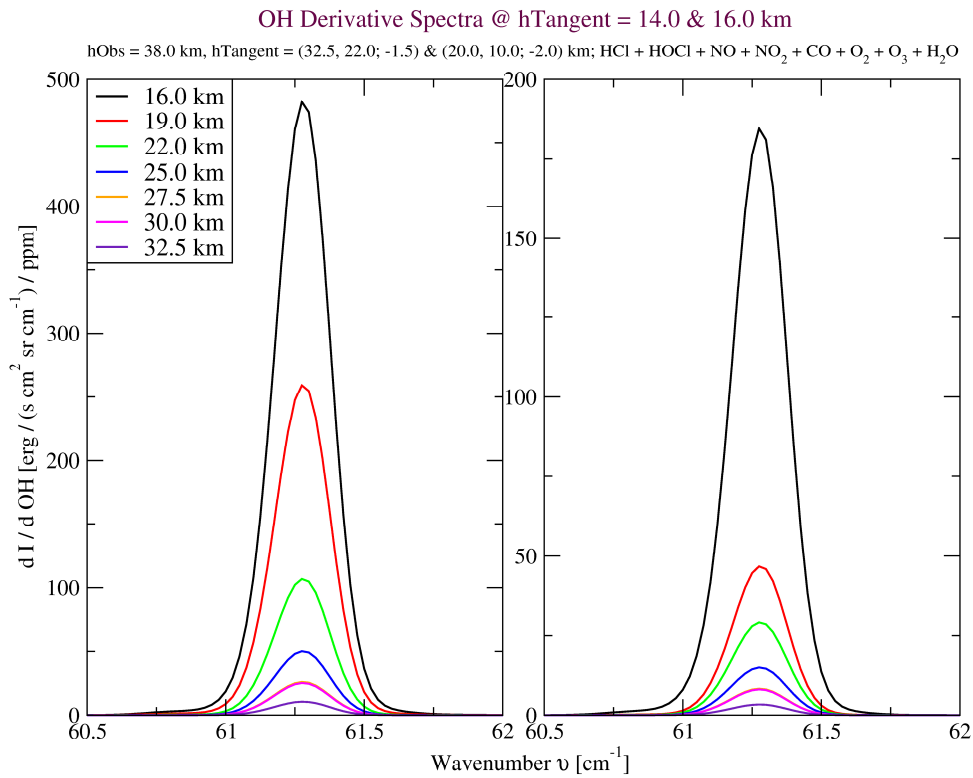


Fig. 3-27: OH derivative spectra at 7 altitude levels simulated at the tangent heights of 14 km and 16 km

Regarding the inversion problems the algorithm relies on the use of a collection of optimization routines contained in the public part of the PORT library. For our purpose we utilize the routine DN2G. Essentially, the retrieval of atmospheric state parameters from observed spectra is an ill-posed problem. To stabilize the inversion process we impose the regularization matrix  $\mathbf{L}$  constraining the solution. The augmented residual vector  $\mathbf{R}_\alpha$  and Jacobian matrix  $\mathbf{A}_\alpha$  are then computed by

$$\mathbf{R}_\alpha = \begin{bmatrix} \bar{F}(\bar{x}) - \bar{y} \\ \sqrt{\alpha} \mathbf{L}(\bar{x} - \bar{x}_a) \end{bmatrix} \quad \text{and} \quad \mathbf{A}_\alpha = \begin{bmatrix} \mathbf{A} \\ \sqrt{\alpha} \mathbf{L} \end{bmatrix}$$

Where  $\alpha$  is a parameter of Tikhonov regularization,  $\mathbf{L}$  can be chosen as the Cholesky factor of an *a priori* profile covariance matrix  $\mathbf{C}_x$  that is given by

$$[\mathbf{C}_x]_{ij} = \sigma_{x_i} \sigma_{x_j} [\bar{x}_a]_i [\bar{x}_a]_j \exp\left(-\frac{(z_i - z_j)}{l_{cor}}\right) \quad \text{with} \quad i, j = 1, \dots, n$$

Here,  $l_{cor}$  is a length determining the correlation between the parameters at different altitudes.

A number of retrievals using synthetic measurements have been studied in order to verify the feasibility of forward model and inversion algorithm. Fig. 3-28 shows the estimated ozone ( $\text{O}_3$ ) concentration profile retrieved from the synthetic limb sounding spectra with 14 tangent altitudes ranging from 10.0 to 32.5 km with steps of 2.0 or 1.5 km which largely resembled typical TELIS observations in the 1.8 THz channel. The exact  $\text{O}_3$  profile as well as temperature, pressure, OH, HCl, HOCl, NO,  $\text{NO}_2$ , CO,  $\text{O}_2$ , and  $\text{H}_2\text{O}$  profiles were taken from the US standard atmosphere. The artificial noise defined by a Gaussian distribution and given signal-to-noise ratio (SNR) was added to the simulated spectra. The *a priori* and initial profile of  $\text{O}_3$ ,  $\bar{x}_a$  and  $\bar{x}_0$ , respectively, were assumed to be identical and were given as a scaled exact profile, i.e.  $\bar{x}_a = \bar{x}_0 = 2.0 \hat{x}_0$ . A retrieval grid with 3 km and 2.5 km spacing was selected. The inversion performance is acceptable using the forward model and retrieval algorithm of PILS as demonstrated in Fig. 3-28. Furthermore, Fig. 3-29 illustrates the corresponding relative errors of the retrieved profile of  $\text{O}_3$  with respect to different regularization matrices (different values of  $l_{cor}$ , identical  $\alpha$ ). The value of the regularization parameter  $\alpha$  was previously decided by the procedure of singular value decomposition. It is clear that larger values of  $l_{cor}$  result in convergence toward a solution with small relative error with respect to the exact solution. The best solution was obtained in the case  $l_{cor} = 40$  km.

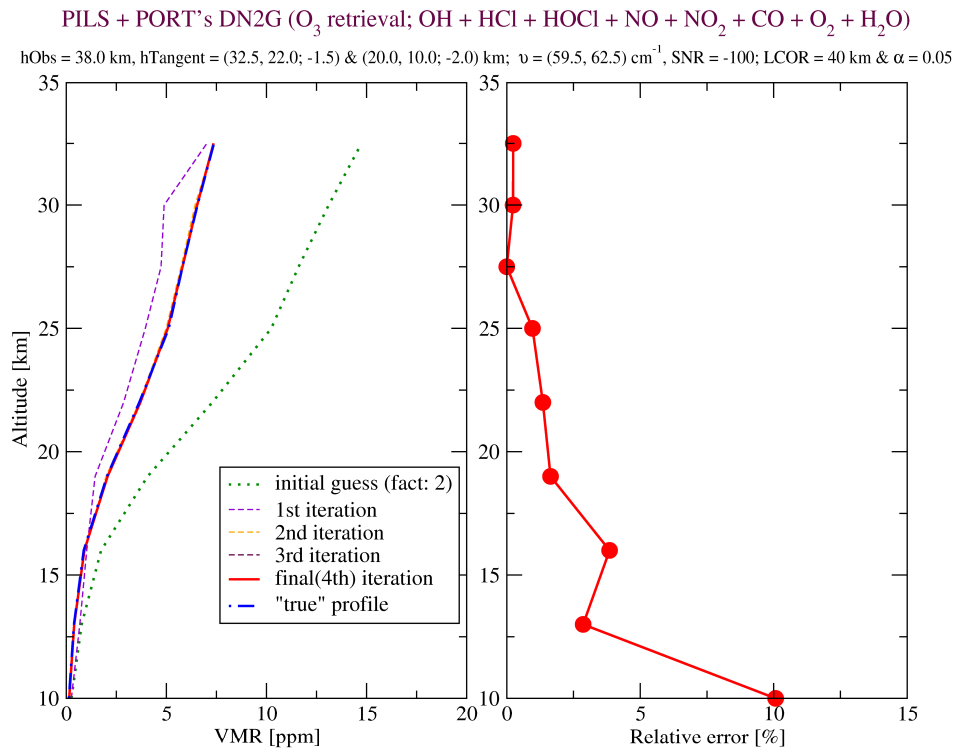


Fig. 3-28: Result of ozone retrieval according to each iteration and its relative error

### Comparison of Relative Errors for $l_{cor}$ ( $O_3$ retrieval; $OH + HCl + HOCl + NO + NO_2 + CO + O_2 + H_2O$ )

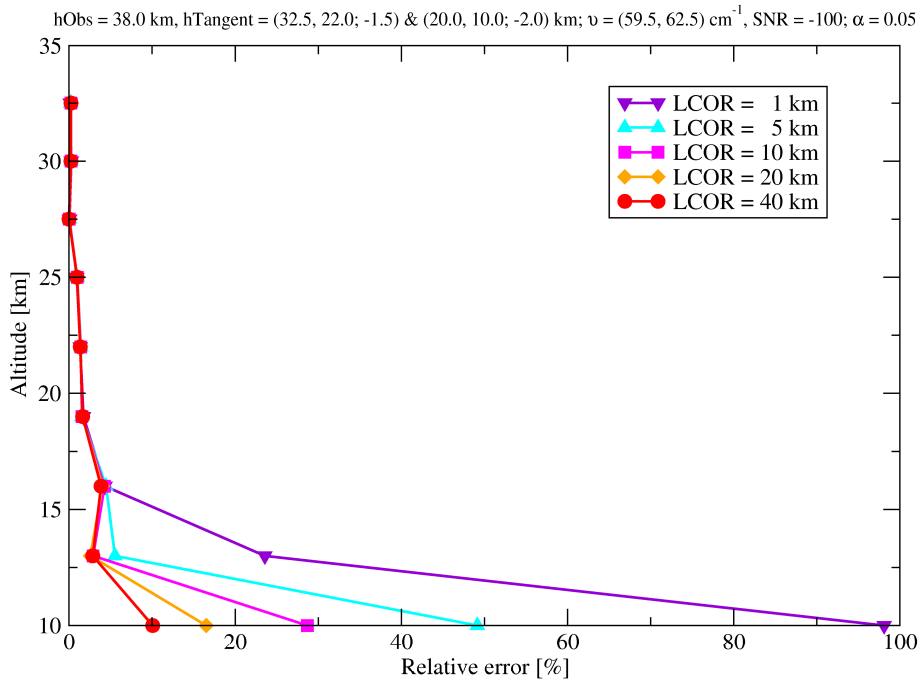


Fig. 3-29: Result of relative errors for regularization matrix described by different  $l_{cor}$

The new code PLS appears to be a promising program ready to derive atmospheric profiles by analyzing IR/MW limb sounding measurements.

### 3.14 Textbook on Numerical Regularization for Atmospheric Inverse Problems

A. Doicu, T. Trautmann, F. Schreier

The textbook *Numerical Regularization for Atmospheric Inverse Problems* was published in 2010 by Springer in their Praxis series. It is devoted to a comprehensive treatment of regularization techniques for atmospheric science and for further developments in this field. Currently there is no other monograph that would cover the wide range of applications in remote sensing. The style of this book is on an advanced mathematical level presenting and analyzing numerical algorithms for atmospheric retrieval by pulling together all the relevant material in a consistent, powerful manner.

The retrieval problems arising in atmospheric remote sensing belong to the class of the so-called *discrete ill-posed problems*. These problems are unstable under data perturbations, and can be solved by numerical regularization, in which the solution is stabilized by accounting on additional information.

The book focuses on the following topics:

- Many computational aspects are treated and a selection of theoretical results is discussed;
- state-of-the-art numerical methods for solving discrete ill-posed problems are surveyed;
- various methods are illustrated with examples taken from the field of atmospheric remote sensing;
- relevant inverse methods from classical regularization theory are presented, together with approaches from statistical inversion.

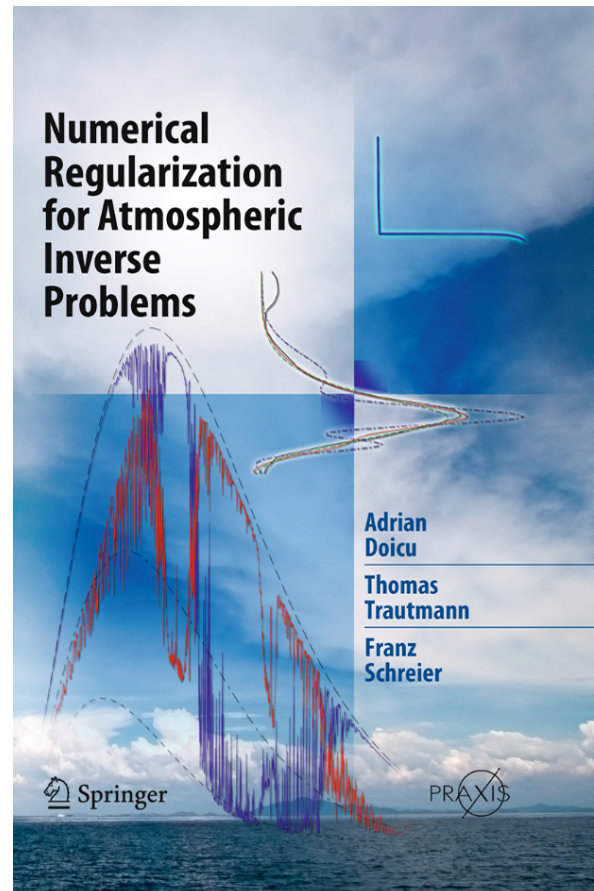
**Chapter 1** presents typical retrieval problems encountered in atmospheric remote sensing, while **Chapter 2** introduces the concept of ill-posedness for linear discrete equations. Here the difficulties associated with the solution of these problems are illustrated by considering a temperature retrieval test case and analyzing the solvability of the discrete equation by using the singular value decomposition of the corresponding matrix.

Next **Chapter 3** deals with a detailed description of Tikhonov regularization for linear problems. In this context a set of mathematical and graphical tools is introduced which permits to fully characterizing the regularized solution. The goal of **Chapter 4** is to reveal the similarity between Tikhonov regularization and statistical inversion regarding the regularized solution representation, the error analysis, and the design of parameter choice methods. In **Chapter 5** a brief survey of some classical iterative regularization methods is given, such as the *Landweber* iteration and semi-iterative methods, followed by a discussion of the regularization effect of the conjugate gradient method when applied to the normal equations.

The remaining chapters of the book are devoted to nonlinear ill-posed problems. Four typical test problems are introduced which are used throughout the rest of the book to illustrate the behaviour of the numerical algorithms and tools. These test problems from atmospheric remote sensing deal with the retrieval of ozone and BrO in the visible spectral region, and of CO and temperature in the infrared spectral domain.

**Chapter 6** discusses some practical aspects of Tikhonov regularization for nonlinear problems, while **Chapter 7** deals with the relevant iterative regularization methods for nonlinear problems. A review of the truncated and the regularized total least squares method for solving linear ill-posed problems is given in **Chapter 8** by also stressing its similarity with the Tikhonov regularization. The final **Chapter 9** describes the *Backus-Gilbert* approach as a representative member of mollifier methods and, finally, addresses the maximum entropy regularization.

For the sake of completeness and in order to emphasize the mathematical techniques which are used in the classical regularization theory, ten **Appendices** at the end of the book present direct and iterative methods for solving linear and nonlinear ill-posed problems.



## 4. Atmospheric Remote Sensing – Applications

### 4.1 Remote Sensing of NO<sub>2</sub> Vehicle Emission using Mobile DOAS during Expo 2010

S. S. Wang, N. Hao

The Expo 2010 was held on both banks of the Huangpu River in the mega-city of Shanghai, China, from May 1<sup>st</sup> to October 31<sup>st</sup>, 2010. With the theme of 'Better City - Better Life', air quality of Shanghai becomes more and more attractive. Vehicle population increased with an average rate of 10% per year in the last decade, and there more than 2.85 million vehicles are registered in Shanghai nowadays, equivalent to more than doubling the vehicle population of 2000 (*Shanghai Municipal Bureau of Statistics*). Thus, vehicle emission has inevitably become a major source of urban air pollution with the reduction of industrial pollutant discharge.

In order to better understand the NO<sub>2</sub> vehicle emission of Shanghai, we performed the mobile DOAS field measurements by encircling the Inner Ring Viaduct Road (IRVR) in Shanghai during the Expo 2010 opening ceremony from April 30<sup>th</sup> to May 9<sup>th</sup>. A schematic of the overall mobile DOAS system is shown in Fig. 4-1 (*Wang et al. 2009*).

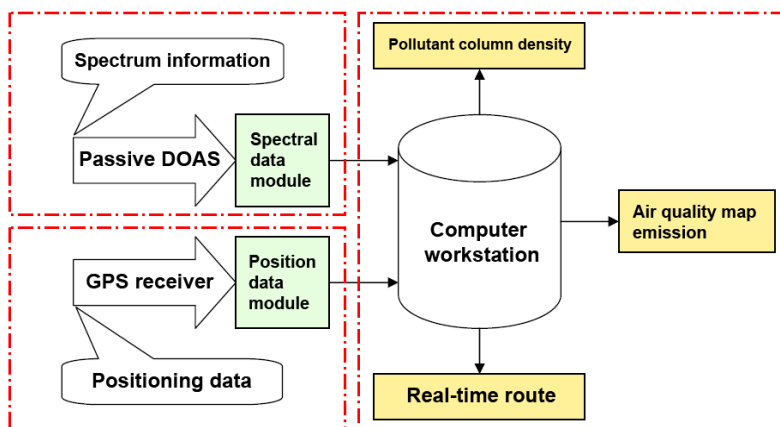


Fig.4-1: Framework of the mobile DOAS system

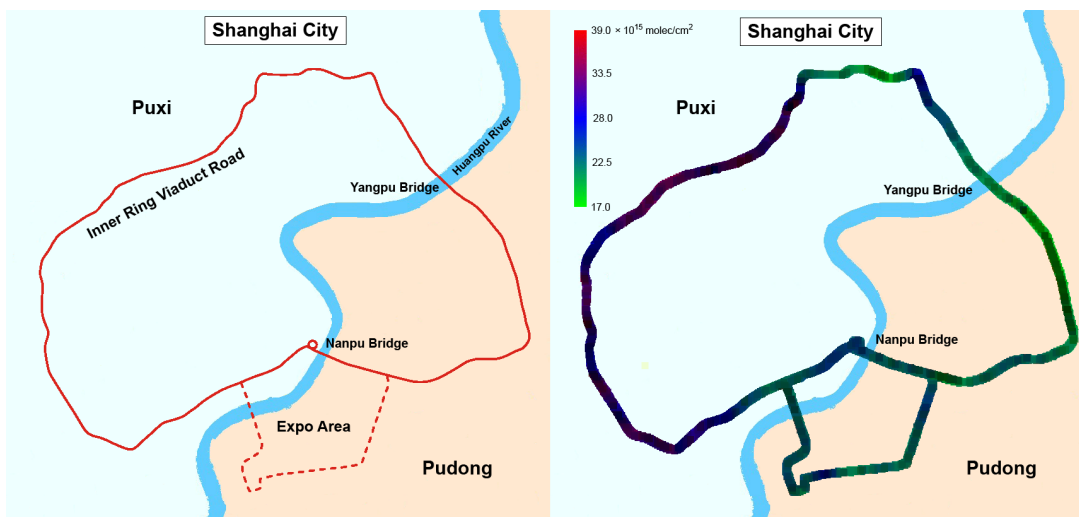


Fig.4-2: Inner ring road with sections. The Expo area is indicated as well (left). The right panel displays the spatial distribution of NO<sub>2</sub> differential vertical column densities along the IRVR and Expo road.

With 48 km length, the IRVR can be divided into 29 km in Puxi, 8 km in Pudong and 11 km of two bridges spanning the Huangpu River named *Nanpu Bridge* and *Yangpu Bridge* which connect the IRVR between Puxi and Pudong part. Fig. 4-2 (left) illustrates the ring roads and IRVR sections.

Spatial distribution of NO<sub>2</sub> differential vertical column densities (DVCD) along the route can be seen in the right part of Fig. 4-2. The measurement indicates that all the NO<sub>2</sub> DVCDs are comparable from  $17.66 \times 10^{15}$  molec/cm<sup>2</sup> to  $35.63 \times 10^{15}$  molec/cm<sup>2</sup> during the total encirclement. From the absence of a predominant peak value, we can infer that there is no obvious pollutant source of traffic congestion as NO<sub>2</sub> emitted from the vehicles spread all over the area. The NO<sub>2</sub> DVCD average value of the Pudong part is lower than the average value of the Puxi part. This could be e.g. due to the fact that the building density in the Pudong district is 20% lower than in the other central districts where IRVR passes through. Less buildings, together with lower building height, may enhance the exchange of air thus helping to diffuse pollutants. Furthermore, the roadside trees and greenbelt also have effects on the diffusion of NO<sub>2</sub>.

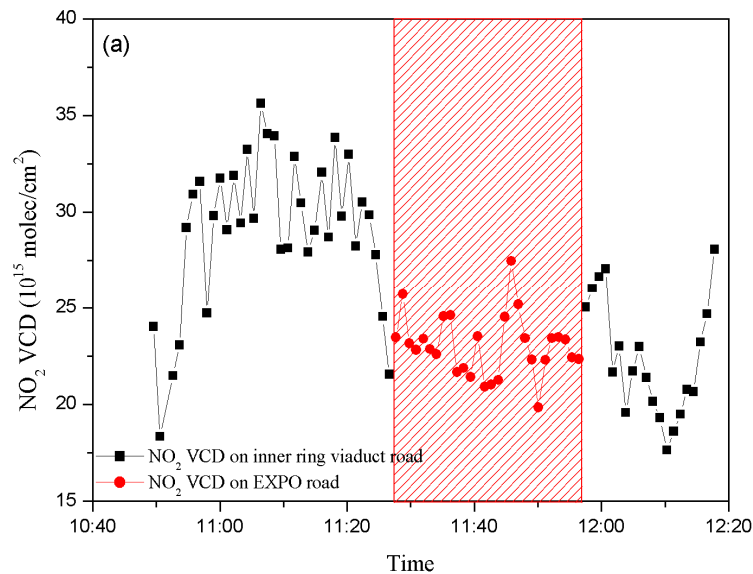


Fig. 4-3: IRVR and Expo road measurements on the day of the EXPO opening ceremony (May 1<sup>st</sup>, 2010) from 10:49 to 12:18 local time.

Fig. 4-3 shows the variation of NO<sub>2</sub> DVCD with time on the Expo opening ceremony day May 1<sup>st</sup>, 2010. It is noteworthy that the NO<sub>2</sub> DVCD of the Expo Park road (red part in Fig. 4-3) is almost the lowest during the encirclement.

Based on a GIS (Geographic Information System) platform, we located the center of the area encircled by the IRVR and separated the area into an upwind part and a downwind part. NO<sub>2</sub> emission at a certain time through the traverse was calculated by multiplying the retrieved DVCD at that time by the mean value of wind speed and the distance traversed perpendicular to the pollutant transport direction in case of pollutant transports along the wind direction. Then the total emission of the pollutant inside the enclosed area is the difference between the outflow of the downwind and the inflow of the upwind parts. Most of the calculated daily NO<sub>2</sub> vehicle emissions are positive which indicates that the large area encircled by the IRVR emits pollutants to the outside. Estimates of the average value of NO<sub>2</sub> vehicle emission from the central urban area amount to 1.8 ton/h. While the IRVR is regarded as the boundary of the central urban area, the calculated emission would cover most of the NO<sub>2</sub> vehicle emission from Shanghai's core area. The calculated NO<sub>2</sub> vehicle emission of the central urban area varies from 0.61 ton/h to 4.86 ton/h leading to an average annual NO<sub>2</sub> vehicle emission of  $1.58 \times 10^4$  ton. The NO<sub>2</sub> vehicle emission quantified by mobile DOAS measurement is comparable with the reported emission inventories of 2006, i.e.  $1.8 \times 10^4$  ton/year NO<sub>x</sub> within IRVR (Fu 2009). The discrepancies between NO<sub>x</sub> inventories and quantified NO<sub>2</sub> can be explained by the amount of NO which has not been oxidized. The mobile DOAS field measurements are capable of verifying the accuracy of emission inventories and providing them with additional pollutant data.

## References

Shanghai Municipal Bureau of Statistics: Shanghai Statistical Yearbook 2001~2010, China Statistics Press, Beijing, 2010

Wang, S.S. et al.: Application of vehicle-borne passive differential optical absorption spectroscopy for urban traffic air pollution monitoring, *Acta Optica Sinica* 29, 2645-2649, 2009

Fu, Q.Y.: Emission inventory and the formation mechanism of high pollution of fine particulate matters in Shanghai, Fudan University, 2009

## 4.2 Air Quality Measurements for the Expo 2010 in Shanghai from Space

N. Hao, P. Valks, D. Loyola, W. Zimmer

Shanghai (31°14'N, 121°29'E), the largest city in China, held the World Exposition (Expo 2010) from May 1<sup>st</sup> to October 31<sup>st</sup>, 2010, with more than 70 million visitors. Located on the Yangtze River delta, Shanghai enjoys comparatively better geographic conditions than Beijing, enabling easier dispersion of air pollutants. However, the local soot, SO<sub>2</sub> and NO<sub>2</sub> emissions in Shanghai were 2-3× higher than those in Beijing during 2003-2005 (Chan and Yao 2008). Its fast growing economy, long history of industrial development and rapidly industrializing neighboring provinces pose large challenges to the air quality of Shanghai. To improve the air quality during the Expo 2010, many emission control measures (ECMs) focusing on energy, industry, transport and construction were implemented since 2002 and an Air Quality Plan (2009-2011) special for the Expo was implemented. Moreover, the short-term ECMs were brought forward for several pollution sources that greatly affect the air quality in Shanghai, including joint pollution prevention and control in the Yangtze River Delta, straw burning ban, suspending work at factories and construction sites.

Satellite observations can provide unique insights into the regional air quality around Shanghai and air pollution transport from surrounding provinces. At IMF-AP, we have assessed the effectiveness of these controls and studied the impact on pollutants over Shanghai and neighboring provinces during the Expo using operational GOME-2 products processed by DLR in the framework of the O3M-SAF and data from Terra's MOPITT (Measurements of Pollutants in the Troposphere) and MODIS (Moderate Resolution Imaging Spectroradiometer).

First, we compared aerosol optical thickness (AOT) based on MODIS data from the Aqua platform (MOY08, collection 5) over Shanghai and surrounding provinces during the Expo period (May – October, 2010) and the same period from 2007-2009. Fig. 4-4 (top panel) shows that AOT has decreased by about 18% over Shanghai and surrounding provinces during the Expo period, compared to the same period in the previous years (2007-2009). Similar decreases in the PM10 (Particulate Matter) concentrations in Shanghai during the Expo were reported by a Mid-Expo Air Quality Report (*Clear Air Initiative for Asian Cities Center 2010*). Furthermore, we compared AOT for the period January-April 2010 when no emission control measures were applied, with the same period from 2007-2009. As shown in Fig. 4-4 (bottom panel), there is increase of AOT over Shanghai and surrounding areas during this period, compared to 2007-2009. These results indicate that the emission control measures could have played an important role in the aerosol reduction during the Expo period. Here, it is important to note that besides the emission reductions, the meteorological conditions could also have a large effect on the aerosol load as well.

Analysis of satellite data from GOME-2 and OMI had shown that short-term ECMs, especially removing half of the cars from the roads, contributed to a decrease of 43%-59% in NO<sub>2</sub> columns over Beijing during Olympic period (Mijling et al. 2009). It was however impossible to implement the similar strict traffic control measures as Olympic Games during the Expo period because of its much longer time coverage (6 months). To analyze the NO<sub>2</sub> pollution during the Expo period, we compared GOME-2 tropospheric NO<sub>2</sub> for May – October 2010 with the same period in previous years. As listed in Table 4-1, GOME-2 observed similar NO<sub>2</sub> columns during the Expo period and before the Expo (January – April), compared to 2007-2009. These results are expected because no short-term traffic control measures were implemented over Shanghai and surrounding areas during the Expo period.

	Mean NO <sub>2</sub> Column (10 <sup>15</sup> molec/cm <sup>2</sup> )		Δ (%)
	2007-2009	2010	
January – April	21.5 ± 3.7	20.8 ± 3.0	-3.3
May – October	15.8 ± 3.4	15.7 ± 3.9	-0.6

Table 4-1: Mean tropospheric NO<sub>2</sub> columns (10<sup>15</sup> molec/cm<sup>2</sup>) over Shanghai (30.7°-31.7° N, 120.9°-121.9° E) between January to April 2010 (before Expo) and May to October 2010 (Expo period) together with the same period from 2007 to 2009

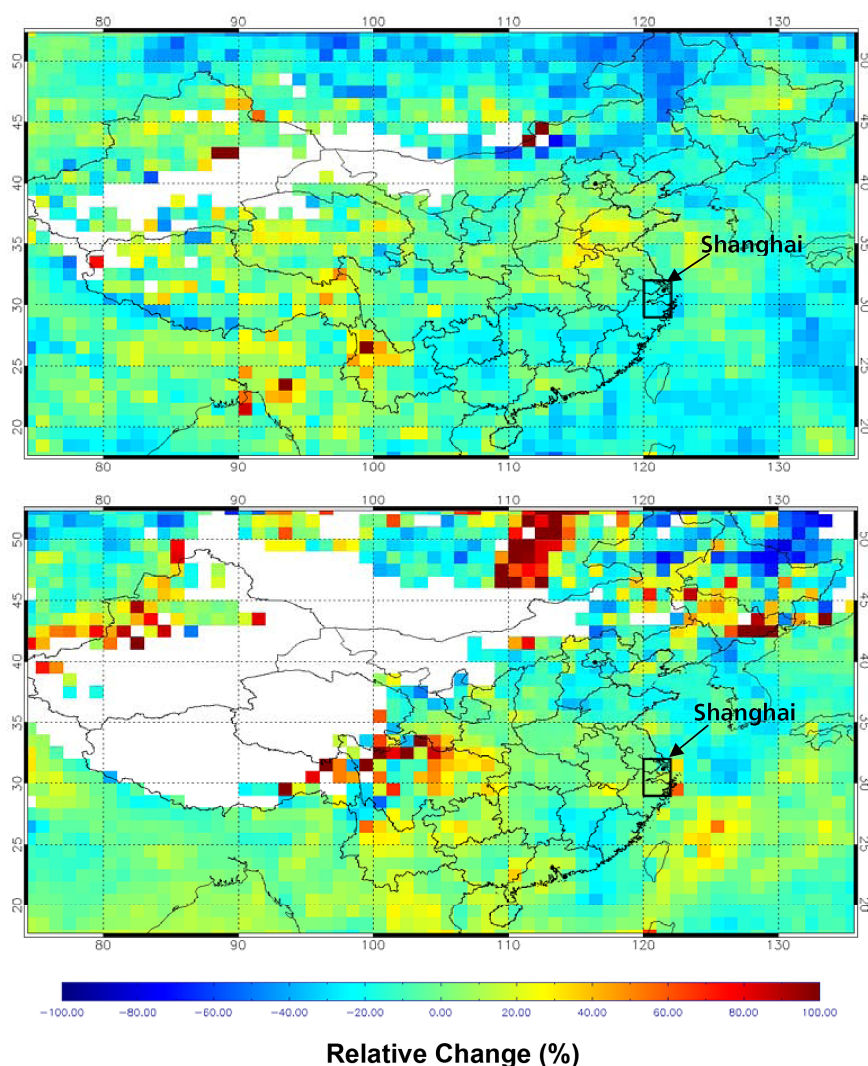
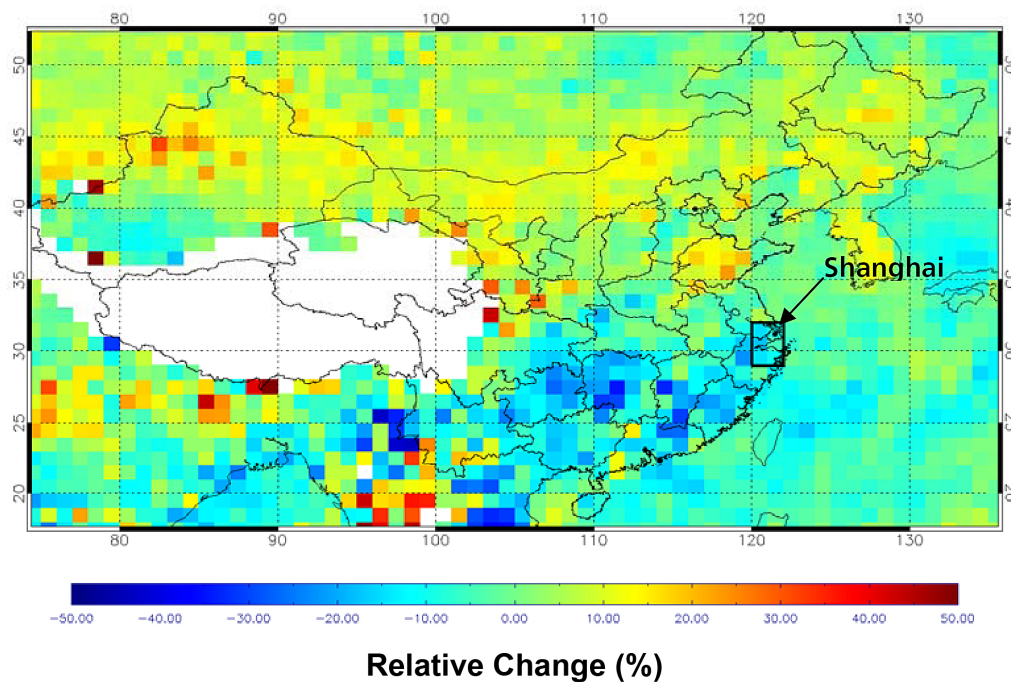


Fig. 4-4: Top: Relative change of mean AOT between May – October 2010 (Expo period) vs. 2007-2009 (reference period). Bottom: Same as above but for the periods January to April 2010 (before Expo) vs. the reference period. Negative values indicate a smaller AOT in 2010, white pixels correspond to missing data.

We used from MOPITT the monthly average CO mixing ratio at the 700 hPa level because MOPITT has little sensitivity to CO within the boundary layer (BL). Compared to NO<sub>2</sub>, CO has longer chemical lifetimes above the BL and enhanced concentrations may be found further away from the emission sources (*Witte et al. 2009*). Therefore, we had to define a larger analysis domain (29°-32° N, 120°-122° E) which included Shanghai and neighboring provinces (Fig. 4-4 box). Fig. 4-5 demonstrates that the CO concentration over Shanghai and surrounding provinces decreased by about 8.7 % during the Expo period, compared to previous years (2007-2009) for the same month. The monthly mean CO<sub>700hPa</sub> over the domain in the left panel of Fig. 4-6 shows a similar pattern of low values during the Expo period especially from July – September relative to the past three years. All these results reflect the efficiency of

ECMs imposed on industry and power plants in Shanghai and the surrounding regions. However, it remains to be seen whether the relatively clean air over Shanghai will persist.



Fi. 4-5: The relative changes of  $CO_{700hPa}$  between May – October, 2010 and May – October in the reference period (2007-2009).

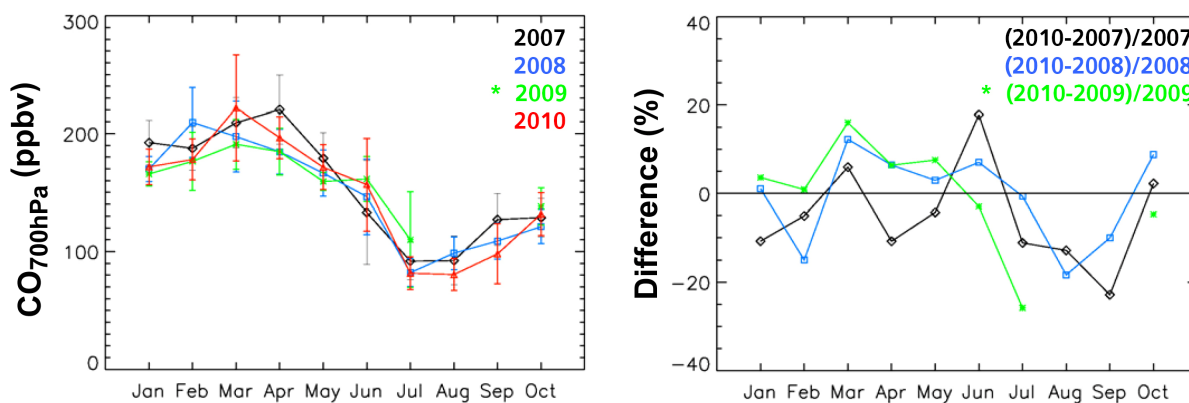


Fig. 4-6: Left: Monthly mean time series of  $CO_{700hPa}$  (ppbv) from 2007-2010 (January – October). Vertical bars are the  $1-\sigma$  standard deviation. Right: Monthly difference between 2010 and the previous years (January – October).

### Reference

Chan, C.K., Yao, X.: Air pollution in mega cities in China, *Atmos. Environ.*, 42, 1-42, 2008

Mijling, B., van der A, R.J., Boersma, F.K., Van Roozendael, M., De Smedt, I., and Kelder, H.M.: Reductions of  $NO_2$  detected from space during the 2008 Beijing Olympic Games, *Geophys. Res. Lett.*, 36, L13801, doi:10.1029/2009GL038943, 2009

Witte, J.C., Schoeberl, M.R., Douglass, A.R., Gleason, J.F., Krotkov, N.A., Gille, J.C., Pickering, K.E. and Livesey, N.: Satellite observations of changes in air quality during the 2008 Beijing Olympics and Paralympics, *Geophys. Res. Lett.*, 36, L17803, doi: 10.1029/2009GL039236, 2009

Clean Air Initiative for Asian Cities (CAI-Asia) Center: Blue Skies at Shanghai Expo 2010. A Mid-Expo Air Quality Report, 2010 see <http://megaevents.cleanairinitiative.org/shanghaiexpo2010/>

### 4.3 The Eyjafjallayökull Eruption Monitored by GOME-2

*M. Rix (TUM), P. Valks, D. Loyola*

Volcanic eruptions can inject large quantities of volcanic ash and gases into the atmosphere. Depending on the strength of the eruption, the height of the emissions can vary between the summit height of the volcano up to 20 km or higher, e.g. as seen 1991 during the Pinatubo eruption on the Philippines. The ash emitted by volcanic eruptions is known to be the primary hazard to aviation in volcanic clouds. The ash can cause severe damages to aircraft from disrupting avionics and navigation systems, limiting the view of the pilots and severely scratching forward facing surfaces of aircraft to stalling engines as a result of ash melting in the aircraft's engines. Most dangerous are explosive magmatic eruptions where the thermal energy allows the eruption plume to reach the cruising altitudes of jet aircraft. Besides ash, volcanic eruption clouds contain large amounts of gases as these are the driving forces during explosive eruptions. Typically the dominant gases are water vapor, carbon dioxide, and sulfur dioxide (SO<sub>2</sub>). Of these gases SO<sub>2</sub> is itself a hazard to aircraft as it reacts with water to form sulfuric acid which is highly corrosive and may therefore damage the paint and windows of aircraft and can create sulfate deposits in the engines. The latter may block the cooling holes and lead to engine overheating. Although the SO<sub>2</sub> and ash may separate into distinct clouds as the ash drops to lower altitudes due to gravity effects and may be transported into different directions under conditions of vertical wind shear, the presence of SO<sub>2</sub> is a good indicator for volcanic eruption plumes and the presence of ash.

The eruption of the Eyjafjallayökull in southern Iceland, starting April 14<sup>th</sup> and lasting until May 23<sup>th</sup>, 2010, demonstrated the severe impacts such volcanic events can have on global mobility. Explosive activity started on April 14<sup>th</sup>, 2010; the first phase of the eruption produced an ash rich plume of 5-9 km altitude and lasted until April 17<sup>th</sup>. The prevailing winds carried the ash to the southeast and south towards the European continent where air traffic had to be stopped to a large extent. While until May 4<sup>th</sup> the activity had dropped, it picked up again, producing ash columns of up to 9 km height, which again resulted in partial closure of the European airspace. The activity of the Eyjafjallayökull volcano ended May 23<sup>th</sup>. Although the eruption of Eyjafjallayökull can be considered fairly small (Volcanic Explosivity Index = 2-3) it caused Europe-wide disruption to aviation for several days leaving thousands of passengers stranded at airports throughout Europe. The economic loss due to the eruption was estimated at about 2.5 billion € in total.

During the eruptive period the operational near-realtime retrieval of SO<sub>2</sub> at IMF-AP allowed a continuous monitoring of the volcanic plume. During the eruptive episode until May 4<sup>th</sup> only small amounts of sulfur dioxide were detected by GOME-2 and other satellite instruments, mainly close to the volcano. However during the activity following May 4<sup>th</sup>, large amounts of SO<sub>2</sub> were emitted into the atmosphere, and the volcanic gas plume could be traced by GOME-2 for several days. After the intensity of the eruption picked up again an SO<sub>2</sub>, rich eruption plume was detected on May 5<sup>th</sup> that was distributed to the south-east and covered North-Ireland and parts of the UK. The following day the plume could be detected directly to the south of Iceland. On May 7<sup>th</sup> and 8<sup>th</sup> the GOME-2 observations showed that part of the volcanic cloud was transported towards Spain. This led to the closure of the airspace over parts of southern and central Europe the following day. The observations agree very well with the modeled plume forecast of the London Volcanic Ash Advisory Centre (VAAC – UK MetOffice: [www.metoffice.gov.uk/aviation/VAAC](http://www.metoffice.gov.uk/aviation/VAAC)) as illustrated in Fig. 4-7. The following days (May 9<sup>th</sup> – 12<sup>th</sup>) the SO<sub>2</sub> plume could be observed south of Iceland over the Atlantic leaving Europe mainly unaffected, with only small parts of the plume touching Ireland on May 11<sup>th</sup> and France on May 12<sup>th</sup>. From May 14<sup>th</sup> – 17<sup>th</sup> GOME-2 SO<sub>2</sub> results demonstrate how the volcanic plume was again southbound by the prevailing winds. This leads to airspace closure over Ireland and the UK on May 16<sup>th</sup> and 17<sup>th</sup>. GOME-2 SO<sub>2</sub> emissions from the Eyjafjallayökull eruption could be detected until the eruption finally ceased on May 23<sup>rd</sup>.

During the eruption a new method was tested that has been developed at IMF-AP to retrieve the SO<sub>2</sub> plume height in near-realtime. The retrieval uses the fact that the altitude of the SO<sub>2</sub> layer in the atmosphere determines the proportion of photons that pass the absorbing layer on their way to the sensor. The higher this altitude, the more photons are Rayleigh scattered below and therefore pass through the SO<sub>2</sub> layer resulting in more prominent SO<sub>2</sub> absorption structures in the measured radiances. If the layer is low in the atmosphere more photons are scattered above. Therefore the measured

radiances also contain information about the SO<sub>2</sub> plume height. Using the SO<sub>2</sub> column amount from the operational DOAS retrieval, the height of the plume can be estimated by matching the measured radiances with simulations performed for different plume heights. Input parameters for the simulations include SO<sub>2</sub> column, ozone column, viewing geometry, surface albedo, cloud fraction and cloud top albedo. The input parameters are taken from the operational GOME-2 product at IMF-AP. Using these input parameters, backscatter radiances are simulated for different assumed plume heights, which are currently 2 km, 5 km, 7 km, 9 km, 11 km, 13 km and 15 km. The simulated spectra are then matched with the measurement and the one with the smallest residual, that is the one that shows the smallest difference to the measured spectrum, is selected as the most likely plume height. If this plume height is not equal to the plume height assumed for the DOAS retrieval in the first step, the retrieval is redone with the new plume height and the whole process is repeated. This is iterated until assumed and retrieved plume height converge. For the Eyjafjallayökull eruption plume on May 5<sup>th</sup> the retrieval shows plume heights mainly between 7-11 km (Fig. 4-8). The reported plume height at the volcano for that day was around 9 km and matches well with the retrieved heights. Trajectory modeling suggests plume heights between 6-14 km for May 5<sup>th</sup>, i.e. the retrieved plume altitudes are well within the possible range.

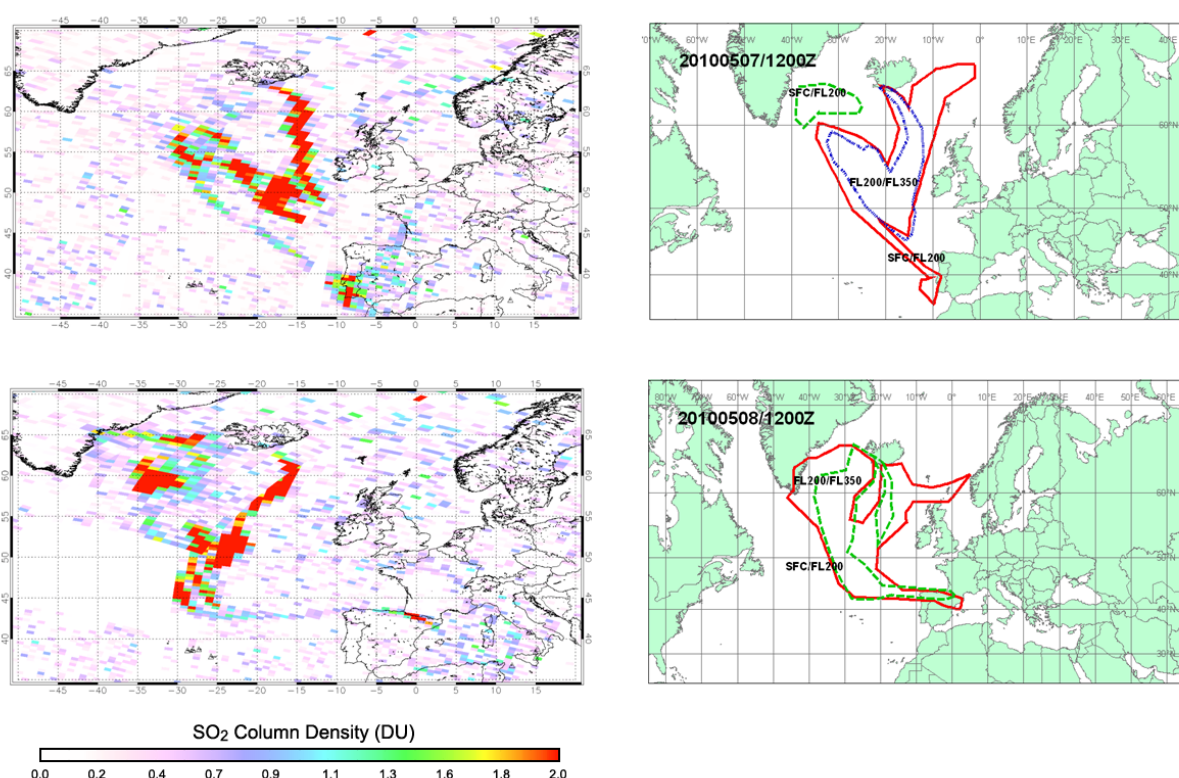


Fig. 4-7: Volcanic SO<sub>2</sub> cloud from Eyjafjallayökull eruption as seen by GOME-2 on May 7<sup>th</sup> and 8<sup>th</sup> (left). The GOME-2 observations agree well with the plume forecast of the UK MetOffice using the NAME dispersion model (right).

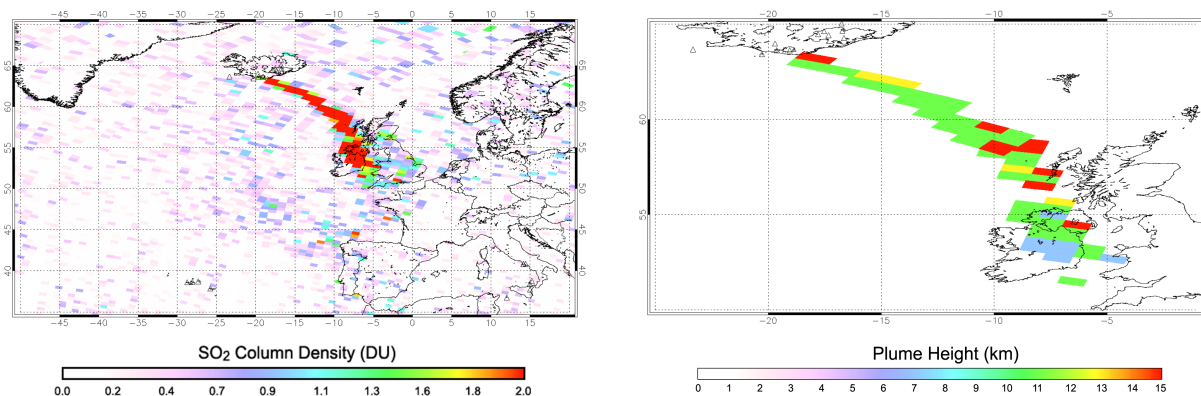


Fig. 4-8: Volcanic SO<sub>2</sub> plume from Eyjafjallayökull eruption (left) and estimated plume height (right) on May 5<sup>th</sup> 2010

#### 4.4 Operational O3M-SAF Trace Gas Column Products: GOME-2 NO<sub>2</sub>, BrO, SO<sub>2</sub>, CH<sub>2</sub>O and H<sub>2</sub>O

*P. Valks, N. Hao, M. Rix (TUM), S. Slijkuis, D. Loyola, W. Zimmer and S. Emmadi (TUM)*

The GOME-2 column products of ozone and the other minor trace gases NO<sub>2</sub>, BrO, SO<sub>2</sub>, HCHO and H<sub>2</sub>O have been developed by IMF-AP in the framework of EUMETSAT's Satellite Application Facility on Ozone and Atmospheric Chemistry Monitoring (O3M-SAF). These trace gas column products are generated operationally at DLR using the GOME Data Processor (GDP) version 4.4 (Valks et al. 2010).

##### Total and tropospheric Nitrogen Dioxide (NO<sub>2</sub>)

Nitrogen dioxide plays a key role in both stratospheric and tropospheric chemistry. In the stratosphere, it is involved in ozone destruction, while in the troposphere, NO<sub>2</sub> is an important air pollutant and ozone precursor. The total NO<sub>2</sub> column is retrieved from GOME-2 solar backscattered measurements spectra using the Differential Optical Absorption Spectroscopy (DOAS) method in the 425-450 nm wavelength range. An additional algorithm is applied to retrieve the tropospheric NO<sub>2</sub> column (Valks et al. 2011). The operational dissemination of the GOME-2 total and tropospheric NO<sub>2</sub> products started in 2008, and the NO<sub>2</sub> product is available for the users in near-realtime, i.e. within two hours after sensing. Fig 4-9 shows the tropospheric NO<sub>2</sub> columns from GOME-2 for the period 2007-2009 over East Asia. The world's largest area with high NO<sub>2</sub> pollution is found above east China, which is a result of China's spectacular economic growth during the last decade, accompanied by a strong increase in emissions of air pollutants.

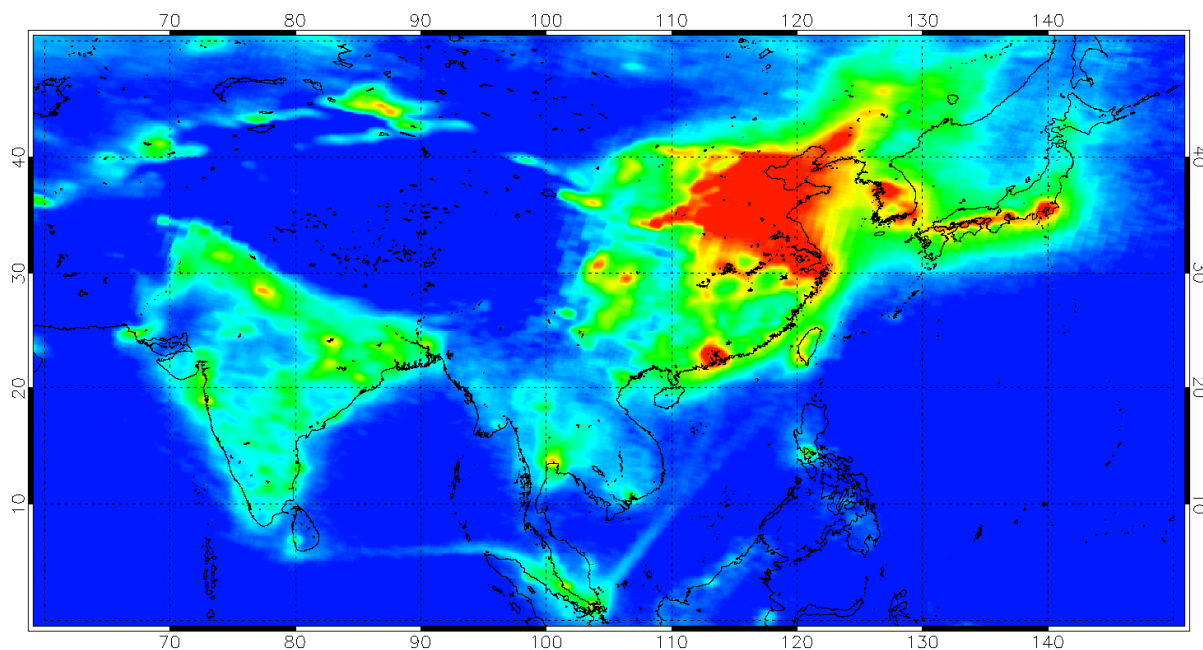


Fig. 4-9: Average tropospheric NO<sub>2</sub> columns measured by GOME-2 over East Asia for 2007-2009.

##### Bromine Oxide (BrO)

Inorganic bromine Br<sub>y</sub> (Br, BrO, BrONO<sub>2</sub>, BrOH, BrCl, HBr) is the second most important halogen affecting stratospheric ozone. In the troposphere large emissions of inorganic bromine occur during the polar springtime period resulting in Ozone Depletion Events (ODEs). BrO is the only compound within the Br<sub>y</sub> family to be measured routinely. The GOME-2 BrO slant column density is calculated with the DOAS method in the UV wavelength region 336-351.5 nm. The vertical BrO column is given by the ratio of the slant column density to the stratospheric air mass factors which are derived from a chemistry transport model (CTM) climatology of stratospheric BrO profiles. Fig 4-10 displays the large BrO emissions in the polar regions of both hemispheres during springtime. The GOME-2 BrO product became operational in 2009. A quantitative and refined interpretation of the satellite BrO observations requires to resolve the measured total BrO column into their stratospheric and tropospheric

contributions. It is therefore planned at IMF-AP to develop a tropospheric BrO algorithm for GOME-2 in 2011 (Theys et al. 2010).

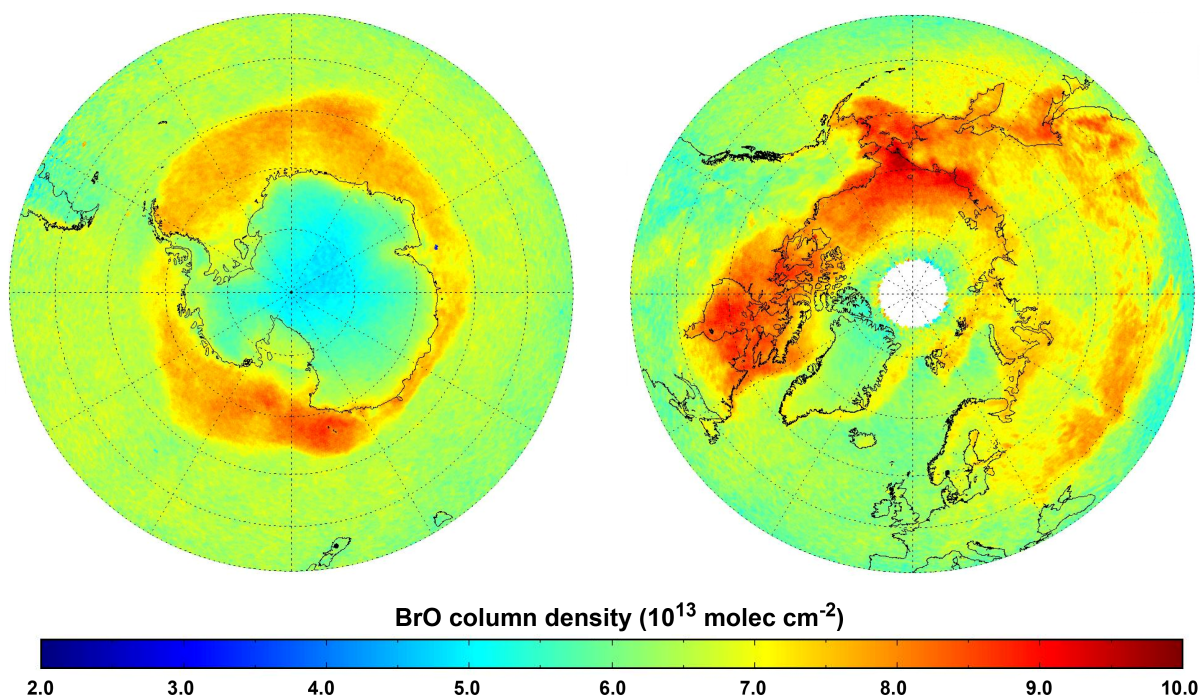


Fig. 4-10: Monthly maps of GOME-2 BrO for the SH in October 2009 (left) and for the NH in March 2010 (right).

#### Sulphur Dioxide ( $\text{SO}_2$ )

Atmospheric  $\text{SO}_2$  is an important indicator for volcanic eruptions and volcanic activity like passive degassing. Furthermore, it is produced anthropogenically in power plants, refineries, metal smelting and the burning of fossil fuels. The GOME-2  $\text{SO}_2$  column are retrieved with the DOAS method in the UV wavelength region 315-326 nm, and includes a background correction for the interference of  $\text{O}_3$  and  $\text{SO}_2$  absorption features. The volcanic air mass factors are a function of plume height and  $\text{SO}_2$  load, and a cloud correction is applied. The operational dissemination of the GOME-2  $\text{SO}_2$  product started in 2009, and the  $\text{SO}_2$  product is used for several early warning services related to volcanic hazards, such as the Support to Aviation Control Service (SACS) of ESA and the GMES European Volcano Observatory Space Services (EVOSS) (Rix et al. 2009). The GOME-2 observations of the spectacular 2010 Eyjafjallayökull eruption in Iceland are discussed in chapter 4.3 of this annual report.

#### Formaldehyde ( $\text{HCHO}$ )

Formaldehyde ( $\text{HCHO}$ ) is one of the most abundant hydrocarbons in the atmosphere and both an important indicator of non-methane volatile organic compound (NMVOC) emissions and photochemical activity. Satellite measurements of  $\text{HCHO}$  can be used to constrain NMVOC emissions in current state-of-the-art chemical transport models. The GOME-2  $\text{HCHO}$  slant column density is retrieved with the DOAS method using the 328.5-346 nm wavelength range (De Smedt et al. 2008). The vertical column density is then obtained by dividing the slant column by an appropriate air mass factor (AMF), calculated with the radiative transfer model LIDORT 3.3. Monthly averaged *a priori*  $\text{HCHO}$  profiles are obtained from the IMAGESv2 global chemistry transport model, and interpolated for each measurement location. The GOME-2  $\text{HCHO}$  product became operational in 2010.

#### Water Vapour ( $\text{H}_2\text{O}$ )

Atmospheric water vapour is the most important natural (non-anthropogenic) greenhouse gas, which accounts for about 2/3 of the natural greenhouse effect. Despite this importance, its role in climate and its reaction to climate change are still difficult to assess. Water vapour has a very high temporal and spatial variability: a global monitoring of  $\text{H}_2\text{O}$  by satellite is therefore a key to understanding its impact on climate. The GOME/SCIAMACHY/GOME-2 series of instruments will cover a projected time-span of at least 20 years, which makes them interesting for climatology studies of  $\text{H}_2\text{O}$ . The first software version for an operational  $\text{H}_2\text{O}$  product from GOME-2 was implemented 2009 (see annual report of

2009). In 2010 the retrieval algorithm was refined and further validated (Slijkhuis et al. 2010). The work has been done in close collaboration with the Max Planck Institute for Chemistry in Mainz. Figure 4-11 illustrates an example of the GOME-2 water vapour distribution for January 2008. The operational status of the GOME-2 H<sub>2</sub>O product shall be achieved in early 2011.

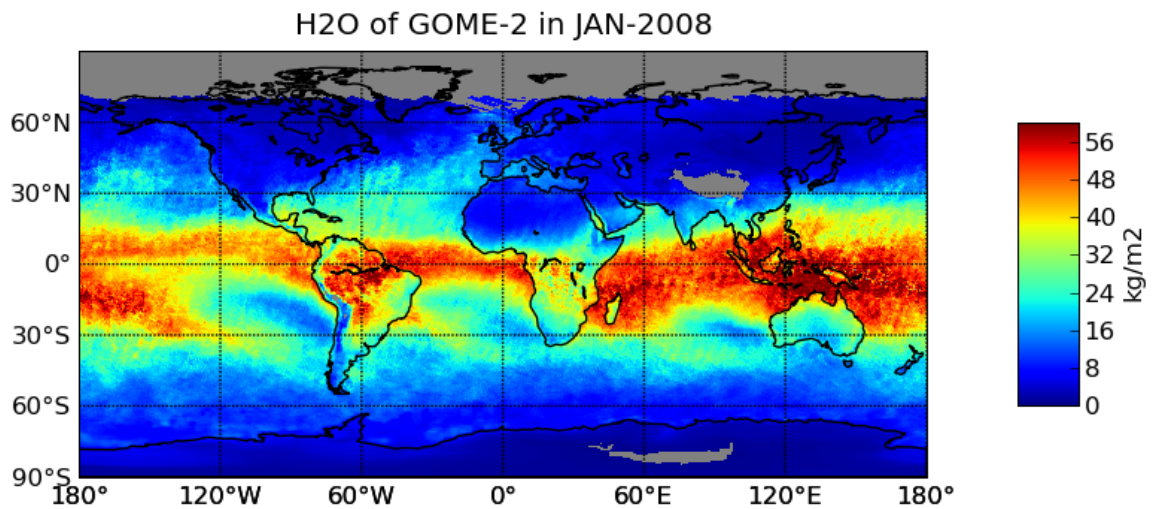


Fig. 4-11: Map of global monthly mean H<sub>2</sub>O values, with cloudy measurements removed, for January 2008.

#### References

De Smedt, I., Müller, J.-F., Stavrou, T., van der A, R., Eskes, H. and Van Roozendael, M.: Twelve years of global observation of formaldehyde in the troposphere using GOME and SCIAMACHY sensors. *Atmos. Chem. Phys.*, 8 (16), 4947-4963, 2008.

Rix, M. et al.: Satellite monitoring of volcanic sulfur dioxide emissions for early warning of volcanic hazards, *IEEE Journal of Selected Topics in applied Earth observation and remote sensing*, Vol.2, No.3, 2009.

Slijkhuis, S., Beirle, S., Mies, K., Wagner, T., Emmadi, S., Loyola, D., Zimmer, W., Kalakoski, N.: Water Vapour: A new operational O3M-SAF trace gas total column product, Proc. EUMETSAT P.57, 2010

Theys, N., Van Roozendael, M., Hendrick, F., De Smedt, I., Errera, Q., Richter, A., Begoin, M., Yang, X. and De Mazière, M.: Global observations of tropospheric BrO columns using GOME-2 satellite data, *Atmos. Chem. Phys. Discuss*, 10, 28635-28685, 2010.

Valks, P. et al.: Algorithm Theoretical Basis Document for GOME-2 Total Column Products of Ozone, Minor Trace Gases and Cloud Properties (GDP 4.2 for O3M-SAF OTO and NTO), DLR/GOME-2/ATBD/01, Iss./Rev.: 2/D, 2010

Valks, P. et al.: Operational total and tropospheric NO<sub>2</sub> column retrieval for GOME-2/MetOp, submitted to *Atmos. Meas. Tech.*, 2011.

## 4.5 Venus Modeled Spectrum and Observations with SCIAMACHY

*M. Vasquez, F. Schreier, M. Gottwald, S. Gimeno García (TUM), S. Slijkhuis, G. Lichtenberg*

SCIAMACHY on ENVISAT, although usually an instrument for remote sensing of the Earth's atmosphere, used Venus as a calibration target twice in 2009. During these observations also scientific data from the Venusian atmosphere were captured. In March 2009, Venus was close to passing right between the Earth and the Sun, i.e. inferior conjunction. During this phase SCIAMACHY mainly saw the dark side of Venus and only a very small part of the planet's atmosphere illuminated by sunlight. Thus, observing conditions mimicked a limb geometry. In June 2009, Venus was observed once again showing more than half of its disk illuminated by sunlight, corresponding to a nadir-type geometry.

### The Atmosphere and Clouds of Venus

Venus has a very dense atmosphere, mainly composed of carbon dioxide (96.5%), nitrogen (3.5%) and other minor constituents such as water vapor, sulfur dioxide, carbonyl sulfide, hydrochloric, and hydrofluoric acid (*Haus and Arnold 2010*). In addition the Venusian atmosphere also comprises layers of thick sulfuric acid clouds.

The Cloud Particle Size Spectrometer (LCPS) data on-board the Pioneer Venus Sounder probe and the nephelometer experiments detailed the cloud microstructure and cloud compositional properties of Venus by measuring the size and number density as a function of altitude (*Knollenberg and Hunten 1980*). Table 4-2 summarizes the cloud composition and properties. The main cloud deck show transition levels at 50 and 56 km, dividing the cloud system into three different regions, namely lower, middle and upper cloud regions. A region of haze was also detected above the upper cloud level, extending upwards to 90 km. The cloud system is composed of particles which have a multimodal size distribution with the smallest particles of the system composing a high and low altitude haze region.

Region	Altitude (km)	Temperature (K)	Optical Depth	Effective Diameter ( $\mu$ )	Composition
Upper Haze	70-90	225-196	0.2-1.0	0.4	H <sub>2</sub> SO <sub>4</sub> + contaminants
Upper Cloud	56.5-70	286-225	6.0-8.0	0.4, 2.0	H <sub>2</sub> SO <sub>4</sub> + contaminants
Middle Cloud	50.5-56.5	345-286	8.0-10.0	0.3, 2.5, 7.0	H <sub>2</sub> SO <sub>4</sub> + crystals
Lower Cloud	47.5-50.5	367-345	6.0-12.0	0.4, 2.0, 8.0	H <sub>2</sub> SO <sub>4</sub> + crystals
Lower Haze	31-47.5	482-367	0.1-0.2	0.2	H <sub>2</sub> SO <sub>4</sub> + contaminants

Table 4-2: Summary of Venus cloud properties.

### Radiative Transfer Model, Methodology and Results

GARLIC (Generic Atmospheric Radiation Line-by-line Infrared Code) is a versatile model that computes radiative transfer in a spherical atmosphere for up-, down-, and limb viewing geometries. Recently GARLIC has been implemented with single scattering as a first approach to simulate the effects of thin clouds and aerosols. The Venusian spectra were modeled with GARLIC for a CO<sub>2</sub> atmosphere of 100 km height. The absorption cross sections were calculated using the HITRAN spectroscopic database which contains the line parameters for a large number of molecules.

Modeling the spectrum from June assumed a nadir geometry. The final spectrum was obtained by adding two different spectra: one with a total illuminated disk and the other with a total non-illuminated disk. The illuminated and the dark fraction of the disk were calculated by taking into account the phase angle, which is known as a measure of the illuminated portion on the planet, in this case on Venus, between the planetocentric direction vectors of the Sun and Earth. With the distances to the Sun and Venus from Earth at the time when the observations took place, the phase angle was calculated to be 79.5° for a total disk illuminated-area of 59.08%. The dark and illuminated disk spectra were weighted by their fractions and added to the final spectrum. For the March spectrum a limb viewing geometry was applied since only a small portion of the planet, about 3.26% of the visible disk, was illuminated by the Sun. For this case, the observer zenith angle in GARLIC was set such that the

tangent height was above the cloud top height (~ 70 km) with the Sun at an angle of 159.2° with respect to the observer.

The depth of the molecular absorption lines can be used to determine the cloud top height. When clouds are thick, photons can hardly penetrate them, so they can be considered as reflecting surfaces. Under these conditions, photon path lengths are directly related to the cloud top height: The lower the cloud, the longer the photon path length thus raising the probability of absorption events. Therefore, the depth of the lines acts as a proxy for the estimation of the Venusan cloud top heights.

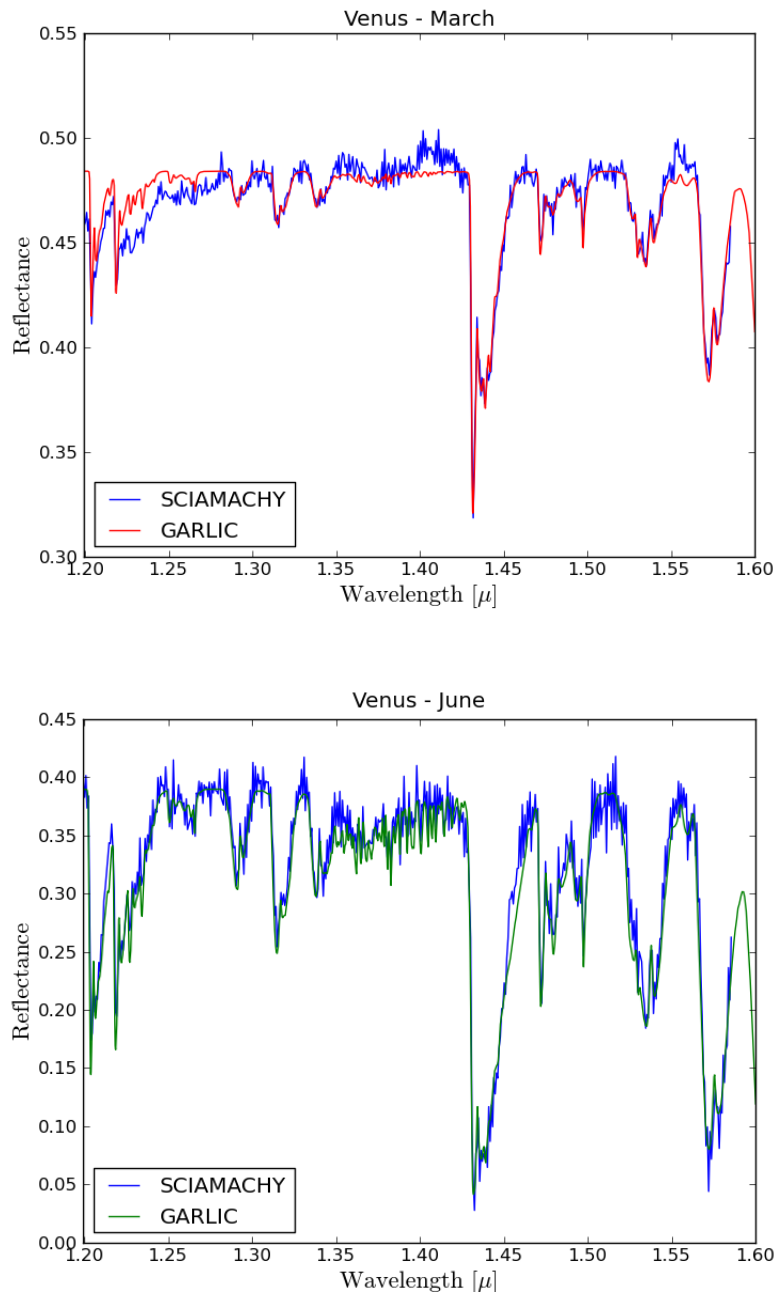


Fig. 4-12: Measured and modeled spectra from Venus in March (top) and June (bottom) 2009.

Reflecting clouds at different altitude levels were tested to simulate the measured spectra. Above the main cloud layer, a region of haze extending over 20 km was also considered. The haze optical properties were calculated by means of Mie scattering theory considering particles of 75%  $H_2SO_4$  concentration in a host medium of  $CO_2$  (Palmer and Williams 1975). An uni-modal log-normal size particle distribution of mode diameter of 0.4 with a standard deviation of 1.56, a particle albedo of 0.998 and an asymmetry parameter of approximately 0.7 was used. An extinction optical depth of

about 0.008 was considered in addition. For the June spectrum, the cloud altitude was identified at an altitude of 65 km when comparing to other altitudes in terms of the lines depth (Fig. 4-12 bottom). For the case of March, only contributions from the single scattering events above the cloud top were taken into account (Fig. 4-12 top).

### References

*Haus, R., Arnold, G.:* Radiative Transfer in the Atmosphere of Venus and Application to Surface Emissivity Retrieval from VIRTIS/VEX measurements, *Planetary and Space Science*, 58, 1578-1598, 2010

*Knollenberg, R.G., Hunten, D.M.:* The microphysics of the Clouds of Venus: Results of the Pioneer Venus Particle Size Spectrometer Experiment, *Journal of Geophysical Research*, 85, A13, 8039-8058, 1980

*Palmer, K.F., Williams, D.:* Optical Constants of Sulfuric Acid; Application to the Clouds of Venus, *Applied Optics*, 14, 208-219, 1975

## 5. Documentation

### 5.1 Books and Book Contributions

Doicu, A., Trautmann, T., Schreier, F.: Numerical Regularization for Atmospheric Inverse Problems. Springer Praxis Books in Environmental Sciences. Springer-Verlag and Praxis Publishing, ISBN 978-3-642-05438-9, 2010

Meringer, M.: Structure enumeration and sampling. In: Handbook of Chemoinformatics Algorithms CRC/Chapman&Hall, 233-267, ISBN 978-1-4200829-2-0. 2010

### 5.2 Journal Papers

Camacho, J.L., Antón, M., Loyola, D., Hernandez, E.: Influence of turbidity and clouds on satellite total ozone data over Madrid (Spain). *Annales Geophysicae*, 28, 1441-1448. DOI: 10.5194/angeo-28-1441-2010, 2010

Doicu, A., Wriedt, T.: Near-field computation using the null-field method. *Journal of Quantitative Spectroscopy and Radiative Transfer*, 111 (3), 466-473. Elsevier. DOI: 10.1016/j.jqsrt.2009.10.003, 2010

Doicu, A., Schüssler, O., Loyola, D.: Constrained regularization methods for ozone profile retrieval from UV/VIS nadir spectrometers. *Journal of Quantitative Spectroscopy and Radiative Transfer*, 111 (6), 907-916. Elsevier. DOI: 10.1016/j.jqsrt.2009.11.020. 2010

Gottwald, M.: La selenografía en los siglos XIX y XX. *Investigacion y Ciencia* (408), 64-73. Prensa Científica. 2010

Gottwald, M.: Orígenes y desarrollo de la cartografía lunar. *Investigacion y Ciencia* (407), 78-88. Prensa Científica. 2010

Loyola, D., Thomas, W., Spurr, R., Mayer, B.: Global patterns in daytime cloud properties derived from GOME backscatter UV-VIS measurements. *International Journal of Remote Sensing*, 31, 4295-4318. DOI: 10.1080/01431160903246741, 2010

Rother, T. Wauer, J.: Case study about the accuracy behaviour of three different T-matrix methods. *Applied Optics*, 49 (30), DOI: Doc. ID 133483. 2010

Rozanov, A., Kühl, S., Doicu, A., McLinden, C., Puķīte, J., Bovensmann, H., Burrows, J.P., Deutschmann, T., Dorf, M., Goutail, F., Grunow, K., Hendrick, F., von Hobe, M., Hrechanyy, S., Lichtenberg, G., Pfeilsticker, K., Pommereau, J. P., Van Roozendaal, M., Stroh, F., Wagner, T.: BrO vertical distributions from SCIAMACHY limb measurements: comparison of algorithms and retrieval results, *Atmos. Meas. Tech. Discuss.*, 3, 5079-5178, DOI:10.5194/amtd-3-5079-2010, 2010

Venema, V., Gimeno García, S., Simmer, C.: A new algorithm for the downscaling of cloud fields. *Quarterly Journal of the Royal Meteorological Society*, 136, 91-106. Royal Meteorological Society. 2010

### 5.3 Conference Proceeding Papers and Presentations

Beirle, S., Slijkhuis, S., Kalakoski, N., Loyola, D., Mies, K., Wagner, T.: Consistent Global Long Term (1995-2010) Water Vapor Observations from UV/VIS Satellite Sensors. In: Proceedings of the ESA Living Planet Symposium, ESA SP-686, Bergen, 2010

Brizzi, G., Dehn, A., Fehr, T., Niro, F., de Saavedra, M., Scarpino, G., Bovensmann, H., Gottwald, M., Lecomte, P.: ESA's Atmospheric Chemistry Mission – A Status Report. In: Proceedings of the ESA Living Planet Symposium, ESA SP-686, Bergen, 2010

Coldewey-Egbers, M., Loyola, D., Zimmer, W., Van Roozendael, M., Lerot, C., Balis, D., Koukouli, M., Dameris, M., Garny, H., Braesicke, P.: Comparison of observed and modelled global total ozone trends 1995-2009. 38<sup>th</sup> COSPAR Scientific Assembly, Bremen, 2010

Fagiolini, E., Flechtner, F., Gruber, T., Schmidt, T., Schwarz, G., Trautmann, T., Wickert, J., Zenner, L.: Quantitative Impact of Surface Pressure Variations on the Earth Gravity Field. European Geosciences Union General Assembly, Vienna, 2010

Fehr, T., Laur, H., Hörsch, B., Barois, O., Canela, M., Gessner, R., Perron, G., Raspollini, P., Barrot, G., Bovensmann, H., Gottwald, M., von Kuhlmann, R., Meijer, Y.: ESA's Atmospheric Chemistry Mission – A Status Report. In: Proceedings of the ESA Living Planet Symposium, ESA SP-686, Bergen, 2010

Gimeno García, S., Venema, V., Schreier, F., Trautmann, T.: Estimations of Errors when Calculating Radiative Transfer within Cloudy Atmospheres. In: Proceedings of the ESA Living Planet Symposium, ESA SP-686, Bergen, 2010

Gimeno García, S., Schreier, F., Lichtenberg, G., Slijkhuis, S., Hess, M., Aberle, B.: Nadir Sounding of Carbon Gases using SCIAMACHY Near Infrared Channels. In: Proceedings of the ESA Living Planet Symposium, ESA SP-686, Bergen, 2010

Gimeno García, S., Schreier, F., Lichtenberg, G., Slijkhuis, S., Hess, M., Aberle, B.: Nadir Sounding of Carbon Gases using SCIAMACHY Near Infrared Channels. 38<sup>th</sup> COSPAR Scientific Assembly, Bremen, 2010

Gottwald, M., Krieg, E., Lichtenberg, G., Noël, S., Bramstedt, K., Bovensmann, H.: SCIAMACHY In-Orbit Operations Until 2013. 38<sup>th</sup> COSPAR Scientific Assembly, Bremen, 2010

Gottwald, M., Krieg, E., Lichtenberg, G., Noël, S., Bramstedt, K., Bovensmann, H., Cirillo, F., Lützw-Wentzky, P.: Preparing SCIAMACHY for the Mission Extension Phase. In: Proceedings of the ESA Living Planet Symposium, ESA SP-686, Bergen, 2010

Gottwald, M., Krieg, E., Lichtenberg, G., Slijkhuis, S., von Savigny, C., Noël, S., Bovensmann, H., Bramstedt, K.: The Status of the SCIAMACHY Line-of-Sight Knowledge. In: Proceedings of the ESA Living Planet Symposium, ESA SP-686, Bergen, 2010

Gottwald, M.: Sensing the Polar Atmosphere with GOME and SCIAMACHY. Invited talk, International Polar Year Oslo Science Conference, Oslo, 2010

Hao, N., Valks, P., Rix, M., Loyola, D., Van Roozendael, M., De Smedt, I., Zhou, B., Zimmer, W.: Air quality measurements for the EXPO 2010 in Shanghai. In: Proceedings of the 2010 European Space Agency Living Planet Symposium, ESA SP-686, Bergen, 2010

Hao, N., Valks, P., Loyola, D., De Smedt, I., Van Roozendael, M., Theys, N., Rix, M., Koukouli, M., Balis, D., Pinardi, G., Zimmer, W.: Operational O3M-SAF trace gas column products: GOME-2 ozone, NO<sub>2</sub>, BrO, SO<sub>2</sub> and CH<sub>2</sub>O. 38<sup>th</sup> COSPAR Scientific Assembly, Bremen, 2010

Hao, N., Valks, P., Rix, M., Van Roozendael, M., Loyola, D., Zhou, B., Zimmer, W.: Air quality measurements for the EXPO 2010 in Shanghai. EUMETSAT Meteorological Satellite Conference, Cordoba, 2010

Hao, N., Valks, P., De Smedt, I., Emmadi, S., Lambert, J.C., Loyola, D., Pinardi, G., Rix, M., Van Roozendael, M., Theys, N., Zimmer, W.: Operational O3M-SAF trace gas column products: GOME-2 NO<sub>2</sub>, BrO, SO<sub>2</sub> and CH<sub>2</sub>O. European Geosciences Union General Assembly, Vienna, 2010

Heiden, U., Gredel, J., Pinnel, N., Mühle, H., Pengler, I., Reissig, K., Dietrich, D., Storch, T., Eberle, S., Kaufmann, H.: The User Interface of the ENMAP satellite mission. IGARSS2010, Hawaii, 2010

Hrechanyy, S., Doicu, A., Aberle, B., Lichtenberg, G., Meringer, M.: Sensitivity Analysis for SCIAMACHY Ozone Limb Retrieval. In: Proceedings of the ESA Living Planet Symposium, ESA SP-686, Bergen, 2010

Hrechanyy, S., De Smedt, I., Kretschel, K., Lichtenberg, G., Meringer, M., Wittrock, F.: Formaldehyde and Glyoxal: New Products in the SCIAMACHY Operational Processor. 38<sup>th</sup> COSPAR Scientific Assembly, Bremen, 2010

Loyola, D., Van Roozendael, M., Spurr, R., Balis, D., Lambert, J-C., Zimmer, W., Lerot, C., Koukouli, M., van Gent, J., Granville, J., Doicu, A., Zehner, C.: GDP 5.0 – The New Operational GOME Total Ozone Product Based on the GODFIT Algorithm. In: Proceedings of the ESA Living Planet Symposium, ESA SP-686, Bergen, 2010

Kitzmann, D., Vasquez, M., Patzer, B., Schreier, F., Rauer, H., Trautmann, T.: Influence of clouds on the reflection spectra of Earth-like extrasolar planets. European Planetary Science Congress, Rome, 2010

Lichtenberg, G., Slijkhuis, S., Gottwald, M., Snel, R., Fox, N., Mackin, S., Bramstedt, K., Krijger, J. M., Noël, S.: Application of QA4EO principles to SCIAMACHY Level 1 data. In: Proceedings of the ESA Living Planet Symposium, ESA SP-686, Bergen, 2010

Lichtenberg, G., Gimeno García, S., Schreier, F., Slijkhuis, Doicu, A., Snel R., Bovensmann, H.: Impact of Level 1 quality on SCIAMACHY Level 2 Retrieval. 38<sup>th</sup> COSPAR Scientific Assembly, Bremen, 2010

Rix, M., Valks, P., van Gent, J., van Roozendael, M., Spurr, R., Hao, N., Emmadi, S., Zimmer, W.: Monitoring of volcanic SO<sub>2</sub> emissions using the GOME-2 satellite instrument, European Geosciences Union General Assembly, Vienna, 2010

Rix, M., Valks P., Loyola, D., Maerker, C., van Gent, J., Van Roozendael, M., Spurr, R., Hao, N., Emmadi, S., Zimmer, W.: Monitoring of volcanic eruptions and determination of SO<sub>2</sub> plume height from GOME-2 measurements. EUMETSAT Meteorological Satellite Conference, Córdoba, 2010

Rix, M., Valks, P., Loyola, D., Maerker, C., Seidenberger, K., Van Gent, J., Van Roozendael, M., Spurr, R., Hao, N., Emmadi, S., Zimmer, W.: Monitoring of Volcanic Eruptions and Determination of SO<sub>2</sub> Plume Height from GOME-2 Measurements. In: Proceedings of the ESA Living Planet Symposium, ESA SP-686, Bergen, 2010

Schreier, F., Gimeno García, S., Lichtenberg, G., Hess, M.: Intercomparison of Near Infrared SCIAMACHY and Thermal Infrared Nadir Vertical Column Densities. In: Proceedings of the ESA Living Planet Symposium, ESA SP-686, Bergen, 2010

Schüssler, O., Loyola, D., Doicu, A.: Constrained Inversion Methods applied to Retrieval of Ozone Profiles from UV/VIS Nadir Sounding Instruments. In: Proceedings of the ESA Living Planet Symposium, ESA SP-686, Bergen, 2010

Schulz, J., Schroder, M., Fischer, J., Preusker, R., Loyola, D., Saunders, R., Ringer, M., Gleisner, H., Brockmann, C., Bojkov, B.: The ESA DUE GlobVapour Project. In: Proceedings of the ESA Living Planet Symposium, ESA SP-686, Bergen, 2010

Slijkhuis, S., Beirle, S., Emmadi, S., Loyola, D., Kalakoski, N., Mies, K., Wagner, T., Zimmer, W.: Water Vapour: a new pre-operational O3M-SAF GOME-2 product. EUMETSAT Meteorological Satellite Conference, Córdoba, 2010

Valks, P. and the O3M-SAF team: The EUMETSAT Satellite Application Facility on Ozone and Atmospheric Chemistry Monitoring. GMES Operational Capacity Workshop, Sofia, 2010

Valks, P., Beirle, S., De Smedt, I., Emmadi, S., Hao, N., Kalakoski, N., Lambert, J-C., Loyola, D., Mies, K., Pinardi, G., Richter, A., Rix, M., Van Roozendael, M., Slijkhuis, S., Theys, N., Wagner, T., Zimmer, W.:

Operational O3M-SAF Trace Gas Column Products: GOME-2 NO<sub>2</sub>, BrO, SO<sub>2</sub>, CH<sub>2</sub>O, OclO and H<sub>2</sub>O. In: Proceedings of the ESA Living Planet Symposium, ESA SP-686, Bergen, 2010

Valks, P., Hao, N., Loyola, D., De Smedt, I., Van Roozendael, M., Theys, N., Rix, M., Lambert, J-C., Pinardi, G., Zimmer, W., Emmadi, S.: Operational O3M-SAF trace gas column products: GOME-2 NO<sub>2</sub>, BrO, SO<sub>2</sub> and CH<sub>2</sub>O. EUMETSAT Meteorological Satellite Conference, Córdoba, 2010

Van Roozendael, M., Loyola, D., van der A, R., Weber, M., Lambert, J-C., Balis, D., Braesicke, P., Dameris, M., Fussen, D., Hauchecorne, A., Kerridge, B., Kyrola, E., Orphal, J., Siddans, R., von Savigny, C., Stiller, G., Tamminen, J., van Velthoven, P., Wolfmueller, M., Zerefos, C.: Building Consolidated Climate-Relevant Ozone Data Sets in the Framework of the ESA CCI Programme. In: Proceedings of the ESA Living Planet Symposium, ESA SP-686, Bergen, 2010

Vasquez, M., Schreier, F., Gimeno García, S., Gottwald, M., Slijkhuis, S., Lichtenberg, G.: Venus Modeled Spectrum Compared with SCIAMACHY Observations. In: Proceedings of the ESA Living Planet Symposium, ESA SP-686, Bergen, 2010

Vasquez, M., Schreier, F., Gimeno García, S., Gottwald, M., Slijkhuis, S.: Venus Near-Infrared Spectra: SCIAMACHY-Observations and Modeling. 38<sup>th</sup> COSPAR Scientific Assembly, Bremen, 2010

Vasquez, M., Schreier, F., Gottwald, M., Slijkhuis, S., Gimeno García, S., Krieg, E., Lichtenberg, G.: Venus Near-Infrared Spectra: SCIAMACHY-Observations and Modeling. In: Pathways towards Habitable Planets ASP Conference Proceedings, 430. Astronomical Society of the Pacific, 2010

Zenner, L., Fagiolini, E., Daras, I., Flechtner, F., Gruber, T., Schmidt, T., Schwarz, G., Stammer, D., Trautmann, T., Wickert, J.: Improved De-aliasing for Gravity Field Modelling with GRACE. 2<sup>nd</sup> SPP1257-Colloquium, Potsdam, 2010

#### **5.4 Attended Conferences and Professional Leaves**

GMES Operational Capacity Workshop, Sofia, Bulgaria, March 25/26, 2010

Helmholtz Alliance *Planetary Evolution and Life* Workshop, Berlin, Germany, March 28-31, 2010

European Geosciences Union General Assembly, Vienna, Austria, May 2-7, 2010

ESA/EUMETSAT Workshop on Volcanic Ash Monitoring, Frascati, Italy, May 26/27, 2010

International Polar Year Oslo Science Conference, Oslo, Norway, June 7-12, 2010

Open ARTS Community Workshop, Kristineberg, Sweden, June 7-10, 2010

ESA Living Planet Symposium 2010, Bergen, Norway, June 28 – July 2, 2010

38<sup>th</sup> COSPAR Scientific Assembly, Bremen, Germany, July 18-25, 2010

European Planetary Science Congress, Rome, Italy, September 19-24, 2010

EUMETSAT Meteorological Satellite Conference, Cordoba, Spain, September 20-24, 2010

2<sup>nd</sup> Colloquium on Mass Transport and Mass Distribution in the System Earth (SPP1257), Potsdam, Germany, October 13/14, 2010

2. Herbstschule des Netzwerks EOS, Lauenburg, Germany, November 16-19, 2010

## 5.5 Diploma and Doctoral Theses

Fagiolini, E.: The impact of atmospheric variability on the determination of the gravity field of the Earth. Dissertation, Faculty of Civil Engineering and Geodesy, Technical University of Munich. (Supervisors: Prof. Dr. Reiner Rummel, Technical University of Munich and Gottfried Schwarz)

Gimeno García, S.: Simulation of solar radiative transfer and comparison with spectro-radiometric measurements. Dissertation, Faculty of Physics and Earth Science, University of Leipzig. (Supervisor: Prof. Dr. Thomas Trautmann)

Köhler, C.H.: Observation and simulation of the longwave radiative effects for Saharan mineral dust plumes. Dissertation, Faculty of Physics and Earth Science, University of Leipzig. (Supervisors: Prof. Dr. Manfred Wendisch, University of Leipzig and Prof. Dr. Thomas Trautmann)

Lonitz, K.: Comparison of MISR and Meteosat-9 Cloud Motion Winds. Diploma Thesis, Faculty of Physics and Earth Sciences, University of Leipzig, March 2010. (Supervisor: Prof. Dr. T. Trautmann)

Otto, S.: Optische Eigenschaften von Saharamineralstaub und dessen klimarelevanter Einfluss auf den Strahlungstransport in der Erdatmosphäre. Dissertation, Faculty of Physics and Earth Science, University of Leipzig. (Supervisors: Prof. Dr. Manfred Wendisch, University of Leipzig and Prof. Dr. Thomas Trautmann)

Rix, M.: Observation of volcanic SO<sub>2</sub> plumes based on the satellite-borne GOME-2 instrument. Dissertation, Faculty of Civil Engineering and Geodesy, Technical University of Munich. (Supervisors: Prof. Dr. Richard Bamler, Technical University of Munich and Dr. Pieter Valks)

Schüssler, O.: Combined Inversion Methods for UV/VIS Nadir Sounding. Dissertation, Civil Engineering and Geodesy, Technical University of Munich. (Supervisors: Prof. Dr. Richard Bamler, Dr. Adrian Doicu and Diego Loyola)

Szopa, M.: Inversion methods for atmospheric nadir infrared sounding. Dissertation, Faculty for Mathematics and Science, University of Potsdam. (Supervisors: Prof. Dr. Christine Böckmann, University of Potsdam and Dr. Adrian Doicu)

Vasquez, M.: Simulation of the radiation field in planetary atmospheres. Dissertation, Centre of Astronomy and Astrophysics, Technical University of Berlin. (Supervisors: Prof. Dr. Heike Rauer, German Aerospace Center, Institute of Planetary Research and Dr. Franz Schreier)

Xu, J.: Inversion for Limb Infrared Atmospheric Sounding. Dissertation, Civil Engineering and Geodesy, Technical University of Munich. (Supervisors: Prof. Dr. Richard Bamler, Dr. Franz Schreier, and Prof. Dr. Thomas Trautmann)

## Abbreviations and Acronyms

AD	Automatic Differentiation
AMF	Airmass Factor
ANX	Ascending Node Crossing
AOT	Aerosol Optical Thickness
AP	Atmospheric Processors
ARD	Absolute Relative Difference
ASM	Azimuth Scan Mechanism
ATBD	Algorithm Theoretical Basis Document
ATC	Active Thermal Control
BIRA-IASB	Belgisch Instituut voor Ruimte-Aëronomie Institut d' Aëronomie Spatiale de Belgique
BIRRA	Beer InfraRed Retrieval Algorithm
BL	Boundary Layer
BOA	Bottom-of-Atmosphere
BTD	Brightness Temperature Difference
CF	Cloud Fraction
CKD	Correlated K-Distribution
CLO	Consolidated Level 0
COT	Cloud Optical Thickness
CPU	Central Processing Unit
CTI	Customer Furnished Item
CTM	Chemistry Transport Model
CTP	Cloud Top Height
CVS	Concurrent Versioning System
DFD	Deutsches Fernerkundungsdatenzentrum
DFG	Deutsche Forschungsgemeinschaft
DIMS	Data & Information Management System
DLR	Deutsches Zentrum für Luft- und Raumfahrt
DOAS	Differential Optical Absorption Spectroscopy
D-PAC	German Processing and Archiving Center
DRACULA	Advanced Retrieval of the Atmosphere with Constrained and Unconstrained Least-Squares Algorithms
DRE	Direct Aerosol Radiative Effect
DVCD	Differential Vertical Column Density
ECM	Emission Control Measure
ECV	Essential Climate Variable
ENVISAT	Environmental Satellite
EO	Earth Observation
EOC	Earth Observation Center
EQC	Equality-Constrained
ERS	European Remote Sensing Satellite
ESA	European Space Agency
ESAS	Earth's Surface Atmosphere System
ESM	Elevation Scan Mechanism
ESRIN	European Space Research Institute
ESTEC	European Space Technology Center
EUMETSAT	European Organisation for the Exploitation of Meteorological Satellites
EVOSS	European Volcano Observatory Space Services
FD	Fast Delivery
FPGA	Field Programmable Gate Array
FTIR	Fourier Transform Infrared Spectrometer
GARLIC	Generic Atmospheric Radiation Line-by-Line Infrared Code
GDP	GOME Data Processor
GEISA	Gestion et Etude des Informations Spectroscopiques Atmosphériques

GIS	Geographic Information System
GMES	Global Monitoring for Environment and Security
GODFIT	GOME Direct Fitting
GOME	Global Ozone Monitoring Experiment
GOMOS	Global Ozone Monitoring by Occultation of Stars
GPU	Graphics Processing Unit
GUI	Graphical User Interface
HITRAN	High Resolution Transmission
HK	Housekeeping
IASI	Infrared Atmospheric Sounding Interferometer
ICA	Independent Column Approximation
IDE	Integrated Development Environment
IMF	Institut für Methodik der Fernerkundung
I/O	Input/Output
IRE	Indirect Radiative Effect
IRGN	Iteratively Regularised Gauss-Newton
IRVR	Inner Ring Viaduct Road
IUP-IFE	Institut für Umweltphysik / Institut für Fernerkundung
IR	Infrared
LCPS	Particle Size Spectrometer
LES	Large-Eddy Simulation
LIDAR	Light Detection and Ranging
LIDORT	Linearized Discrete Ordinate Radiative Transfer
LMU	Ludwig-Maximilians-University
LoS	Line-of-Sight
LWC	Liquid Water Content
MetOp	Meteorological Operational Polar Satellites of EUMETSAT
MIPAS	Michelson Interferometer for Passive Atmospheric Sounding
MoCaRT	Monte Carlo Radiative Transfer
MODIS	Moderate Resolution Imaging Spectroradiometer
MOPITT	Measurements of Pollution in the Troposphere
MPS	Mission Planning System
MW	Microwave
NIST	National Institute of Standards and Technology
NMVOC	Non-methane Volatile Organic Compound
NNTM	Non-Nominal Telemetry
NRT	Near-realtime
NWP	Numerical Weather Prediction
O3M	Ozone Monitoring
OCM	Orbit Control Manoeuvre
OCR	Operation Change Request
ODE	Ozone Depletion Event
OL	Offline
OMI	Ozone Monitoring Instrument
OS	Operating System
PDS	Payload Data Segment
PILS	Profile Inversion for Limb Sounding
PIRATES	Programmer's Interface to Radiative Transfer Algorithms
PM	Particulate Matter
PMD	Polarization Measurement Device
PPA	Plane Parallel Approximation
PREMIER	Process Exploration through Measurements of Infrared and Millimetre-wave Emitted Radiation
PUM	Product User Manual
QA4EO	Quality Assurance Framework for Earth Observation
RAL	Rutherford Appleton Laboratory
RAM	Random Access Memory

RCS	Revision Control System
RT	Radiative Transfer
SACS	Support to Aviation Control Service
SAF	Satellite Application Facility
SAMUM	Sahara Mineral Dust Experiment
SCCS	Source Code Control System
SCIAMACHY	Scanning Imaging Absorption Spectrometer for Atmospheric Chartography
SCD	Slant Column Density
SEU	Single Event Upset
SGP	Southern Great Plains
SLS	Spectral Line Source
SMHI	Swedish Meteorological and Hydrological Institute
SMILES	Superconducting-Submillimeter-Wave Limb-Emission Sounder
SNR	Signal-to-Noise Ratio
SOST	SCIAMACHY Operations Support Team
SQWG	SCIAMACHY Quality Working Group
SRON	Netherlands Institute for Space Research
SVN	Subversion
SZA	Solar Zenith Angle
TELIS	TeraHertz Limb Sounder
TIR	Thermal Infrared
TOA	Top-of-Atmosphere
TR	Tikhonov Regularization
TUM	Technical University Munich
TV	Thermal Vacuum
UMAS	Unified Mapping Tool for Atmospheric Spectrometers
UV	Ultraviolet
VAAC	Volcanic Ash Advisory Centre
VCD	Vertical Column Density
VINO	Versatile Inversion for Nadir Observations
VIS	Visual
VOC	Volatile Organic Compound
WLS	White Light Source

## DLR at a Glance

DLR is Germany's national research center for aeronautics and space. Its extensive research and development work is integrated into national and international cooperative ventures. As Germany's space agency, DLR has been given responsibility for the forward planning and the implementation of the German space program by the German federal government as well as for the international representation of German interests. Furthermore, Germany's largest project-management agency is also part of DLR.

Approximately 6,900 people are employed at thirteen locations in Germany: Köln (headquarters), Berlin, Bonn, Braunschweig, Bremen, Göttingen, Hamburg, Lampoldshausen, Neustrelitz, Oberpfaffenhofen, Stuttgart, Trauen and Weilheim. DLR also operates offices in Brussels, Paris, and Washington, D.C.

### Remote Sensing Technology Institute Institut für Methodik der Fernerkundung

DLR's Remote Sensing Technology Institute (IMF) is located in Oberpfaffenhofen, Berlin-Adlershof, and Neustrelitz.

IMF carries out research and development for retrieving geo-information from remote sensing data. It conducts basic research on physical principles of remote sensing and develops algorithms, techniques, and operational processing systems for synthetic aperture radar, optical remote sensing, and spectrometric sounding of the atmosphere. The processing systems are in operational use for national, European, and international Earth observation missions.

For preparation and in support of spaceborne missions IMF operates a suite of multi- and hyperspectral optical airborne sensors. The institute contributes its expertise to novel sensor and mission concepts.

The German Remote Sensing Data Center (DFD) and IMF form DLR's Earth Observation Center (EOC).



DLR

**Deutsches Zentrum  
für Luft- und Raumfahrt e.V.**  
in der Helmholtz-Gemeinschaft

**Institut für Methodik der Fernerkundung**  
Oberpfaffenhofen  
82234 Weßling

[www.dlr.de/caf](http://www.dlr.de/caf)